BERGISCHE
UNIVERSITÄT
WUPPERTAL

JÜLICH
Forschungszentrum

Development of a data processing chain for a spatial heterodyne interferometer measuring temperature in the mesosphere and lower thermosphere

Dissertation
zur Erlangung des Grades
Doktor der Naturwissenschaften (Dr. rer. nat.)

vorgelegt der
Bergischen Universität Wuppertal
Fakultät 4 - Mathematik und Naturwissenschaften

von
Konstantin Ntokas

Wuppertal 2023

Contents

List of Figures

List of Tables

Abstract

Atmospheric dynamics are governed by wave-like patterns that propagate momentum throughout the atmosphere. Over the past few decades, numerous observational methods have been developed to capture these wave characteristics. With the steady advancement of computing power, atmospheric models extend their reach to higher altitudes, allowing for the modeling of larger portions of the atmosphere with greater resolution. Both, observation and theoretical simulation have highlighted the significant role played by gravity waves in the mesosphere and lower thermosphere (MLT). Gravity waves, which are small to medium-scale atmospheric waves, originate in the lower atmosphere and travel upward, carrying momentum into the upper atmosphere. As they ascend, these waves can break and dissipate at higher altitudes, and transfer their momentum to the background wind field. Consequently, continuous global observations of gravity waves in this region have become a topic of particular interest.

Gravity wave characteristics can be deduced from their impact onto the temperature field of the background atmosphere (temperature residuals). To this end, a limb-sounding instrument has been developed to observe temperature in the MLT region. The limb observing configuration excels in vertical resolution, a crucial factor in accurately capturing the relatively short vertical wavelengths of gravity waves. Employing Fourier transform spectroscopy, this instrument utilizes a spatial heterodyne interferometer to resolve rotational structures within the O_2 atmospheric A-band airglow emission in the near-infrared spectrum. Notably, this emission is observable during both day and night, enabling continuous monitoring. The instrument records a two-dimensional image. The vertical axis encodes spatial information corresponding to different tangent altitudes, while the horizontal axis superimposes spectral and spatial information. This arrangement allows for the derivation of a vertical temperature profile from a single image. The method exploits the relative intensities of emission lines to retrieve temperature, removing the need for absolute radiometric calibration, which simplifies the calibration process. Furthermore, since the emission falls in the near-infrared range, silicon-based detectors can be used, which operate under ambient conditions and do not require extensive cooling devices. This enables the design of the instrument according to CubeSat standards. Following the initial instrument version, a redesign led to the creation of a second version called AtmoLITE, which will be deployed in subsequent scientific missions. This work primarily focuses on the second version and assesses its performance, with a particular emphasis on the International Satellite Program in Research and Education (INSPIRE) Sat-4 mission.

Due to the instrument's redesign, it is necessary to determine the overall uncertainties and performance limits of the new version. Achieving accurate temperature measurements entails meticulous image processing, with a specific focus on correcting errors stemming from instrument imperfections. This process entails the identification and comprehension of new errors, leading to the development of correction methods. The availability of an extensive calibration dataset for the INSPIRESat4 mission allows a comprehensive evaluation of these correction methods. Uncertainties and minor errors from the correction procedures are propagated into the uncertainties of the derived temperatures, aiding to understand which processing steps are critical for obtaining precise temperature observations. Furthermore, an end-to-end simulation, based on calibration measurements, facilitates the assessment of instrument performance, encompassing all instrument errors at the calibration stage.

In addition, a novel processing method is under investigation, offering the potential to resolve horizontal across-track temperature variations assuming the viewing direction of the instrument is along the satellite‘s flight track. Exploiting the spatial information lying underneath the spectral modulation along the horizontal axis, this innovative approach splits the field of view, providing the capability to derive not only vertical but also horizontal wave parameters.

Kurzfassung

Die Dynamik der Atmosphäre wird durch wellenartige Muster bestimmt, welche Momentum durch die Atmosphäre transportieren. In den letzten Jahrzehnten wurden zahlreiche Beobachtungsmethoden entwickelt, um Eigenschaften dieser Wellen zu erfassen. Mit der stetigen Weiterentwicklung der Rechenleistung dringen Atmosphärenmodelle in größere Höhen vor, was die Modellierung größerer Teile der Atmosphäre mit höherer Auflösung ermöglicht. Sowohl Beobachtungen als auch theoretische Simulationen haben die bedeutende Rolle von Schwerewellen in der Mesosphäre und der unteren Thermosphäre (MLT) deutlich gemacht. Schwerewellen, was kleine bis mittelgroße atmosphärische Wellen sind, haben ihren Ursprung in der unteren Atmosphäre und wandern nach oben, wobei sie Momentum in die obere Atmosphäre tragen. Auf ihrem Weg nach oben können diese Wellen brechen und ihren Impuls an den Hintergrundwind abgeben. Daher ist die kontinuierliche globale Beobachtung von Schwerewellen in dieser Region von besonderem Interesse.

Die Eigenschaften von Schwerewellen lassen sich aus ihrem Einfluss auf das Temperaturfeld der Hintergrundatmosphäre (Temperaturresiduen) ableiten. Zu diesem Zweck wurde ein Limb-Sounding-Instrument zur Beobachtung der Temperatur in der MLT-Region entwickelt. Die Limb-Beobachtungskonfiguration bietet eine hohe vertikale Auflösung, ein entscheidender Faktor, um die vergleichsweise kurzen vertikalen Wellenlängen von Gravitationswellen genau zu erfassen. Unter Verwendung der Fourier-Transform-Spektroskopie nutzt dieses Instrument ein Spatial Heterodyne Interferometer, um die Verteilung der Rotationsemissionen innerhalb der atmosphärischen O_2 A-Bande im nahen Infrarotspektrum aufzulösen. Diese Emission kann sowohl bei Tag als auch bei Nacht beobachtet werden, was eine kontinuierliche Beobachtung ermöglicht. Das Instrument nimmt ein zweidimensionales Bild auf. Die vertikale Achse kodiert räumliche Informationen, die den verschiedenen Tangentenhöhen entsprechen, während die horizontale Achse spektrale und räumliche Informationen überlagert. Diese Anordnung ermöglicht die Ableitung eines vertikalen Temperaturprofils aus einem einzigen Bild. Die Methode nutzt die relativen Intensitäten der Emissionslinien, um die Temperatur zu ermitteln, so dass eine absolute radiometrische Kalibrierung nicht erforderlich ist, was den Kalibrierungsprozess vereinfacht. Da die Emission in den Nahinfrarotbereich fällt, is die Verwendung von Detektoren auf Siliziumbasis möglich, die unter normalen Umgebungsbedingungen arbeiten und keine umfangreichen Kühlvorrichtungen benötigen. Dies ermöglicht die Konstruktion des Instruments gemäß den CubeSat-Standards. Im Anschluss an die erste Version des Instruments wurde eine zweite Version mit dem Namen AtmoLITE entwickelt, die in den kommenden wissenschaftlichen Missionen eingesetzt wird. Diese Arbeit konzentriert sich in erster Linie auf die zweite Instrumentenversion und bewertet deren Leistungsfähigkeit, wobei der Schwerpunkt auf der International Satellite Program in Research and Education (INSPIRE) Sat-4 Mission liegt.

Aufgrund der Neukonstruktion des Instruments müssen die Messunsicherheiten und Leistungsgrenzen der neuen Version bestimmt werden. Um genaue Temperaturmessungen zu erzielen, ist eine sorgfältige Bildverarbeitung erforderlich, wobei ein besonderer Schwerpunkt auf der Korrektur von Fehlern liegt, die auf Unzulänglichkeiten des Instruments zurückzuführen sind. Dieser Prozess beinhaltet die Identifizierung und das Verstehen neuer Fehler, was zur Entwicklung von Korrekturmethoden führt. Die Verfügbarkeit eines umfangreichen Kalibrierungsdatensatzes für die INSPIRESat4-Mission ermöglicht eine umfassende Evaluierung dieser Korrekturmethoden. Unsicherheiten und kleinere Fehler aus den Korrekturverfahren werden durch Simulationen in die Unsicherheiten der abgeleiteten Temperaturen

fortgepflanzt. Dies hilft zu verstehen, welche Verarbeitungsschritte für den Erhalt präziser Temperaturbeobachtungen entscheidend sind. Darüber hinaus ermöglicht eine End-to-End-Simulation auf der Grundlage von Kalibrierungsmessungen die Bewertung der Instrumentenleistung, wobei alle Instrumentenfehler in der Kalibrierungsphase berücksichtigt werden.

Zusätzlich wird eine neuartige Prozessierungsmethode untersucht, die das Potenzial hat, horizontale Temperaturresiduen quer zur Flugspur des Satelliten aufzulösen, vorausgesetzt, die Betrachtungsrichtung des Instruments erfolgt entlang der Flugspur des Satelliten. Unter Ausnutzung der räumlichen Informationen, die unter der spektralen Modulation entlang der horizontalen Achse liegen, teilt dieser innovative Ansatz das Sichtfeld und bietet die Möglichkeit, nicht nur vertikale, sondern auch horizontale Wellenparameter abzuleiten.

Chapter 1

Introduction

The dynamics of the atmosphere are governed by wave-like patterns exhibited by atmospheric parameters such as pressure, temperature, and wind velocity. Numerous wave types have been identified, each rooted in diverse dynamical principles and displaying distinct properties, often caused by specific atmospheric conditions. The most prominent wave types are atmospheric tides, planetary waves and gravity waves. Atmospheric tides are global-scale periodic oscillations primarily induced by diurnally varying solar radiation. Planetary waves, also known as Rossby waves, are large-scale perturbations that generally arise due to the interplay of the Coriolis force and pressure gradients within a rotating system, such as the Earth. Gravity waves are small to medium-scale wave patterns that originate from the displacement of air masses from their hydrostatic equilibrium position, where gravity or buoyancy acts on these air masses to restore equilibrium. Planetary and gravity waves play a pivotal role in shaping the general circulation patterns of the middle atmosphere. Planetary waves largely drive the equator-to-pole circulations in the stratosphere (Holton et al., 1995), while gravity waves are the dominant driver of the pole-to-pole circulation in the mesosphere (Smith, 2004; Schmidt et al., 2006).

Gravity waves mainly travel vertically, bridging different atmospheric layers, with wavelengths ranging from a few to several tens of kilometers. They can be carried along horizontally with the atmospheric circulation resulting in wavelengths ranging from a few hundred to several thousand kilometers. These waves are predominantly excited in the lower atmosphere

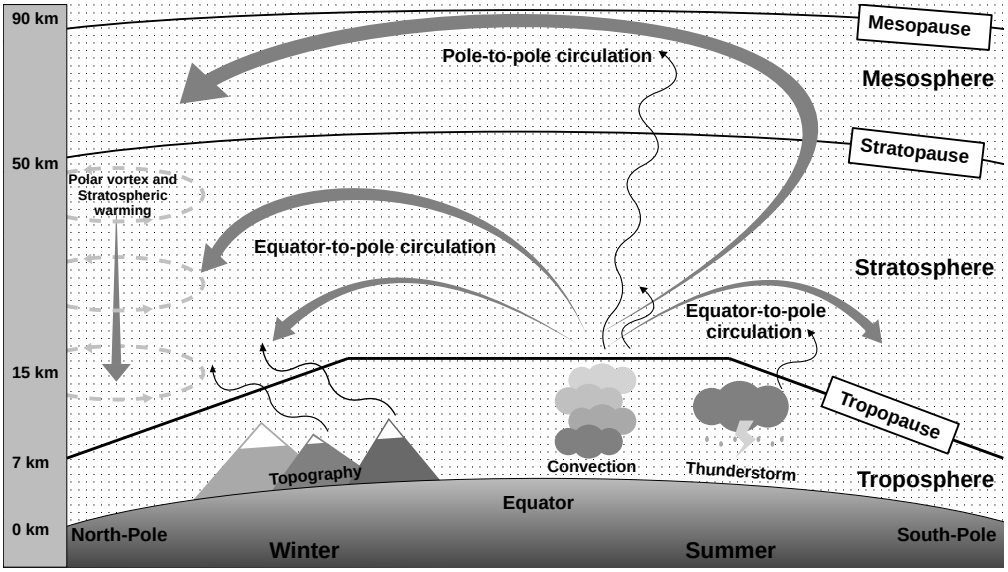

Figure 1.1: The influence of gravity waves onto the global circulation pattern of the middle atmosphere for the northern hemisphere winter time; gravity waves are displayed by wavy thin arrows and the global circulation pattern of the middle atmosphere is depicted by thick gray arrows. For the northern hemisphere summer time, the mesospheric pole-to-pole circulation is reversed. The polar vortex turns in the opposite direction.

due to various factors, such as convection, thunderstorms, unstable jets, and the uplift of air masses flowing over mountains, as illustrated in Figure 1.1. As these waves propagate upward in the atmosphere, their amplitude increases exponentially to counterbalance the diminishing density (Andrews et al., 1987), leading to enhanced wave breaking and momentum deposition. They can interact with the polar vortex and play a substantial role in the breakdown of the polar vortex during spring time (Gupta et al., 2021), which, in turn, influences surface weather as cold air masses descend into the troposphere. Furthermore, as previously mentioned, high-rising gravity waves drive the circulation pattern from the summer to the winter pole in the mesopause region. The rising air over the summer hemisphere causes adiabatic cooling, while the descending air over the winter pole results in adiabatic heating. These vertical movements account for the intriguing phenomenon where the polar summer mesosphere, despite receiving 24-hour sunlight, stands as the coldest region in the atmosphere, resulting in temperature variations up to 50 K compared to what would be expected solely based on radiative equilibrium (Vincent, 2015). Therefore, observing gravity waves up to the mesosphere and lower thermosphere (MLT) is crucial for gaining a deeper understanding of the complex dynamics

and energy displacement in the middle atmosphere.

Insights into gravity waves can be derived from various atmospheric parameters. Wind data, for instance, exhibits wave-like patterns induced by gravity waves, enabling the determination of wave orientation and scale. Also, the transport of momentum by gravity waves can be calculated using wind data, as demonstrated by Fritts and Alexander (2003). Alexander et al. (2010) highlights the value of ground-based radar and radiosondes in providing wind data with high temporal and vertical resolution at specific geographic stations. Nonetheless, their limited spatial distribution poses challenges in observing these waves over large horizontal scales. Air- or spaceborne remote sensing techniques can help, as they observe a large volume of air in a short period from a point being distant from the measured object. Satellite-based instruments, in particular, offer the potential for mesoscale or even global coverage, making them highly suitable for studying gravity wave phenomena on a broader scale. Hereby, temperature data is commonly used to extract valuable insights about gravity waves (Alexander et al., 2010). Similar to wind data, wave-like patterns imprinted by gravity waves can reveal their orientation and scale. Temperature data, following the approach outlined by Ern (2004), can also be employed to compute the transport of momentum by gravity waves. Therefore, as highlighted by Preusse et al. (2009), the acquisition of temperature data from a spaceborne instrument within the MLT region holds great promise for a more comprehensive analysis of gravity wave activity.

A common technique for observing physical parameters from spaceborne instruments is passive remote sensing. It relies on the fact that physical quantities, such as temperature, impacts the radiation captured by the instrument. The captured radiation thus can be utilized during data processing to inversely derive the desired atmospheric parameter.

To capture the relatively small vertical wavelengths of gravity waves, the instrument must be capable of detecting subtle changes in radiance along the altitude axis. Limb geometry is particularly suitable for meeting this criterion. In limb geometry, the instrument's line of sights (LOSs) through the atmosphere are tangential to the Earth's surface, as shown in Fig. 1.2. This viewing geometry enables the instrument to independently capture the radiation traveling along each LOS toward the instrument's aperture. Consequently, it allows for the observation

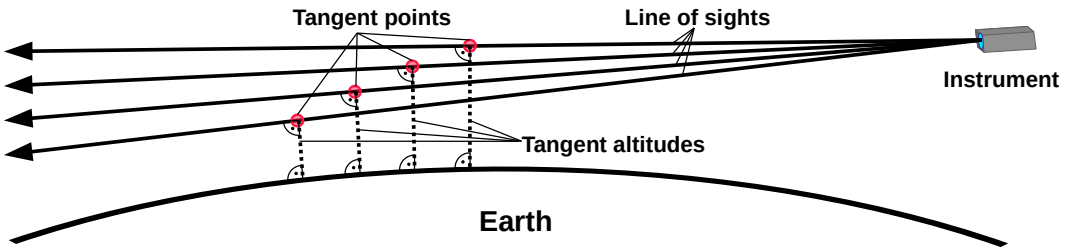

Figure 1.2: Viewing geometry of a limb sounding instrument

of each altitude separately. The tangent point, which is the point closest to the Earth's surface along a given LOS, defines the tangent altitude of the measurement associated with the LOS. This altitude represents the distance between the tangent point and the Earth's surface. This viewing geometry is often used by spaceborne instruments used for gravity research (Gille et al., 2008; Llewellyn et al., 2004; Preusse et al., 2006). A more detailed overview of past and present instruments used in this field is given in Appx. A.3, which shows that a void in atmospheric data suitable for gravity wave research is anticipated to arise in the upcoming years.

A collaborative effort between the Jülich Research Center and the University of Wuppertal in Germany led to the development of a limb sounding instrument (Kaufmann et al., 2018). The instrument design aims to provide vertical temperature profiles with a fine vertical resolution of 1.5 km. These precise measurements enable the effective capture and analysis of small to medium-scale gravity waves propagating vertically in this region.

The observational method was initially tested during the 2017 Atmospheric Heterodyne Interferometer Test (AtmoHIT) mission within the REXUS program. Building upon the AtmoHIT optical design, the Atmospheric Spatial Heterodyne Interferometer Next Explorer (AtmoSHINE) was launched aboard the Chinese Hongyun satellite in December 2018, marking the first in-orbit demonstration of O_2 A-band nighttime measurements. Preliminary image correction methods were developed by Liu et al. (2019), and Chen (2020) performed initial temperature retrieval tests. To address stray light challenges, the optical system was redesigned, resulting in the current instrument version, called Atmospheric Limb Interferometer for Temperature Exploration (AtmoLITE). AtmoLITE features a widened spectral bandpass for en-

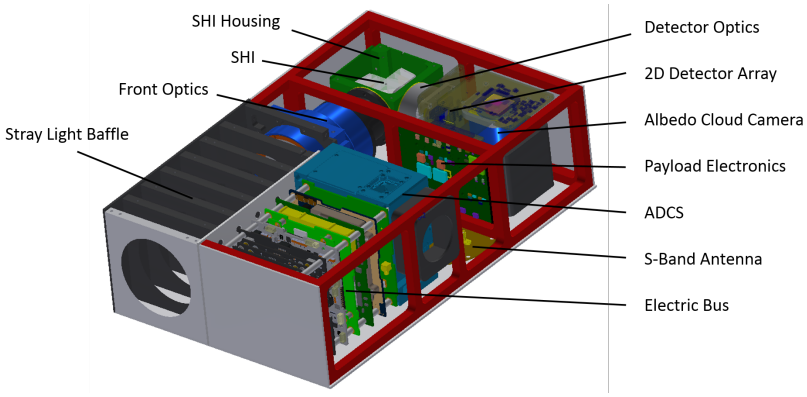

Figure 1.3: Model of the AtmoLITE instrument deployed on 6 CubSats with an external size of $30 \times 20 \times 10$ cm; by Olschewski et al. (2018)

hanced signal strength, albeit with reduced spectral resolution. It is part of the International Satellite Program in Research and Education (INSPIRE) Sat-4 and Sat-3 missions and has been selected by the European Commission for in-orbit validation as part of the MetEOC-4 Spatial Heterodyne Interferometer Performance Assessment in Space (SHIPAS) mission under the H2020 program.

A model of the AtmoLITE instrument is shown in Fig.1.3. Atmospheric radiance enters through a baffle located in front of the instrument to mitigate stray light from the sides. The instrument captures a 2D image of the atmospheric radiance, with the front and camera optics mapping the atmospheric scene onto a 2D detector array. A spatial heterodyne interferometer (SHI) is utilized to resolve the spectrum of the captured radiance through interference. The interference appears as a superposition of multiple cosine waves on the detector, as shown in Figure 1.4, with spatial frequencies determined by the incoming light's frequencies. Essentially, the SHI performs an inverse Fourier transformation on the incoming light, converting it into an interferogram placed on the horizontal axis of the detector. SHIs are therefore a specific realization of Fourier-Transform spectroscopy. The horizontal axis is employed during data processing to extract temperature information from the spectral signature of the incoming radiance, while the vertical axis represents the spatial characteristics of the observed atmospheric structure for each LOS, as illustrated in Figure 1.2. Consequently, a single image allows for the retrieval of a 1D temperature profile.

A bandpass filter is used to observe a 6 nm spectral band centered at 763 nm, covering

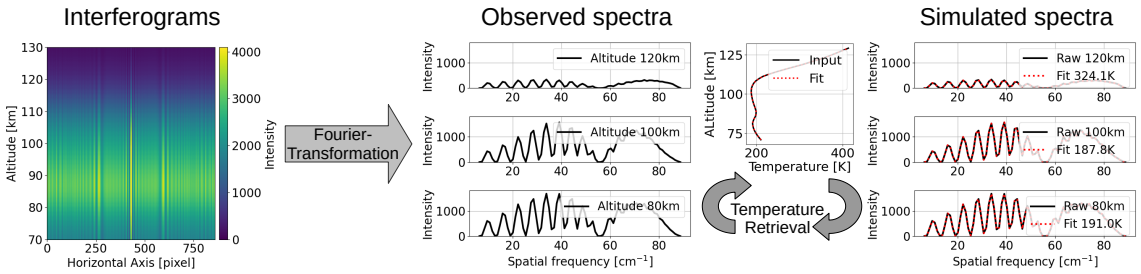

Figure 1.4: Methodological overview of the data processing

the oxygen atmospheric A-band emissions. This choice offers several advantages: First, the signal strength peaks around 90 km altitude, providing high accuracy in the mesopause region, making it suitable for studying MLT dynamics. Second, the emissions are partly visible during nighttime, increasing the local time coverage of the observation. Third, the temperature can be derived from the relative distribution of the spectral band, eliminating the need for radiometric calibration and simplifying the calibration process. Fourth, since the oxygen A-band emissions are close to the visible range, detectors that do not require extensive cooling can be used. This allows for the design of a highly compact and energy-efficient instrument, built upon CubeSat standards, as depicted in Fig. 1.3.

A CubeSat is a predefined container of $10\,\text{cm} \times 10\,\text{cm} \times 10\,\text{cm}$, which standardizes the platform size of a satellite, developed by Stanford and California Polytechnic State Universities in 1999 (Heidt et al., 2000). Stacking multiple CubeSats for flexibility is common, as shown by Poghosyan and Golkar (2017). Advances in miniaturization of cost-effective commercial off-the-shelf (COTS) components have revolutionized small spacecraft design. Initially, CubeSats were used for educational or demonstration purposes, as exemplified by the SwissCube mission (Borgeaud et al., 2010). However, in recent years, there has been a significant increase in low-cost science missions employing CubeSats (Poghosyan and Golkar, 2017; Bouwmeester and Guo, 2010). Using COTS components and CubeSat standards substantially lowers the cost and complexity of satellite development, making it accessible to smaller countries and educational institutions. It shortens the development timeline to just a few years, in contrast to the $5 - 10$ years typically required for traditional missions (Poghosyan and Golkar, 2017).

The task of the AtmoLITE data processing involves deriving a temperature profile from

the interferograms. The methodology is outlined in Fig. 1.4. Initially, a Fourier transform is applied along the horizontal axis, converting the interferograms row-wise into spectra, referred to as the measured spectra. Subsequently, a forward model is employed, taking a 1D vertical temperature profile as input and generating analytical spectra for all altitudes as seen from the instrument. Inverse modeling uses this forward model to optimize the temperature input, while minimizing the differences between the measured and simulated spectra. The forward model consists of two steps: First, radiative transfer calculations simulate radiances at various tangent altitudes for each LOS depicted in Fig. 1.2. Second, instrument specifications are considered to simulate the spectrum as observed by the instrument itself. Notably, the enhancement of previous radiative transfer models for this instrument group involves the incorporation of self-absorption, which accounts for the absorption of radiation by ground-state oxygen molecules and refers to the inverse transition of the emissions.

The main part of the thesis revolves around the performance assessment of the AtmoLITE instrument using the calibration data from the upcoming INSPIRESat-4 mission. The temperature precision of AtmoLITE is primarily governed by the noise level, which is closely tied to the strength of the signal. To evaluate its performance, an end-to-end simulator is developed. This simulator encompasses an interferogram simulation based on an updated forward model, including self-absorption. Subsequently, data processing is employed that results in the retrieval of temperature profiles. This approach allows to assess the performance limits of an ideal instrument in terms of the derived temperature precision.

In a real world application, multiple errors may affect observations due to instrument imperfections. To obtain an accurate temperature product, it is essential to correct these errors during data processing, which is the primary focus of this work. This thesis identifies and understands new errors, leading to the development of correction methods. The extensive calibration data set for the INSPIRESat-4 mission enables a comprehensive evaluation of the newly developed methods. Using the aforementioned end-to-end simulator and including the corresponding instrument error allows to determine the efficacy of the correction methods in terms of temperature errors. It therefore helps to understand which steps of the processing chain are crucial to derive an accurate temperature product. This study thus provides an

error and uncertainty estimation of the data processing used to derive a 2D temperature field, consisting of vertical temperature profiles distributed spatially along the satellite's flight path.

For a comprehensive characterization of gravity waves, however, it is necessary to observe all three dimensions of the temperature field. The instrument's optical design allows for the horizontal splitting of the field of view, enabling to process segments separately to resolve parts of the horizontal temperature variations orthogonal to the LOSs (across-track direction) assuming the measurements are performed along the satellite's flight direction. This innovative approach has been assumed in a simulation study conducted by Chen et al. (2022). Their research illustrates that by deploying two satellites simultaneously, with the assumption that each instrument can provide two temperature data points per tangent altitude, it becomes feasible to capture a substantial portion of the gravity wave spectrum. This approach would not only increase the information content of the data product generated by a single instrument but also potentially reduce the number of satellites required for a constellation, thereby lowering the mission's overall cost. This thesis therefore establishes a novel processing method, which ultimately provides two data points per tangent layer through the split field of view technique.

This thesis is structured to address the following objectives:

- Investigating the impact of self-absorption in the radiative transfer model.
- Assessing the precision of retrieved temperatures from simulated observations taken by AtmoLITE.
- Developing correction methods and evaluating their efficacy in terms of retrieved temperatures.
- Exploring a novel processing technique that utilizes a split field of view to resolve horizontal temperature variations.

First, the theoretical background of the radiative transfer model is introduced in Chap. 2. It is used to estimate the arriving signal strength of the oxygen A-band emissions, which governs the noise level, and therefore the temperature uncertainty. It is also employed in the forward model of the retrieval.

Next, in Chap. 3, the necessary mathematical theory is presented, which is needed to understand the subsequent steps in the data processing. It covers the functionality of a SHI, essential aspects of Fourier-transform spectroscopy, signal and noise analysis, and the theory of the temperature retrieval.

Chapter 4 is dedicated to the assessment of the instrument performance. It starts with the simulation of the arriving radiances using the radiative transfer model from Chap. 2, where the impact of self-absorption is investigated. It continues by examining the performance limits in terms of temperature precision assuming an ideal instrument. Subsequently, instrument errors and the developed correction methods are introduced. The efficacy of the correction methods with respect to the temperature retrieval is evaluated, with corresponding calibration data presented at each step. The extensive calibration data from the INSPIRESat-4 mission is also utilized to simulate an interferogram, allowing for an assessment of overall instrument errors based on measured on-ground data.

In Chap. 5, the novel processing technique is explored that utilizes a split field of view to resolve horizontal temperature variations. The chapter explains the general theory behind this technique and validates it using simulated horizontal temperature variations.

Chapter 2

Radiative transfer of the oxygen A-band emissions

Since the O_2 A-band emissions are observed to derive temperature in the mesosphere and lower thermosphere (MLT), this chapter focuses on the theoretical background of the emission, providing the basis for the radiative transfer model. The model is used to simulate the expected signal strength, which governs the noise level of the instrument and therefore the temperature precision of the observations. The theory on the noise level of the instrument will be discussed in Sec. 3.3 and the resulting temperature precision will be shown in Sec. 4.2. Furthermore, the model is part of the forward model in the retrieval process, which will be introduced in Sec. 3.4.

Within the atmosphere, atoms and molecules can exist in various excitation states and transition between them. An atom or molecule can transfer from a state of higher excitation to a state of lower excitation, emitting a photon which carries the energy difference. This process is referred to as emission. Conversely, it can absorb a photon and move from a lower to a higher excited state, known as absorption. Emission and absorption processes act as sources and sinks of radiation traveling through the atmosphere, respectively. Excited molecules can be found in one of multiple electronic states, where for each electronic state it can be in one of multiple vibrational states. The transitions between different electronic-vibrational states form atmospheric emission and absorption bands. Each band consists of multiple emission lines

resulting from transitions between multiple rotational states. Specifically, the oxygen A-band emission at 762 nm is the electronic transition from the second excited state $O_2(b^1\Sigma_g^+, v = 0)$ to the ground state $O_2(X^3\Sigma_g^-, v = 0)$.

Sec. 2.1 introduces the production and loss mechanisms of the second excited state $O_2(b^1\Sigma_g^+, v = 0)$, which will be used to estimate the number density of excited molecules defining the source of the oxygen A-band emission. The rotational structure of the emission lines is introduced in Sec. 2.2, which relative distribution is used to extract the temperature information. The absorption is considered in the radiative transfer calculations presented in Sec. 2.3, which propagate the emission through the atmosphere along the line of sights (LOSs) as presented in Fig. 1.2. Subsequently, the theory is used to build a radiative transfer model, which is used to estimate the signal strength of the emission arriving at the instrument.

2.1 Production mechanisms of the oxygen A-band emission

This section provides an overview of all collisional and photochemical production mechanisms used to estimate the number density of the second excited state of molecular oxygen, which initiate the generation of the O_2 A-band emission. A detailed description of the dayglow O_2 A-band is given by Bucholtz et al. (1986), Ortland et al. (1998), Sheese (2009), Yankovsky and Manuilova (2006), Yankovsky and Vorobeva (2020) and Zarboo et al. (2018). A schematic overview of the reactions forming the excited state is shown in Fig. 2.1. The production of the emission can be split in three sources.

First, the excited state can be produced by photon absorption in the atmospheric bands. Bucholtz et al. (1986) show that the γ-band absorption from $O_2(X^3\Sigma_g^-, v = 0)$ to $O_2(b^1\Sigma_g^+, v = 2)$ can be neglected and hence is not shown in Fig. 2.1. Only the absorption in the A- and B-bands is therefore considered. The excited molecules in $O_2(b^1\Sigma_g^+, v = 1)$ are rapidly deactivated to $O_2(b^1\Sigma_g^+, v = 0)$ via a quenching process. Slanger et al. (1997) argue that the B-band emission from $O_2(b^1\Sigma_g^+, v = 1)$ to $O_2(X^3\Sigma_g^-, v = 0)$ at 686 nm is much smaller compared to the latter quenching process and is therefore neglected in the presented model. However, the emission in the $(1, 1)$ band is a significant deactivation process and is considered

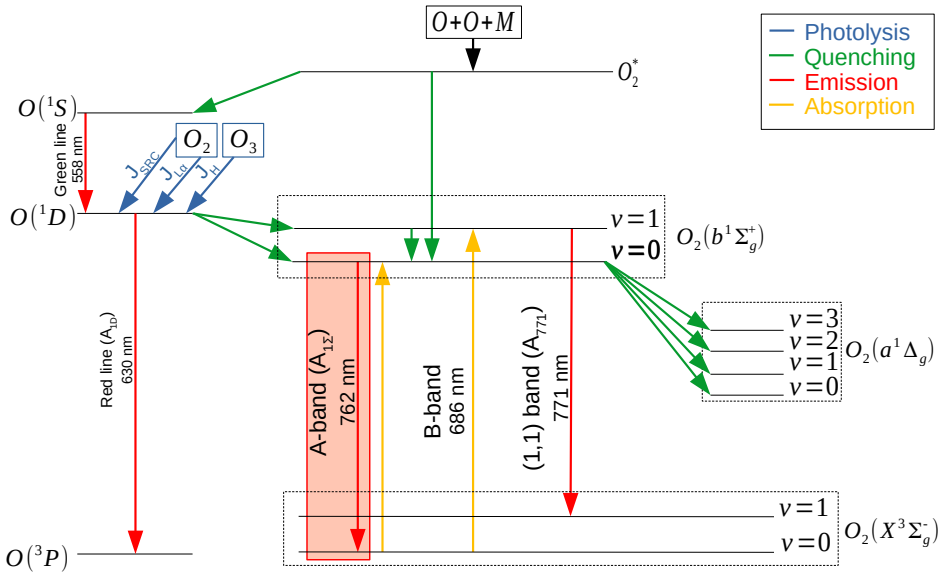

Figure 2.1: Schematic of production of excited state $O_2(b^1\Sigma_g^+, v = 0)$; only transitions and energy levels used in the model are shown.

when calculating the number density of the excited state $O_2(b^1\Sigma_g^+, v = 0)$. The second source is due to photolysis of O_2 in the Schumann-Runge continuum (J_{SRC}) and at Lyman-α ($J_{L\alpha}$) and due to the photolysis of O_3 in the Hartley band (J_H). It produces highly excited atomic oxygen $O(^1D)$, which transforms to $O_2(b^1\Sigma_g^+)$ due to collisional de-excitation with O_2 in ground state. The third source is a chemical source, independent of instantaneous solar radiation, and therefore active even during night time. This process originates from a three-body recombination of atomic oxygen, producing highly excited O_2^*, which represents any of the four states below the first dissociation limit, as discussed by Zarboo et al. (2018). $O_2(b^1\Sigma_g^+)$ is subsequently produced via quenching processes, which will be explained in detail at the end of this section. This process was first described by Barth and Hildebrandt (1961) and is called Barth process.

Following Sheese (2009), the number density of the excited state $O_2(b^1\Sigma_g^+, v = 0)$ within the A-band is given by

$$n = \frac{P_{A-band} + P_{B-band} + P_{Phot_{O_3}} + P_{Phot_{O_2}} + P_{Barth}}{P_{loss}} \tag{2.1}$$

where the nominator and denominator represent the production and loss terms, respec-

tively. In the following, the notation [·] represents the number density of a molecule. The loss rate can be calculated by

$$P_{loss} = A_{1\Sigma} + k_0[N_2] + k_3[O_3] + k_4[O_2] + k_6[O] \tag{2.2}$$

where k_0, k_3, k_4 and k_6 corresponds to the quenching rate coefficients of the reactions 19–22 in Table 2.1 and $A_{1\Sigma}$ is the sum of the Einstein coefficients of all radiative transitions from the excited state $O_2(b^1\Sigma_g^+, v = 0)$ corresponding to reaction 18 in Table 2.1. The A-band photo-absorption is calculated by

$$P_{A-band} = g_A[O_2] \tag{2.3}$$

where g_A is the photodissociation rate of the reaction 1 in Table 2.1. The B-band photo-absorption contributes to $O_2(b^1\Sigma_g^+, v = 0)$ via the quenching reactions 4–7 and is calculated by

$$P_{B-band} = K[O_2(b^1\Sigma_g^+, v = 1)] \tag{2.4}$$

$$K = K_{0B}[O] + K_{1B}[O_2] + K_{2B}[N_2] \tag{2.5}$$

$$[O_2(b^1\Sigma_g^+, v = 1)] = \frac{g_A[O_2]}{A_{771} + K + K_{3B}[O_3]} \tag{2.6}$$

where K_{0B}, K_{1B}, K_{2B} and K_{3B} are the quenching rates of reactions 4–7, g_B is the photodissociation rate of the reaction 2 and A_{771} is the Einstein coefficient of the (1,1)-band emission denoted by reaction 3 in Table 2.1.

The production rate of the excited $O_2(b^1\Sigma_g^+)$ due to the photolysis of O_2 and O_3 can be calculated by

Index	Reaction	Rate	Value	Unit	Reference
1	$O_2(X^3\Sigma_g^-) + hv(\lambda = 762.7nm) \rightarrow O_2(b^1\Sigma_g^+, v = 0)$	g_A	5.94×10^{-9}	s^{-1}	Bucholtz et al. (1986)
2	$O_2(X^3\Sigma_g^-) + hv(\lambda = 689.6nm) \rightarrow O_2(b^1\Sigma_g^+, v = 1)$	g_B	3.54×10^{-10}	s^{-1}	Bucholtz et al. (1986)
3	$O_2(b^1\Sigma_g^+, v = 1) \rightarrow O_2(X^3\Sigma_g^-) + hv(\lambda = 771nm)$	A_{771}	7.0×10^{-2}	s^{-1}	Rothman et al. (2013)
4	$O_2(b^1\Sigma_g^+, v = 1) + O \rightarrow O_2(b^1\Sigma_g^+, v = 0) + 0$	k_{0B}	4.5×10^{-12}	cm^3s^{-1}	Yankovsky and Manuilova (2006)
5	$O_2(b^1\Sigma_g^+, v = 1) + O_2 \rightarrow O_2(b^1\Sigma_g^+, v = 0) + O_2$	k_{1B}	$4.2 \times 10^{-11} e^{\frac{-312}{T}}$	cm^3s^{-1}	Yankovsky and Manuilova (2006)
6	$O_2(b^1\Sigma_g^+, v = 1) + N_2 \rightarrow O_2(b^1\Sigma_g^+, v = 0) + N_2$	k_{2B}	5.0×10^{-13}	cm^3s^{-1}	Yankovsky and Manuilova (2006)
7	$O_2(b^1\Sigma_g^+, v = 1) + O_3 \rightarrow 2O_2 + O$	k_{3B}	3.0×10^{-10}	cm^3s^{-1}	Yankovsky and Manuilova (2006)
8	$O_2(X^3\Sigma_g^-) + hv(137nm \leq \lambda \leq 175nm) \rightarrow O(^3P) + O(^1D)$	J_{SCR}	see Sec. 2.1	s^{-1}	Sheese (2009)
9	$O_2(X^3\Sigma_g^-) + hv(\lambda = 121.6nm) \rightarrow O(^3P) + O(^1D)$	J_{L_α}	see Sec. 2.1	s^{-1}	Sheese (2009)
10	$O_3 + hv(\lambda \leq 310nm) \rightarrow O(^1D) + O_2(a^1\Delta_g)$	J_H	7.1×10^{-3}	s^{-1}	Sheese (2009)
11	$O(^1D) \rightarrow O + hv(\lambda = 630nm)$	A_{1D}	6.81×10^{-3}	s^{-1}	Rothman et al. (2013)
12	$O(^1D) + O_2 \rightarrow O + O_2(b^1\Sigma_g^+, v = 0)$	φk_1	0.95, see row 13	unitless	Green et al. (2000)
13	$O(^1D) + O_2 \rightarrow O + O_2$	k_1	$3.3 \times 10^{-11} e^{\frac{55}{T}}$	cm^3s^{-1}	Sander et al. (2011)
14	$O(^1D) + N_2 \rightarrow O + N_2$	k_2	$2.15 \times 10^{-11} e^{\frac{110}{T}}$	cm^3s^{-1}	Sander et al. (2011)
15	$O + O + M \rightarrow O_2^* + M\,(M = N_2, O_2)$	k_5	$4.7 \times 10^{-33} \left(e^{\frac{300}{T}}\right)^2$	cm^6s^{-1}	Campbell and Gray (1973)
16	$O_2^* + O_2 \rightarrow O_2(b^1\Sigma_g^+, v = 0) + O_2$	C_{O2}	5.7	unitless	McDade et al. (1986)
17	$O_2^* + O \rightarrow O_2(b^1\Sigma_g^+, v = 0) + O$	C_O	17	unitless	McDade et al. (1986)
18	$O_2(b^1\Sigma_g^+, v = 0) \rightarrow O_2(X^3\Sigma_g^-, v = 0) + hv(762nm)$	$A_{1\Sigma}$	8.78×10^{-2}	s^{-1}	Rothman et al. (2013)
19	$O_2(b^1\Sigma_g^+, v = 0) + N_2 \rightarrow O_2(a^1\Delta_g, v = 0, 2)/O_2(X^3\Sigma_g^-, v = 9)$	k_0	$8.0 \times 10^{-20} T^{1.5} e^{\frac{503}{T}}$	cm^3s^{-1}	Zagidullin et al. (2017)
20	$O_2(b^1\Sigma_g^+, v = 0) + O_3 \rightarrow O_2(a^1\Delta_g, v = 0) + O_3$	k_3	$3.5 \times 10^{-11} e^{\frac{-135}{T}}$	cm^3s^{-1}	Sander et al. (2011)
21	$O_2(b^1\Sigma_g^+, v = 0) + O_2 \rightarrow O_2(a^1\Delta_g, v \leq 3) + O_2(X^3\Sigma_g^-, v \leq 3)$	k_4	$7.4 \times 10^{-17} T^{0.5} e^{\frac{-1104.7}{T}}$	cm^3s^{-1}	Zagidullin et al. (2017)
22	$O_2(b^1\Sigma_g^+, v = 0) + O \rightarrow O_2(a^1\Delta_g, v = 0)/O_2(X^3\Sigma_g^-, v = 0) + O$	k_6	8.0×10^{-14}	cm^3s^{-1}	Sander et al. (2011)

Table 2.1: Photochemical reaction parameters used in the simulation of the A-band production and loss mechanisms

$$P_{Phot_{O_2}} = \frac{(J_{SCR} + J_{L_\alpha})[O_2]\varphi k_1[O_2]}{A_{1D} + k_1[O_2] + k_2[N_2]} \tag{2.7}$$

$$P_{Phot_{O_3}} = \frac{J_H[O_3]\varphi k_1[O_2]}{A_{1D} + k_1[O_2] + k_2[N_2]} \tag{2.8}$$

where J_{SCR}, J_{L_α} and J_H are the photolysis coefficients of the reaction 8, 9 and 10 in Table 2.1, respectively. A_{1D} denotes the Einstein-coefficient of the atomic oxygen red lime emission presented in reaction 11. The quenching rates k_1 and k_2 refer to the reactions 13 and 14, and φ characterizes the fraction of reaction 13 that produces excited $O_2(b^1\Sigma_g^+, v = 0)$, corresponding to reaction 12. J_H is provided by Sheese (2009). The photolysis rates J_{SCR} and J_{L_α} are calculated following Sheese (2009) and are determined by the absorption rate of oxygen molecules concerning the spectral flux available at specific atmospheric locations. The spectral flux is derived from the spectral solar flux at the top of the atmosphere using the Beer-Lambert law. In this context, the absorption cross-section of oxygen at the solar Lyman-α line at 121.6 nm and the absorption quantum yield are set to $1.0 \times 10^{-20}\,\mathrm{cm}^2$ and 0.55, respectively, as outlined in (Reddmann and Uhl, 2003). Regarding the Schumann-Runge continuum, the

absorption cross-section is described by Yoshino et al. (2005) across the specified wavelength range, and the absorption quantum yield is set to 1 (Brasseur and Solomon, 2005). The spectral solar flux at the top of the atmosphere is taken from the SORCE Solar Spectral Irradiance and can be obtained from `https://lasp.colorado.edu/home/sorce/data/`.

The production rate attributed to the Barth process is modeled following the approach outlined by McDade et al. (1986). This process involves the three-body recombination of atomic oxygen, leading to the creation of highly excited O_2^*. Subsequently, this excited state undergoes de-excitation, resulting in the formation of $O_2(b^1\Sigma_g^+)$ through a direct quenching process with O_2, or through a multi-step process in which O_2^* is quenched with O, involving $O(^1S)$ and $O(^1D)$ as intermediates. McDade et al. (1986) introduces a model with two fitting parameters, namely C_{O_2} and C_O. These parameters are associated with the quenching rates of O_2^* with O_2 and O, corresponding to reactions 16 and 17, respectively, as detailed in Table 2.1. These fitting parameters were derived from rocket measurements, which provided data on atomic oxygen concentrations and O_2 A-band emissions. The production rate is then given by

$$P_{Barth} = \frac{k_5[O]^2[M][O_2]}{C_{O_2}[O_2] + C_O[O]} \tag{2.9}$$

where k_5 represents the quenching rate associated with reaction 15, as specified in Table 2.1. The results of simulations related to the production mechanisms are discussed in Sec. 4.1.2.

2.2 Rotational structure of the oxygen A-band emission

As introduced in the chapter's opening, the oxygen A-band emission represents the electronic transition from the second excited state, $O_2(b^1\Sigma_g^+, v = 0)$, to the ground state, $O_2(X^3\Sigma_g^-, v = 0)$. This electronic transition consists of multiple rotational transitions, with each transition generating three emission lines due to the presence of two unpaired electrons in the ground-state O_2, leading to spin angular momentum effects (Ritter and Wilkerson, 1987). The distribution of these emission lines will be employed to derive temperature within the retrieval process in Section 3.4.

It is important to highlight that the temperature derived from this distribution corre-

sponds to the rotational temperature, which matches the kinetic temperature only under local thermodynamic equilibrium (LTE) conditions. LTE prevails when collisional processes predominantly determine the population density of different energy levels of molecules. However, as altitude increases, decreasing pressure causes radiative processes, such as photon absorption and emission, becoming more important compared to collisions, leading to a state of non-LTE. For the O_2 A-band emission corresponding to an electronic transition, non-LTE conditions are encountered in the MLT region. Nonetheless, it is generally assumed that rotational LTE prevails, resulting in the derived rotational temperature aligning closely with the kinetic temperature.

The concept of rotational LTE is discussed by López-Puertas and Taylor (2001), who point out that rotational levels for most atmospheric molecules are in LTE for high altitudes up in the thermosphere. This is due to the small energy differences between rotational states, requiring only a small number density of collision partners to achieve thermal equilibrium. Additionally, the relatively long radiative lifetime of 11.4 s for the excited $O_2(b^1\Sigma_g^+)$, calculated as the inverse of the Einstein coefficient of the O_2 A-band emission, gives sufficient time for thermal equilibrium to be established. The same argument applies to the spin distribution, as the energy differences between spin states are even smaller. This concept of rotational LTE finds widespread application in temperature derivation from the oxygen A-band, as seen in the studies of Englert et al. (2017), Gumbel et al. (2020), and Sheese et al. (2010).

Following López-Puertas and Taylor (2001), the number of excited O_2 molecules of a specific upper rotational state, can be calculated by

$$n_i(T) = n\frac{g_i}{Q(T)}\exp\left(\frac{-c_2 E_i}{T}\right) \tag{2.10}$$

where i indicates the upper state of the transition, c_2 is the second radiation constant, E_i and g_i denote the energy and the degeneracy of the upper state, respectively, T the rotational temperature, and n is the number density calculated by Eq. (2.1). $Q(T)$ is the temperature dependent rotational partition function, defined by

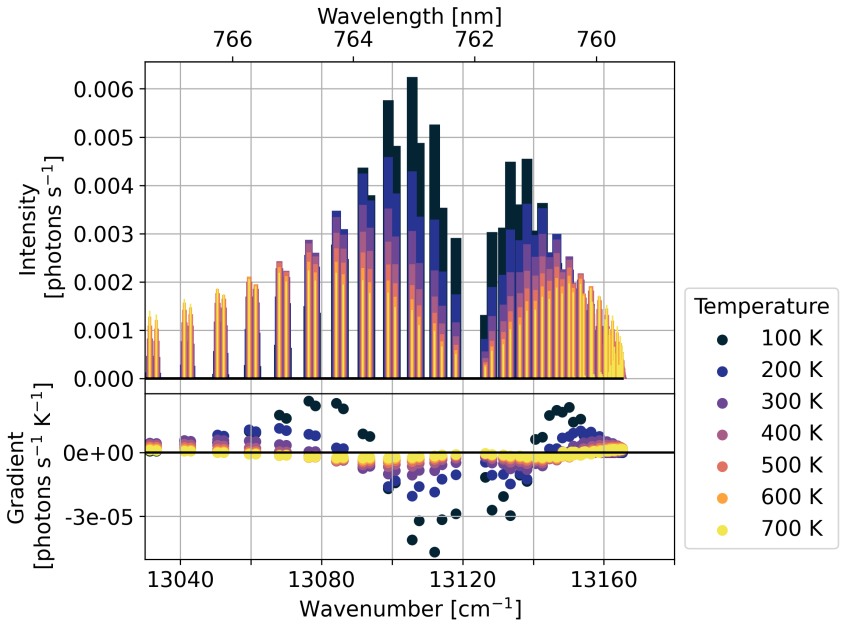

Figure 2.2: Rotational distribution of the O_2 A-band emission lines evaluated for different temperatures; the gradient in the lower panel is calculated by finite difference along the temperature axis with sampling size of 1 K; the gradient shows a lower sensitivity for higher temperatures.

$$Q(T) = \sum_{i \in I} g_i \exp\left(\frac{-c_2 E_i}{T}\right), \tag{2.11}$$

where I is the set of all possible upper states which can be determined by the unique degeneracy g_i. Thus, the term is normalized by $Q(T)$ such that Eq. (2.10) describes the distribution of the number densities of the rotational states. The line strength of the emissions can be then calculated by

$$S_{i,j} = A_{i,j} n_i \tag{2.12}$$

where $A_{i,j}$ is the Einstein coefficient corresponding to the transition from the upper rotational state i to the lower rotational state j. The required spectroscopic parameters of the emission lines are given by the HITRAN database (Gamache et al., 2021; Gordon et al., 2022; Rothman et al., 2013). Figure 2.2 displays the line strengths of emissions for various temperatures with $n = 1$, revealing the radiative rate of each transition within the rotational band.

In this representation, the splitting of a rotational transition into three emission lines due to the spin angular momentum is partially visible. Two emission lines appear as pairs, while the third line, although present, has significantly lower intensity (not visible in the figure). This can be particularly seen in the P-branch below $13.120\,\mathrm{cm}^{-1}$. A similar pattern is observed in the Q-branch above $13.120\,\mathrm{cm}^{-1}$, where some triplets overlap, especially around $13.160\,\mathrm{cm}^{-1}$. Concerning temperature dependence, lower temperatures yield higher central frequencies with decreasing intensity toward the band edges. Higher temperatures result in a broader intensity distribution. Notably, the sensitivity to temperature decreases with higher temperatures. Further discussion on the varying sensitivity if given in Sec. 4.2.

2.3 Radiative Transfer

The radiative transfer describes the propagation of the O_2 A-band emission through the atmosphere towards the instrument. This propagation is modeled as traveling along the LOS, illustrated in Fig. 1.2. Along this path, the radiance is attenuated due to self-absorption by O_2 molecules in ground state. This effect is modeled by Beer–Lambert law. For the presented observational method, scattering and refraction effects are neglected. The radiance arriving at the instrument can be expressed by an integral over the LOS corresponding to a given tangent altitude z denoted by

$$R_z(\sigma) = \frac{1}{4\pi} \int_0^\infty J(\sigma, s) \exp\left(- \int_s^\infty k_a(\sigma, s) ds' \right) ds, \tag{2.13}$$

where σ is the wavenumber and s refers to the LOS distance from the instrument, J denotes the source function, and k_a is the absorption coefficient. The exponential term is referred to as the transmittance, a measure of how much radiance from a particular position s reaches the instrument. Also for the self-absorption, the question arises regarding the validity of LTE. López-Puertas and Taylor (2001) show in their Sec. 3.6.3 that if the ratio of molecules in the upper state to those in the lower state is close to zero, the absorption in non-LTE approximates the expression in LTE. For the O_2 A-band emission, the ratio is always smaller than 10^{-5} as shown in Appx. A.4 and thus, the self-absorption can be modeled as in LTE.

Before defining the source function and absorption coefficient, the two broadening effects of spectral lines needs to be introduced. Emission lines can be widened due to collisions between molecules, referred to as pressure broadening, and due to thermal motions of the molecules, referred to as Doppler broadening. Typically, both broadening effects are considered, which is mathematically described by a Voigt line shape as defined in Appx. A.6.3. However, within the altitude span investigated in this study, ranging from 60 km to 140 km, pressure broadening can be disregarded, as detailed in Appx. A.6.3. Consequently, only Doppler broadening is considered in the radiative transfer model. Following Brasseur and Solomon (2005), the latter is described by a Gaussian function given by

$$D_{ij}(\sigma, T) = \sqrt{\frac{\ln 2}{\pi(\alpha_{D_{ij}}(T))^2}}\, e^{-\ln 2\left(\frac{\sigma-\sigma_{ij}}{\alpha_{D_{ij}}(T)}\right)^2}, \tag{2.14}$$

where T is the temperature and σ_{ij} the wavenumber of the emission representing the mean of the Gaussian function. The half width at half maximum (HWHM) is denoted by

$$\alpha_{D_{ij}}(T) = \frac{\sigma_{ij}}{c}\sqrt{\frac{2N_A kT\ln 2}{M}}, \tag{2.15}$$

where N_A refers to the Avogadro constant, c denotes the speed of light and M is the molar mass of the isotopologue. All three parameters can be found in the HITRAN data set (Rothman et al., 2013).

The source function is determined by the spontaneous emission, which is defined using a line-by-line model denoted by

$$J(\sigma, s) = \sum_{(ij)\in I_J} A_{ij} n_i(s) D_{ij}(\sigma, T(s)), \tag{2.16}$$

where I_J is the set of all transitions within in the O_2 A-band from upper state i to lower state j, A_{ij} refers to the Einstein coefficient, n_i presents the number density of excited O_2 in upper state i, defined by Eq. (2.10), D_{ij} is the corresponding line shape and T denotes the temperature at position s. The absorption coefficient is modeled in a similar way denoted by

$$k_a(\sigma, s) = \sum_{(ij)\in I_J} n(s) S_{ij}(s) D_{ij}(\sigma, T(s)), \tag{2.17}$$

where n is the number density of O_2 in ground state and S_{ij} refers to the line strength, which can be calculated following Šimečková et al. (2006).

This concludes the theory needed for the forward calculation. Results of radiative transfer simulation are presented in Sec. 4.1.2. Discussions on implementation, limitations and possible improvements of the forward model are given in Appx. A.5.

Chapter 3

Mathematical modeling of a spatial heterodyne interferometer for temperature derivation

As introduced in Chap. 1, a new space-borne instrument is developed by Kaufmann et al. (2018) to derive temperature in the mesosphere and lower thermosphere (MLT). The instrument observes the oxygen A-band emissions at 762 nm using a spatial heterodyne interferometer (SHI).

This chapter gives an overview of the observational method focusing on the mathematical tools necessary to ensure accurate data processing. The general principle of a SHI, which is based on Fourier-transform spectroscopy, is introduced in Sec. 3.1. Subsequently in Sec. 3.2, the mathematical theory of Fourier-transform spectroscopy is introduced which is needed to understand the data processing and analysis throughout this work. Some thoughts on the expected signal and noise level are given in Sec. 3.3. The signal-to-noise ratio (SNR) governs the temperature precision and is used throughout Chap. 4 when assessing the instrument performance. This chapter is concluded with the theory of the temperature retrieval in Sec. 3.4.

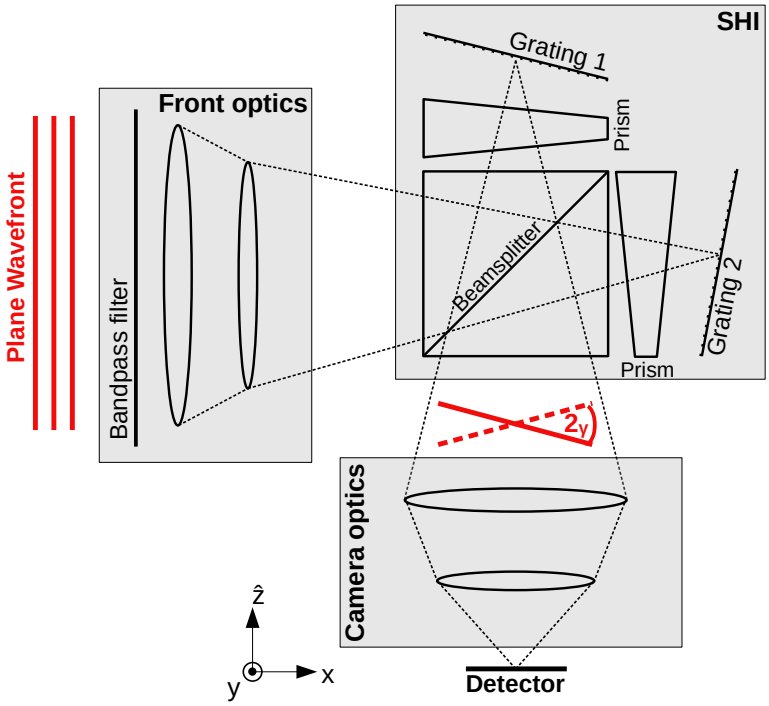

Figure 3.1: Schematic of the SHI including the two optical systems; the coordinate system refers to the detector plane so that the horizontal and vertical axis of the detector refer to the x- and y-axis, respectively.

3.1 Spatial heterodyne interferometer

A spatial heterodyne interferometer (SHI) is similar to a Michelson interferometer, but the two mirrors are replaced by fixed tilted gratings. This measurement method was firstly developed by Connes (1958) and with the subsequent availability of imaging detectors, it was further developed to remote sensing methods by e.g. Cardon et al. (2003), Harlander et al. (1992), Langille et al. (2018) and Watchorn et al. (2001).

Figure 3.1 shows a schematic of the SHI including the two optical systems. The incident light, traveling along the x-axis, is imaged by the front optics onto diffraction gratings. The camera optics images the gratings onto a 2-dimensional focal plane array (FPA). Therefore, the spatial distribution of the atmospheric scene is preserved within the instrument. The SHI produces an interference pattern, which is superposed along the detector's horizontal x-axis. One measurement therefore contains spatial information along the detector's vertical y-axis, and superimposed spectral and spatial information along the x-axis. It should be noted

that the atmospherics vertical z-axis is mapped onto the detector's vertical y-axis and that the detector's horizontal x-axis correspond to the horizontal across-track dimension in the atmosphere. The axis perpendicular to the detector plane is denoted by $\hat{z}$.

The SHI generates the interference pattern as follows: Light of a frequency within the spectral bandpass enters the instrument along the x-axis and is split into two waves by the beam splitter. These waves are diffracted and reflected by the gratings and subsequently recombined at the beam splitter, creating an interference pattern. This pattern is then directed to the detector. When multiple emissions within the bandpass are considered, the interferogram consists of multiple superimposed interference patterns along the x-axis, which can be described as sinusoidal waves. The spatial frequency of the produced fringe pattern follows from the grating equation, denoted by

$$\sigma(\sin\,\theta_L + \sin(\theta_L - \gamma)) = \frac{m}{d}, \tag{3.1}$$

where σ is the wavenumber of the incoming light, θ_L refers to the Littrow angle, d^{-1} is the grating groove density, m is the diffraction order (here set to 1) and γ the outgoing diffraction angle. The Littrow wavenumber is the wavenumber where $\gamma = 0$, thus

$$\sigma_L = \frac{m}{2\sin(\theta_L)d}. \tag{3.2}$$

Using Taylor expansion, Harlander et al. (1992) show that the spatial frequency is dependent on the wavenumber by

$$f(\sigma) \approx 4(\sigma - \sigma_L)\tan(\theta_L)M^{-1}, \tag{3.3}$$

where M^{-1} is the magnification factor introduced by the camera optics. This equation shows that the relation between spatial frequency and wavenumber is symmetric around the Littrow wavenumber. Following Roesler and Harlander (1990), an ideal one-dimensional interferogram along the x-axis can be described by

$$I(x) = \int_{b_0}^{b_1} R(\sigma)d\sigma + \int_{b_0}^{b_1} R(\sigma)\cos(2\pi f(\sigma)x)d\sigma, \tag{3.4}$$

where R is the spectral radiance and b_0 and b_1 are the lower and upper bound of the spectral filter, respectively. The instrument represents light of a certain frequency by a cosine wave with a transformed spatial frequency and thus, performs an inverse Fourier transform. Note that Deiml (2018) gives a detailed mathematical derivation of the above presented equations in their Appx. B.2.1. The interferogram consists of a non-modulated and modulated part, represented by the first and second terms in Eq. (3.4), respectively. The temperature information is inherent in the spectral radiance R, as seen in the radiative transfer equation (Eq. (2.13), Eq. (2.16), Eq.(2.17)). In the interferogram, this information is only imprinted into the modulated part. The non-modulated part is therefore omitted during the processing, as discussed in detail in Sec. 4.3.4.

3.2 Fourier-transform spectroscopy

As explained in Sec. 3.1, the instrument performs mathematically an inverse Fourier transformation on the incident light. The Fourier transformation is thus used in the data processing to convert the interferogram back to a spectrum, which is introduced in Sec 3.2.1 including its mathematical properties used throughout the work. Due to the finite dimension of the FPA and the sampling of the interferogram by discrete pixels, the resulting spectrum differs from the spectrum of the incident light. The finite dimension broadens the emission lines largely which is captured by the instrument line shape (ILS), introduced in Sec. 3.2.2. The pixels sample the continuous interferogram falling onto the FPA, leading to aliasing effects and a slight modulation of the ILS, which is covered in Sec. 3.2.3. Moreover, an ILS with more advantageous properties can be achieved through the use of apodization techniques. The detailed discussion of apodization will be presented in Section 3.2.4.

3.2.1 Fourier transformation

The one-dimensional continuous Fourier Transform is given by

$$S(\kappa) := \mathcal{F}(I)(\kappa) = \int_{-\infty}^{\infty} I(x) e^{-i2\pi\kappa x} dx \tag{3.5}$$

where $\mathcal{F}$ denotes the one-dimensional Fourier transform operator, I is the modulated part of the interferogram defined in Eq. (3.4), x refers to the spatial abscissa of the interferogram, and κ is the spatial frequency of the resulting spectrum as defined in Eq. (3.3). The Fourier transform is complex by definition, where the real and imaginary parts are the cosine and sine transformation, respectively. Instead of presenting the imaginary and real part, polar coordinates are often applied to represent the Fourier transform by the absolute value, also called the power or magnitudinal spectrum, and the phase denoted by

$$S(\kappa) = |S(\kappa)|e^{-i\Phi(\kappa)}dx \tag{3.6}$$

where the phase $\Phi(\kappa)$ is given by $\arctan2(\mathrm{Im}(\kappa), \mathrm{Re}(\kappa))$. The absolute value represents the amplitude of a wave with a respective frequency and and the phase represents the phase shift of the wave. Since the ideal interferogram consists only of cosine waves without phase shift with respect to the center, the imaginary part, and therefore the phase is zero. In general, the Fourier transform of a symmetric function has a zero imaginary part, and therefore a phase equal to zero. Applying the Fourier transformation given in Eq. (3.5) to the modulated part of the interferogram given in Eq. (3.4) results in

$$\mathcal{F}(I)(\kappa) = \frac{1}{2}\int_{b_0}^{b_1}\int_{-\infty}^{\infty} R(\sigma)\left(e^{i2\pi f(\sigma)x} + e^{-i2\pi f(\sigma)x}\right)e^{-i2\pi\kappa x}dxd\sigma \tag{3.7}$$

$$= \frac{1}{2}R(|\kappa|) \tag{3.8}$$

where Euler's formula and the exponential definition of a Dirac delta function is applied. It shows that the spectral intensity of the radiation is halved and mirrored around the zero frequency. Note that the spectral axis of the Fourier transform is transformed from wavenumber to spatial frequencies, following Eq. (3.3). The spectrum can be converted back to the interferogram by the one-dimensional inverse continuous Fourier transformation denoted by

$$I(x) = \mathcal{F}^{-1}(S)(x) = \frac{1}{2\pi}\int_{-\infty}^{\infty} S(\kappa)e^{i2\pi\kappa x}d\kappa. \tag{3.9}$$

The discrete Fourier-transformation is defined by

$$S[m] = \mathcal{F}(I)[m] = \frac{1}{N} \sum_{n=0}^{N-1} I[n] e^{-i2\pi \frac{mn}{N}} \tag{3.10}$$

and its inverse is given by

$$\mathcal{F}(S)[m] = \sum_{m=0}^{N-1} S[m] e^{i2\pi \frac{mn}{N}} \tag{3.11}$$

where N is the number of samples and n and m the spatial and spectral sample count. Note that the discrete Fourier transform is periodic about the Nyquist-frequency, which is the upper limit on the resolvable frequency defined by $\pm\frac{1}{2p}$ (Nyquist, 1928; Shannon, 1998). If the continuous signal consists only of frequencies smaller than the Nyquist limit, the sampled signal is free of distortion known as aliasing. More details is given in Sec. 3.2.3.

The convolution theorem states states that the Fourier transform of the point-wise product of two functions is equal to the convolution of their individual Fourier transforms, and vice versa. This can be expressed as

$$\mathcal{F}(X \cdot Y) = \mathcal{F}(X) * \mathcal{F}(Y) \tag{3.12}$$

$$\mathcal{F}(X * Y) = \mathcal{F}(X) \cdot \mathcal{F}(Y) \tag{3.13}$$

where $\cdot$ and $*$ indicate the point-wise product and the convolution of two functions, respectively. Note that the convolution theorem holds for the continuous and discrete case.

3.2.2 Concept of instrument line shape

Due to the spatial limitation of the interferogram in a real instrument, the infinite interferogram defined in Eq. (3.4) is multiplied with a boxcar function denoted by

$$I(x) = \Pi(x) \int_{b0}^{b1} R(\sigma) \cos(2\pi\sigma x) d\sigma \tag{3.14}$$

where the non-modulated part is omitted and Π is denoted by

$$\Pi(x) = \begin{cases} 1 & \text{if } x \in [-L, L] \\ 0 & \text{else} \end{cases} \tag{3.15}$$

where L is the half of the interferogram length. Taking the Fourier transformation of Eq. (3.14) gives

$$\mathcal{F}(I)(\sigma) = \mathcal{F}(\Pi)(\sigma) * R(\sigma) \tag{3.16}$$

$$= 2L\,\mathrm{sinc}(2\pi\sigma L) * R(\sigma) \tag{3.17}$$

where the convolution theorem from Eq. (3.12) is used in Eq. (3.16). The ILS is thus defined by the sinc function. The resolution is measured by the full width at half maximum (FWHM) of the main lobe, which is inversely proportional to the length of the boxcar. The incident spectrum is convolved with the sinc function as presented in Eq. (3.17), resulting in an output with spurious oscillations due to the large side lobes of the sinc function. To reduce these oscillations, apodization can be applied, which is introduced in Sec. 3.2.4. Note however that following the uncertainty principle, the finite support of any window function due to the finite dimension of the detector entails an infinite support of the ILS in the Fourier space (Folland and Sitaram, 1997).

3.2.3 Sampling theory

The continuous interferogram is discretely sampled by the detector pixels, which corresponds to a multiplication with an infinite impulse train denoted by

$$I_s(x) = I(x)\,\text{Ш}_p(x) \tag{3.18}$$

where p is the pixel pitch defining the sampling rate of the impulse train. Applying the convolution theorem, the Fourier transform of the sampled interferogram is given by

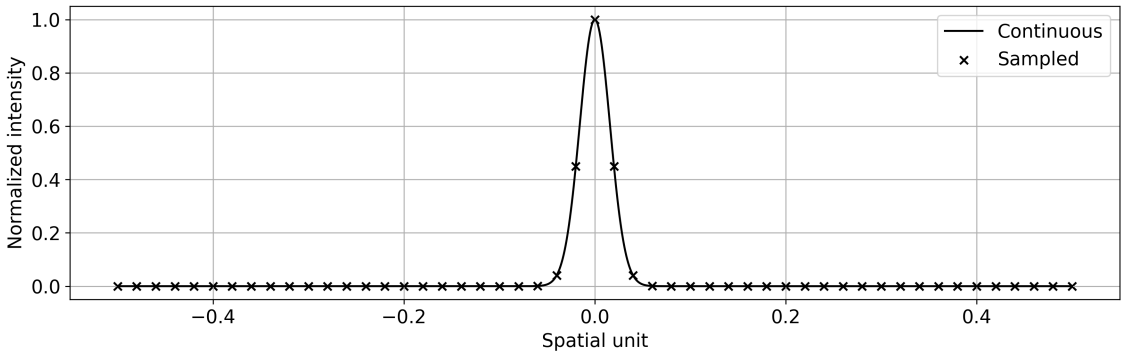

(a)

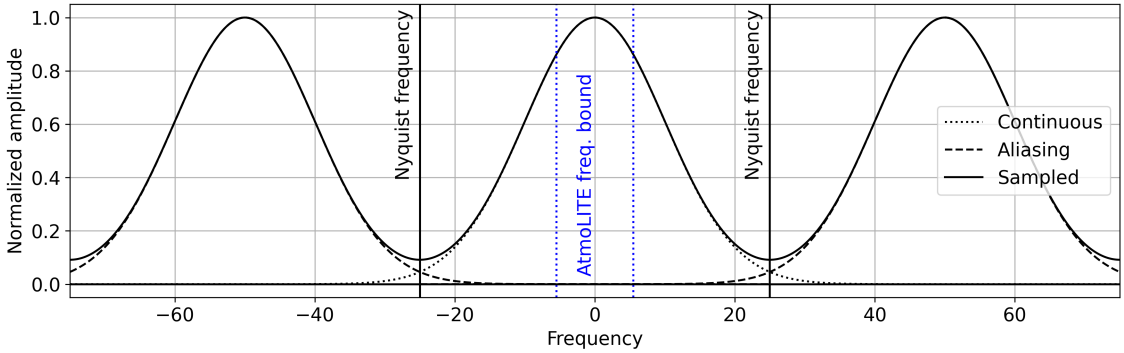

(b)

Figure 3.2: (a) Continuous and sampled Gaussian function in spatial domain; (b) the continuous analytical Fourier transform and its periodic extension (Aliasing); the sampled spectrum resulting from the discrete Fourier transformation of the sampled Gaussian function is the sum of the continuous spectrum and its aliased frequencies; note that the sampled spectrum is interpolated using zero-padding.

$$\mathcal{F}(I_s)(\kappa) = \mathcal{F}(I)(\kappa) * \text{Ш}_{p^{-1}} \tag{3.19}$$

since the Fourier transform of an infinite impulse train is again an infinite impulse train with an inverse sampling rate, denoted by p^{-1}. As shortly mentioned in Sec. 3.2.1, the sampling of the signal induces an upper limit on the resolvable frequency given by $\pm\frac{1}{2p}$, called the Nyquist frequency. However, if the spectrum consists of frequencies above the Nyquist limit, the impulse train $\text{Ш}_{p^{-1}}$ is responsible for folding frequencies beyond Nyquist limit into the resolvable frequency range, which is commonly known as aliasing. An example is shown in Fig. 3.2. Hereby, a Gaussian function in the spatial domain is taken and coarsely sampled

shown in Fig. 3.2a. The Fourier transform of a Gaussian is a Gaussian as well. Since the discrete Fourier-transform is periodic about the Nyquist frequency by definition, as discussed in Sec. 3.2.1, the continuous Fourier transform and its periodic extensions, also known as aliased frequencies, are shown in Fig. 3.2b. The spectrum resulting from the discrete Fourier transform is then the sum of the continuous spectrum and its aliased frequencies inducing aliasing errors. Most applications in Fourier transform spectroscopy ensure that the Nyquist frequency is well beyond the relevant spectral range. Applying a bandpass filter helps restrict the frequencies to an area of interest. For example, in the case of the AtmoLITE instrument, only 21.9 % of the available spectral range is used (indicated by the dotted blue lines in Figure 3.2b), these measures prevent aliasing effects from occurring in the spectral region of interest.

During the sampling processes, the intensity falling onto the FPA is integrated over the pixel, which can be modeled by a convolution of the interferogram with a boxcar, which width is equal to the pixel pitch. Including the boxcar to model a finite interferogram as explained in Sec. 3.2.2 and the sampling by a impulse train as shown above, a discretely sampled interferogram of finite extent can be described by

$$I_s(x) = (I(x) * \Pi_p(x))\, \Pi_{2L}(x)\, \text{Ш}_p(x) \tag{3.20}$$

where Π_p and Π_{2L} are boxcar function with width equal to p, the pixel width, and $2L$, the interferogram length. Applying the convolution theorem, the Fourier transform of the sampled interferogram is given by

$$\mathcal{F}(I_s)(\sigma) = ((R(\sigma) p\, \text{sinc}(\pi\sigma p)) * 2L\, \text{sinc}(2\pi\sigma L)) * \text{Ш}_{p^{-1}}(\sigma). \tag{3.21}$$

Since the pixel pitch p is mostly small by design, it entails a very wide sinc function, where only the bell shape of the main lobe lies within the Nyquist frequency range. It therefore damps the ILS at higher frequencies. In simple terms, the integration process over the pixel pitch results in the blurring of spectral information, with a greater impact on higher frequencies.

3.2.4 Apodization

Following Harris (1978), the idea of apodization can be seen from two viewing points. First, the interferogram is point-wise multiplied with a function which decreases toward the edges to reduce the ringing artifacts caused by the discontinuity at the edges. Second, a window functions is chosen in a way so that its Fourier transform contributes mostly to frequencies close to the zero frequency. In other words, it minimizes the side lobes and maintains the localization of the spectral information. Both strategies remove the oscillations caused by the sinc function. In general, stronger decaying window functions decreases the side lobes more at a cost of an increased FWHM of the main lobe. Apodization therefore can be considered as a trade-off between spectral resolution and removal of the side lobes in the spectral output. Many different apodization functions have been proposed in the last decades. Harris (1978) applies multiples measures to asses different apodization functions and conclude that the resolution of the main lobe, measured by the FWHM, and the maximal absolute value of the first side lobe of the Fourier transform are good measures to asses the performance of an apodization function. Also Kaiser and Schafer (1980) and Barnet et al. (2000) agree on these two measures for their assessments. Filler (1964) proposed the Filler's diagram, which plots the FWHM against the absolute maximum of the first side lobe relative to the sinc function denoted by W/W_{sinc} and $|h/h_{\text{sinc}}|$, respectively. Filler (1964) ran through empirical tests of multiple apodization classes and conclude that there is a mutually dependent boundary between $|h/h_{\text{sinc}}|$ and W/W_{sinc} defined by

$$log_{10}\left|\frac{h}{h_{\text{sinc}}}\right| = 1.939 - 1.401\left(\frac{W}{W_{\text{sinc}}}\right) - 0.597\left(\frac{W}{W_{\text{sinc}}}\right)^2. \tag{3.22}$$

The Norton-Beer apodization functions (see Fig. 3.3) are optimal in the sense of these two measures, because the maximal value of the first side lobe is minimized for a given FWHM of the main lobe. The Norton-Beer apodization therefore follows the second viewing point. Norton and Beer (1976) proposed three apodization functions called Norton-Beer weak, medium and strong corresponding to an increase of the FWHM relative to the sinc function by 20 %, 40 % and 60 %, respectively. Naylor and Tahic (2007) presented an extended version of the Norton-

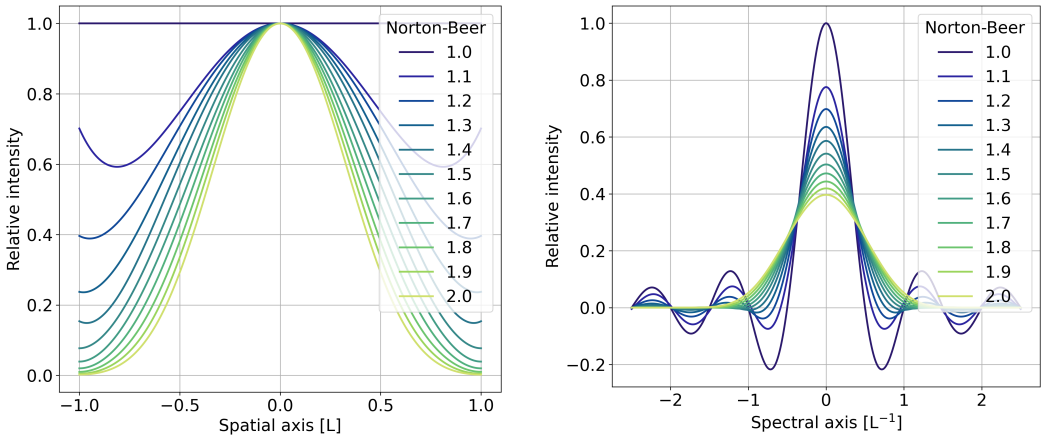

(a) (b)

Figure 3.3: Apodization functions used throughout this work; (a) apodization function in the spatial domain; (b) apodization function in the spectral domain; the labels of the apodization functions are the FWHM relative to the sinc-function.

Beer apodization with 10 functions, where the increase of the FWHM ranges from 10 % to 100 %. Both follow the generic form denote by

$$A_{NB}(x) = \begin{cases} \sum_{k=0}^{K-1} c_k \left[1 - \left(\frac{x}{L}\right)^2\right]^k & \text{if } x \in [-L, L] \\ 0 & \text{else} \end{cases} \tag{3.23}$$

where K is the number of parameters used to shape the apodization window to gain different degrees of apodization strength. The resulting apodization windows using the proposed parameters by Naylor and Tahic (2007) presented in Tab. 7.7 and their Fourier transform are shown in Fig. 3.3 for different FWHM relative to the sinc function. The analytical Fourier transform can be calculated following Ntokas et al. (2023b) and is shown for completeness in Appx. A.7.1.

Subsequently, the results are compared to commonly used apodization functions. Their definitions and references are provided in Tab. 7.8. For this, the $|h/h_{\text{sinc}}|$ and W/W_{sinc} are determined for each apodization window, analyzing varying degrees of apodization strength where possible. The results are presented in Fig. 3.4. Among these apodization functions, the extended Norton-Beer apodization functions, as defined by Naylor and Tahic (2007), closely

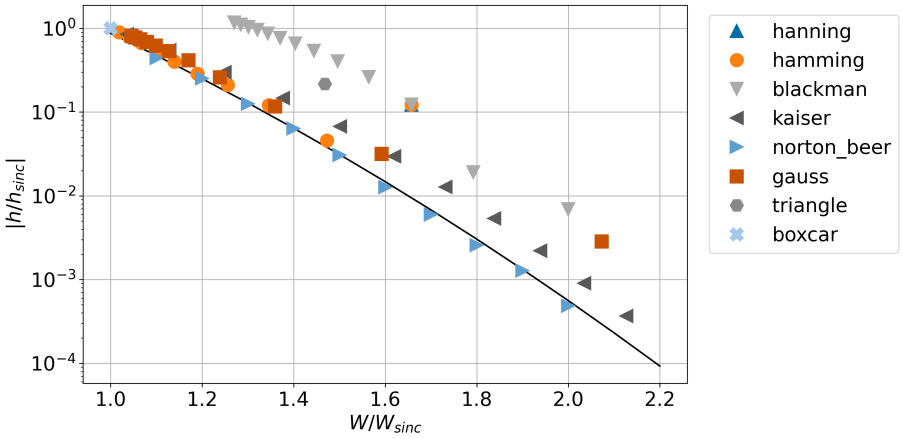

Figure 3.4: Filler's Diagram for commonly used apodization functions with different parameters; the functions and used parameters for each apodization window, including their references, are presented in Tab. 7.8; the parameters in increasing order correspond to the markers from small to large FWHM, except for Hamming and Gauss window, where it corresponds to the markers from large to small FWHM; the solid line represents the boundary defined by the Eq. (3.22).

align with the solid boundary line, defined in Eq. (3.22), delivering the best overall outcome. Because of its optimal properties with respect to these two measures, the Norton-Beer apodization has a large popularity in the Fourier-transform spectroscopy community (Boone et al., 2002; Griffiths and De Haseth, 2007). The Kaiser apodization, shows similar results, but with higher side lobes. This comes from the fact that Norton-Beer apodization functions minimize the side lobes for a fixed FWHM, whereas the Kaiser windows maximize the energy concentration in the main lobe for a fixed maximal side lobe, as discussed by Kaiser and Schafer (1980). The Gauss window follows the Kaiser window, but drifts away for large relative FWHM. The Hamming windows exhibit favorable characteristics as they closely align with the boundary line for smaller relative FWHM values up to 1.5. However, for larger FWHM values, they gradually deviate from the boundary line. The Blackman apodization shows an overall poor performance. The Hanning window can be considered as a special case of the Hamming window, where the parameter is set to 0.5. Similarly, it can also be seen as a special case of the Blackman apodization with the parameter set to 0. However, the Hanning window, like the Blackman window, deviates significantly from the boundary line.

When apodization is applied, the boxcar function is exchanged by the apodization window

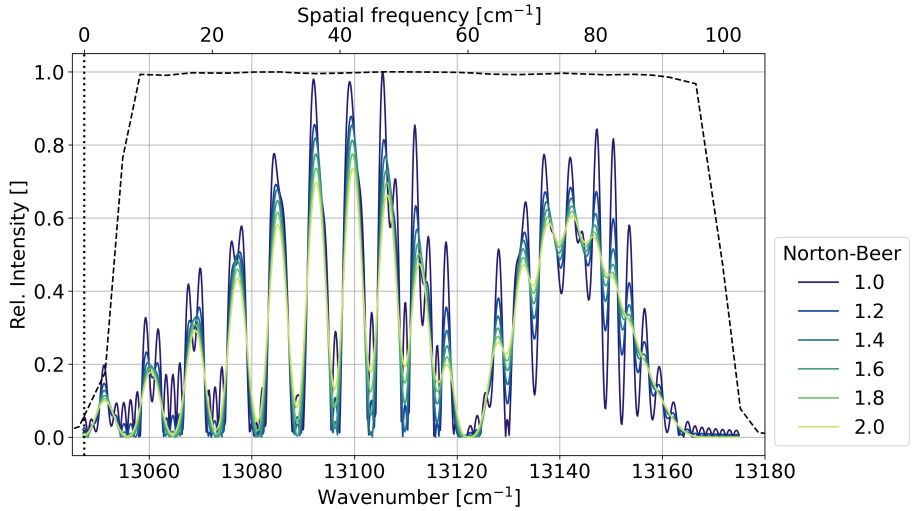

Figure 3.5: Spectra as seen from the AtmoLITE instrument using different Norton-Beer apodization functions defined in Tab. 7.7, where the instrument specifications are taken from Tab. 4.1; the dashed and vertical dotted line indicate the curve of the bandpass filter and the Littrow wavenumber, respectively; the top x-axis shows the spatial frequency at the detector using Eq. (3.3) for the translation.

in Eq. (3.15). The ILS is thus the Fourier transform of the apodization window. The Fourier transform of the apodization function is therefore of large interest as this allows direct calculation in the spectral domain as presented in Sec. 3.2.2, which is used in solving inverse problems during the retrieval in Sec. 3.4.

As an example, the spectra as seen from the AtmoLITE instrument using different Norton-Beer apodization functions are shown in Fig. 3.5, where the specifications are taken from Tab. 4.1. It shows that with increasing strength of the apodization, the spectral oscillations are decreased at the cost of decreased spectral resolution.

3.3 Signal and noise analysis

This section presents the theoretical framework used to calculate the intensity level measured by the detector. It serves to convert the radiance arriving at the instrument into signal intensity as seen in the observations. This information thus is crucial for generating synthetic measurement data. The signal intensity not only determines the measurement data but also plays a vital role in governing the signal-to-noise level and, consequently, the temperature pre-

cision. Following the theory on the noise level, introduced subsequently, both the signal and noise estimations are utilized throughout Chapter 4 to assess the instrument's performance.

To estimate the signal intensity measured by the detector, first the amount of light needs to be determined, which falls into the aperture of the instrument. Hereby, the arriving radiance is multiplied with the etendue, which defines the ability of an optical system to transmit light. The etendue is the multiplication of the area of the aperture and the solid angle of the 2D field of view. As the incident light propagates through the instrument, it first travels through the band pass filter, where the desired spectral region of interest is isolated. The band pass filter has a certain transmission rate, which attenuates the light slightly. Subsequently, it encounters the front optics where each lens's optical surface further attenuate the light by reflecting a small portion of it. After that, the light is split into two wave fronts and directed to the diffraction gratings. The gratings are indicated by a certain grating efficiency for a given wavelength, which attenuates the light further. When the light travels back to the beam splitter, only half of the light is forwarded to the detector. Propagation through the camera optics induces the same attenuation effect due to reflection on the optical surfaces as the front optics. The detector then transfers the photons into a electrical signal, which is governed by the detector efficiency. All these steps form the loss factor or overall efficiency of the instrument. Additionally, it is essential to consider that the intensity is linearly proportional to the integration time. Lastly, to get the estimate per pixel, the incident intensity needs to be divided by the number of used pixels since the etendue refers to the entire field of view. The quantification of these factors can be found in Table 4.1 for the AtmoLITE instrument. Revisiting the interferogram equation in Eq. (3.4), the mean signal is the spectrally integrated radiance. The mean signal of one row can therefore be calculated by

$$R_p(z) = \frac{R(z)\, E\, L\, t_{int}}{N} \tag{3.24}$$

where R is the spectrally integrated radiance within the spectral range of the instrument for a given tangent altitude z, E is the etendue of the instrument, L denotes the loss factor or efficiency of the instrument, t_{int} refers to the integration time and N is the total number

of used pixels of the 2D detector array.

The noise level is determined by the detector specifications. Since the instruments measures emissions in the near infrared, a silicon-based detector can be used. The relatively long integration time permits to neglect readout noise. To maintain a low level of dark current, the detector's temperature is stabilized to cool conditions. As a result, the dominant source of noise is the remaining shot noise. Shot noise is a form of statistical noise that characterizes the probability distribution of the number of photons that reach the detector. It can be modeled by a Poisson process with mean and variance equal to the signal. For a signal above 10 counts, the Poisson distribution approximates a normal distribution about its mean. Thus, for simplicity the shot noise is approximated by an additive white Gaussian noise with standard deviation equal to the square root of the signal in each pixel. The Fourier transform propagates the shot noise equally into the imaginary and real part of the spectrum. However, the retrieval works with the absolute value of the Fourier transform, which rotates the shot noise of the imaginary part into the real part and mirrors the negative values into the positive plane, inducing a bias in the retrieved temperature, especially for low signals. The resulting noise distribution can be described by a Rice distribution (Talukdar and Lawing, 1991), which describes the distance to the origin in a two-dimensional space, where the position is described by two Gaussian variables. In this application, the two random variables are the imaginary and real part of the spectrum and the distance represents the absolute value of the spectrum. Additional information regarding the propagation of noise through the Fourier transform and the spectral noise of a magnitude spectrum can be found in Appx. A.8.

3.4 Temperature retrieval

The temperature retrieval solves an inverse problem, where a forward model is employed to simulate a spectrum. Optimizing the input of the forward model such that the difference between the simulated and the measured spectrum is minimized, gives the retrieved atmospheric parameters.

The forward model used here is based on the radiative transfer model presented in Sec. 2,

but slightly modified. It takes a 1D temperature profile and a 1D number density profile of excited $O_2(b^1\Sigma_g^+)$, referred to as excited O_2 in the following, and calculates the spectra for given tangent altitudes following the radiative transfer equation presented in Sec. 2.3 and in Sec. A.5. It is subsequently convolved with the ILS discussed in Sec. 3.2.2, resulting in an analytical spectrum as seen from the instrument.

It is important to highlight that the O_2 A-band emission lines are very narrow, allowing to approximate them as shifted Dirac delta distributions. When a function is convolved with a Dirac impulse, the result is the same function shifted by an amount equal to the shift of the Dirac impulse. Consequently, instead of convolving the full atmospheric spectrum with an ILS, the ILS can be positioned at the location of the emission line, scaled by the line strength, and then summed up. This approach allows to use a line by line model, where slightly varying ILSs can be employed for multiple emission lines as it will be done for some correction steps presented in Sec. 4.3.4 and Sec. 4.3.5.

The retrieval method, which will be discussed in the upcoming Section 3.4.1, is primarily based on the work of Rodgers (2000). Subsequently, a temperature retrieval of a homogeneous gas cell is described in Sec. 3.4.2. Instead of calculating the full radiative transfer equation, it only calculates the rotational distribution of the emission lines described in Sec. 2.2 and scales them with a scaling factor, which is again convolved with the ILS, resulting in a spectrum as seen from the instrument for the given homogeneous gas cell. This simplified model can be helpful during the assessment of correction methods. It allows to propagate the effect into the temperature retrieval without running through the computationally expensive full retrieval using the radiative transfer equation.

3.4.1 Temperature retrieval using radiative transfer model

Analogous to Rodgers (2000), the temperature retrieval solves the optimization problem given by

$$\min_{\boldsymbol{x}_s} \left(\boldsymbol{y} - F\left(\boldsymbol{x}_s\right)\right)^T \mathbf{S}_\epsilon^{-1} \left(\boldsymbol{y} - F\left(\boldsymbol{x}_s\right)\right) + \left(\boldsymbol{x}_s - \boldsymbol{x}_a\right)^T \mathbf{S}_\mathrm{a}^{-1} \left(\boldsymbol{x}_s - \boldsymbol{x}_a\right) \tag{3.25}$$

where $F : \mathbb{R}^N \mapsto \mathbb{R}^M$ is the forward model taking the vector $\boldsymbol{x}_s \in \mathbb{R}^N$ containing all state parameters consisting of a concatenated 1D temperature and 1D number density profile of excited O_2 molecules, and returning analytical spectra concatenated for all tangent altitudes. The concatenated measured spectra are stored in $\boldsymbol{y} \in \mathbb{R}^M$. $\mathbf{S}_\epsilon^{-1} \in \mathbb{R}^{M\times M}$ is the inverse of the covariance related to the measurement errors, also referred to as measurement error precision matrix. It scales the differences between the measured and simulated spectral samples with the inverse of the measurement uncertainties. A setup strategy of $\mathbf{S}_\epsilon^{-1}$ is outlined in Appx. A.9.1. The second term in Eq. (3.25) consists of the regularization. Hereby, a priori knowledge is incorporated into $\boldsymbol{x}_a$ and the differences between the state parameter and the a priori vector are scaled by the inverse of the associated covariance matrix $\mathbf{S}_\mathrm{a}^{-1} \in \mathbb{R}^{N\times N}$, also referred to as a priori precision matrix. Regularization adds additional terms or constraints to approximate the original, typically ill-posed problem by a similar well posed one. Many ways are proposed how to set up a precision matrix. A popular option due its simplicity is the Tikhonov regularization given by Tikhonov and Arsenin (1977). However, this regularization can be user-unfriendly due to the setting of weighting factors, which lack physical meaning, as discussed in detail in Appx. A.9.2. The auto-regressive approach addresses this problem. It uses a 1D exponential covariance

$$\mathbf{S}_\mathrm{a}(i,j) = \sigma \exp\left(\frac{\mid \boldsymbol{z}_i - \boldsymbol{z}_j \mid}{c}\right) \tag{3.26}$$

with a given standard deviation $\sigma \in \mathbb{R}$ and a correlation length $c \in \mathbb{R}$, where $\boldsymbol{z}$ represents the vertical grid associated with the state parameters and i and j are indices corresponding to different layers. The setup of the inverse of $\mathbf{S}_\mathrm{a}$ is discussed in Appx. A.9.2 which mainly follows the analytical solution presented by Tarantola (2005) and agrees with the discretized matrix presentation of $\mathbf{S}_\mathrm{a}^{-1}$ shown by Rodgers (2000).

Diagnostics

To analyze the retrieval results, Rodgers (2000) proposed linear diagnostics, which allows to asses the quality of the reconstruction. This section provides a concise overview of these

diagnostic tools. The two key metrics are the gain and the averaging kernel matrix. The gain matrix, denoted by $\mathbf{G} \in \mathbb{R}^{N\times M}$, maps differences in the measurement to the retrieval result and thus is a measure to assess the response of the retrieval to perturbations in the measurements. It is defined by

$$\mathbf{G} = \left(\mathbf{S}_{\mathrm{a}}^{-1} + \mathbf{F}'(\boldsymbol{x}_f)^T \mathbf{S}_{\varepsilon}^{-1} \mathbf{F}'(\boldsymbol{x}_f)\right)^{-1} \mathbf{F}'(\boldsymbol{x}_f)^T \mathbf{S}_{\varepsilon}^{-1}, \tag{3.27}$$

where $\boldsymbol{x}_f$ is the retrieval result and $\mathbf{F}'$ the Jacobian of the forward model, approximated by finite differences. The averaging kernel matrix, denoted by $\mathbf{A} \in \mathbb{R}^{N\times N}$ links the true atmospheric state to the retrieval result and is defined by

$$\mathbf{A} = \mathbf{G}\mathbf{F}'(\boldsymbol{x}_f). \tag{3.28}$$

If the gain matrix is the inverse of the Jacobian, the averaging kernel matrix will take the form of an identity matrix. This indicates that the retrieved outcome aligns precisely with the actual atmospheric state, representing an ideal retrieval process. Nevertheless, the regularization term and the potential rank deficiency of the Jacobian matrix may hinder the gain matrix from being a true inverse. In well-regularized retrievals, efforts are directed towards closely approximating the inverse to attain an averaging kernel that closely resembles the identity matrix.

The measurement contribution incorporates this intention and shows whether the information of the reconstructed parameters come from the actual measurement or from the a priori state. It is defined by

$$\boldsymbol{x}_f = \mathbf{A}\boldsymbol{x}_t + (\mathbf{I_N} - \mathbf{A})\boldsymbol{x}_a + \mathbf{G}\boldsymbol{\varepsilon}, \tag{3.29}$$

where $\boldsymbol{x}_t$ is the true atmospheric state and $\mathbf{I_N} \in \mathbb{R}^{N\times N}$ is an identity matrix. The first and second term determines the contribution by the actual measurement and by the a priori knowledge, respectively. The third term propagates the measurement uncertainties into the retrieval result. The objective is to maximize the magnitude of the first term while minimizing the values of the two other terms towards zero. If the averaging kernel is an identity matrix, the second term is zero and assuming that the noise term is small, the retrieval result is close

to the true atmospheric state. It is important to ensure that the eigenvalues of matrix $\mathbf{G}$ are small in order to mitigate the amplification of noise during the retrieval process.

Furthermore, the sources of information for a specific retrieved state parameter can be determined by examining the associated rows of the averaging kernel. One metric is known as the measurement contribution, which is defined as the sum of a row. If the measurement contribution is equal 1 and assuming that $\boldsymbol{x}_a$ is constant for all state parameters, the second term in Eq. (3.29) will be equal to zero entailing that all the information comes from the actual measurements. In most applications however $\boldsymbol{x}_a$ is not constant but represent a profile of an atmospheric parameter. If however the kernel of one row is narrow and if $\boldsymbol{x}_a$ is varying slowly, the second term will be desirably close to zero. This introduces another metric referred to as resolution, which quantifies the amount of smoothing introduced in the retrieval process. The regularization can cause a connectivity between the layers (e.g. the standard deviation and correlation length in the auto-regressive approach determines the strength and extend of the inter-connectivity), which is incorporated into the gain and therefore also into the averaging kernel matrix. The resolution is often measured by the FWHM of averaging kernel row. A large FWHM means that the information of a retrieved state parameter comes from multiple atmospheric layers. A narrow FWHM means that only a few true state parameters are responsible for the retrieved parameter, which is desirable.

Revisiting the third term of Eq. (3.29), the retrieval noise is determined by the effect of perturbations in the measurement propagated into the retrieval result. The covariance of the retrieval noise therefore can be defined as

$$\mathbf{S}_{\text{noise}} = \mathbf{G}\mathbf{S}_{\varepsilon}\mathbf{G}^{T}, \tag{3.30}$$

where $\mathbf{S}_{\text{noise}} \in \mathbb{R}^{N\times N}$. The standard deviation of each parameter is given by the square root of the diagonal entries.

3.4.2 Temperature retrieval of a homogeneous gas cell

This section minimizes a simplified cost function given by

$$\min_{c,T} \|\boldsymbol{y} - F(c,T)\|_2^2 \tag{3.31}$$

where the forward model F is only dependent on a single temperature T and a scalar c. This temperature parameter defines the relative rotational distribution of the emission lines using Eq. (2.12), which are subsequently convolved with the ILS. As last step, the simulated spectrum is multiplied by the scalar c to fit the magnitude of the measured spectrum given by $\boldsymbol{y}$. Each row is thus optimized individually. This method directly propagates spatial or spectral errors into the retrieved temperature, as if the instrument would observe a homogeneous gas cell. This method is therefore particularly useful for assessing instrument errors and errors introduced by data processing, which will be extensively discussed in Sec. 4.3 when evaluating the performance of instrument calibration. It is important to note, however, that if this simplified model is used, the retrieved profile may lack smoothness due to high sensitivity to noise and the absence of smoothing effects introduced by regularization. Therefore, it is recommended to employ this simplified model solely for detailed assessment of instrumental error and processing procedures.

3.5 Chapter summary

This chapter provides an introduction to the observational method used for temperature observation in the mesosphere and lower thermosphere (MLT) measuring the oxygen A-band emission by a spatial heterodyne interferometer (SHI). The general concept of a SHI is presented as a component of Fourier transform spectroscopy (FTS). The fundamentals of FTS are covered, including Fourier transformation, the concept of instrument line shape (ILS) due to a finite detector dimensions, sampling theory resulting from pixel sampling, and the concept of apodization, which reduces oscillations caused by the general ILS.

The conversion process from atmospheric radiance at the aperture to flux falling onto the detector is presented, and the mathematical derivation of the expected noise level of the detector is provided. This noise is introduced by the detector into the interferogram in the spatial domain. Subsequently, the spatial noise is analytically propagated into the spectral

domain by the Fourier transformation. The analytical solution for the expected mean of absolute spectra including noise is also discussed, highlighting its adherence to a Rice distribution, which deviates from the Gaussian distribution and should be considered when dealing with low signals.

In the final part of this chapter, an overview of the temperature retrieval process is provided, involving two distinct retrieval methods. The first method, known as the usual retrieval, is based on the radiative transfer principles discussed in Chapter 2. It encompasses a discussion on regularization and defines retrieval diagnostics. The second method is a simplified retrieval process that allows for the direct propagation of any effects in the interferogram or spectrum into the temperature retrieval. This simplified retrieval focuses solely on retrieving the temperature of a homogeneous gas cell, which is repeated row-wise without solving a 1D atmospheric structure, as is done in the usual retrieval process. It should be noted that this second retrieval method is specifically used to assess instrument errors and errors introduced by data processing.

Chapter 4

Assessment of the instrument's performance

This chapter aims to evaluate the performance of the current instrument version, AtmoLITE. The assessment process unfolds in several steps.

Firstly, Section 4.1 presents the results of simulations that model the expected radiance reaching the instrument aperture under various atmospheric conditions. These simulation outcomes serve as input for the performance assessment in Sec. 4.2. Special attention is dedicated to self-absorption, and these simulations are validated by comparing them with satellite observations.

Secondly, the performance of an ideal instrument is investigated in Sec. 4.2 based on the signal strength derived from the forward simulations shown in Sec. 4.1. These results represents the best-case performance of the instrument, if the calibration is performed perfectly and all errors of the instrument are understood and corrected.

Next, in Sec. 4.3, the current state of the processing chain is presented, which includes the correction methods developed during this thesis of currently known instrument errors. Each processing step is carefully presented, along with the mathematical description of the instrumental error and the necessary tools for correction. These correction methods are assessed using on-ground calibration data from the INSPIRESat4 mission and employing data perturbation to evaluate their sensitivity in terms of the retrieved temperature, where the sim-

Table 4.1: Summary of the AtmoLITE instrument specification according to design; the loss factor of the instrument is calculated following the description in Sec. 3.3.

Parameter	Property
Littrow wavenumber	$13\,047\,\mathrm{cm}^{-1}$
Littrow angle	6.6°
Magnification factor of camera optics	0.58
Groove density of gratings	$300\,\mathrm{mm}^{-1}$
Spectral range in wavelength	765.76 nm to 759.53 nm
Spectral range in wavenumber	$13\,059\,\mathrm{cm}^{-1}$ to $13\,166\,\mathrm{cm}^{-1}$
Spectral range in spatial frequency	$8.8\,\mathrm{cm}^{-1}$ to $95.5\,\mathrm{cm}^{-1}$
Field of view	$1.3\,\mathrm{deg}^2$
	($\approx 60\,\mathrm{km}^2$ for orbit altitude of 600 km)
Aperture radius	37.5 mm
Etendue	$0.018\,\mathrm{cm}^2\mathrm{sr}$
Grating efficiency	0.8 at 762 nm
Detector	GSENSE400BSI
Detector number range	$0 - 4095$ (12bit)
Detector columns/rows	2 000/2 000
Detector region of interest columns/rows	860/860
Pixel pitch	11 µm
Quantum efficiency	0.7 at 762 nm
Number of lenses	7
Reflection by optical surface	0.5 %
Filter transmission	97 %
Loss factor of instrument	25.6 %

plified retrieval method outlined in Sec. 3.4.2 is employed. This step-by-step analysis allows to identify critical stages in the processing chain essential for obtaining accurate temperature data.

The assessment is finalized by an end-to-end simulation in Sec. 4.4, where monochromatic measurements from the calibration data of the INSPIRESat4 mission are used to simulate an interferogram, allowing for an assessment based on measured on-ground data. This simulation gives an error estimate of the overall performance of the instrument at the calibration stage.

The specifications of the AtmoLITE instrument are given in Tab. 4.1. These specification

are used for all simulations and data analysis of the calibration data of the INSPIRESat4 mission throughout Chap. 4 and 5.

4.1 Forward simulation

The temperature precision is predominantly defined by the instrument's noise level, which, in turn, relies on the signal strength, as discussed in Sec. 3.3. The following sections therefore explore the generation of synthetic O_2 A-band emissions to evaluate the signal level arriving at the instrument's aperture. It is mainly based on the theory introduced in Sec. 2.1–2.3.

The generation of synthetic emissions is built upon the HAMMONIA model data, which is introduced here in Sec. 4.1.1. The data provides temperature and the number densities of the required constituents involved in the photo-chemical processes discussed in Sec. 2.1. The simulation results are discussed in Sec. 4.1.2 and subsequently compared to the satellite data in Sec. 4.1.3 as validation.

4.1.1 Test data set extracted from HAMMONIA

The Hamburg Model for the Neutral and Ionized Atmosphere (HAMMONIA) run, as presented by Schmidt et al. (2006), models atmospheric dynamics, radiation and chemistry from earth's surface up to 250 km with vertical resolution of 2 km to 3 km. It is based on the atmospheric general circulation model ECHAM developed at Max Planck Institute for Meteorology in Hamburg, Germany, and was extended by important radiative and dynamical processes of upper atmosphere coupled to a chemistry module. Simulation runs for solar maximum and minimum conditions are performed, as the flux of solar photons in the atmosphere depends on the solar cycle. Local time variability is considered by modeling a local time snapshot. It provides monthly averaged 3-D data sets for temperature and the volume mixing ratios of the required species involved in the photo-chemical processes discussed in Sec. 2.1. Test data sets are generated to be used in the following, covering an equidistant longitude and latitude grid of 10°, up to 180 km. At each longitude and latitude point the solar zenith angle (SZA) is calculated in accordance with the local time of the HAMMONIA runs. This is done for each

month and for solar minimum and maximum conditions. If a fine vertical discretization is needed (e.g. in Sec. A.6.1), the temperature is interpolated linearly and the number densities of all required compounds are interpolated exponentially.

4.1.2 Results of oxygen A-band emission simulations

In this section, the results of the O_2 A-band emission simulations are presented. The test data set extracted from the HAMMONIA model run, as discussed in Sec.4.1.1, serves as input for calculating the number density of excited O_2 molecules using Eq. (2.1), which initiates the emission process. The radiative transfer equation presented in Eq. (2.13) is employed to propagate the emission along the LOS, where self-absorption is considered.

The input temperature profiles differ for solar minimum and maximum conditions above 120km (Figure 4.1a). Figure 4.1b illustrates the mean and standard deviation of the expected number density of excited O_2 molecules resulting from different production mechanisms, based on the temperature profiles. The total excited O_2 represents daytime conditions, while the Barth process corresponds to nighttime conditions. The number density of excited O_2 during nighttime is approximately one order of magnitude lower compared to that during daytime conditions. Propagating this information through the radiative transfer model estimates the radiance at the instrument for various tangent altitudes, as depicted in Fig.4.1c. Daytime simulations show greater variability at higher tangent altitudes above 90 km, primarily due to variations in photolysis production mechanisms illustrated in Figure4.1b, mainly caused by varying SZA.

It's noteworthy that during daytime, the arriving signal at the instrument is further reduced for tangent altitudes below 80 km, as depicted in Fig. 4.1c, even though the number density of excited O_2 increases, as displayed in Fig. 4.1b. This decline can be mainly attributed to the influence of self-absorption. Analyzing the normalized radiance distribution along the LOS in Fig. 4.2a reveals that, for tangent altitudes below 80 km, an increasingly smaller portion of radiance originates from layers situated below 80 km. This effect is also present in Fig. 4.2b, which examines the transmittance from the tangent layer evaluated at the peak of each emission across different tangent altitudes. For a tangent altitude of 85 km, the transmit-

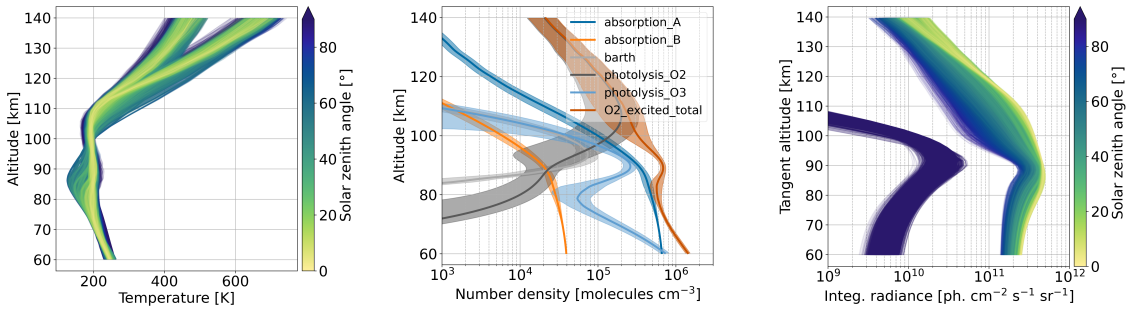

(a) (b) (c)

Figure 4.1: (a) 1-D input temperature profiles used in the forward calculation; (b) Number density of excited O_2 molecules attributed to five distinct production mechanisms during daytime conditions; the total excited O_2 represents the sum of the five parts; the Barth process is the only active process during nighttime conditions; (c) Estimated radiance reaching the instrument for various tangent altitudes for day- and nighttime conditions, which correspond to SZA below and above 90°, respectively.

tance is at 70 % for the emission lines situated at the center of the O_2 A-band, and nearly all emission lines become optically thick for tangent altitudes below 70 km. In summary, the decline in signal between 90 km and 80 km is attributable to both the diminishing production of excited O_2 and the decreasing transmittance. For tangent altitudes below 80 km, the impact of strong self-absorption is evident, leading to minimal information originating from the tangent layer. It is recommended to consider self-absorption for tangent altitudes below 85 km. This phenomenon inherently limits the information content that can be derived from temperature data obtained from measurements in this region. The reduction in signal at higher altitudes, above 120 km for daytime conditions, constrains the measurement method from the uppermost regions.

4.1.3 Comparison with satellite data

In this section, the forward simulations presented in Fig. 4.1c are validated by comparing them with data from the Optical Spectrograph and InfraRed Imaging System (OSIRIS) and SCanning Imaging Absorption spectroMeter for Atmospheric CartograpHY (SCIAMACHY). It is important to note that this comparison is intended to provide a preliminary assessment of the radiative transfer model's capability to estimate signal strength, which is crucial for

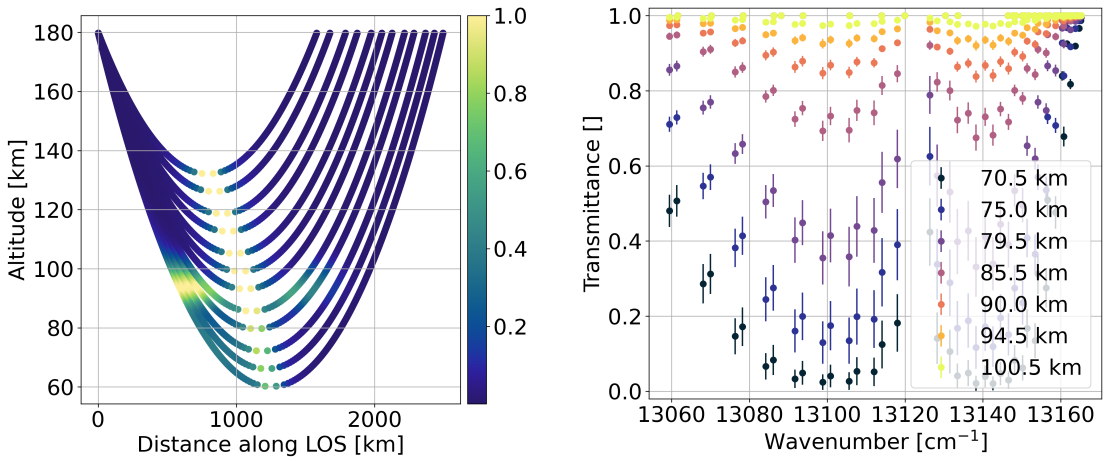

(a) (b)

Figure 4.2: (a) Normalized radiance distribution along the LOSs; (b) Transmittance from the tangent layer evaluated at the peak of each emission line for different tangent altitudes, shown for multiple LOSs which tangent altitudes are given in the legend; error bars exhibit the standard deviation over all months and solar maximum and minimum conditions.

temperature precision assessment. A precise forward calculation is not necessary for the retrieval process since the number densities of excited O_2 are retrieval parameters, as discussed in Section 3.4.1.

OSIRIS aboard the satellite ODIN has been in operation since 2001, circling the Earth on a sun-synchronous orbit (Llewellyn et al., 2004; McLinden et al., 2012). It is a spectrograph measuring a spectral range of 274 nm to 810 nm with a spectral resolution of approximately 1 nm. OSIRIS scans tangent altitudes between 10 km and 110 km with vertical resolution of 2 km above 50 km. Due to the lack of nighttime observations by OSIRIS, data from the SCIAMACHY instrument aboard ENVISAT are used. SCIAMACHY was firstly proposed by Burrows et al. (1995). The instrument was in operation from March 2002 till April 2012, during which nadir, limb, solar and lunar occultation measurements were performed. The mesospheric limb scans span approximately 75 km to 150 km with a vertical resolution of 3 km. The level1 data is extracted from channel 4 (595 nm to 812 nm) and the software SciaL1C is used to derive calibrated spectra.

For the comparison, 3 223 and 3 654 vertical scans from January 2003 are selected from OSIRIS and SCIAMACHY, respectively. These observations are compared with forward sim-

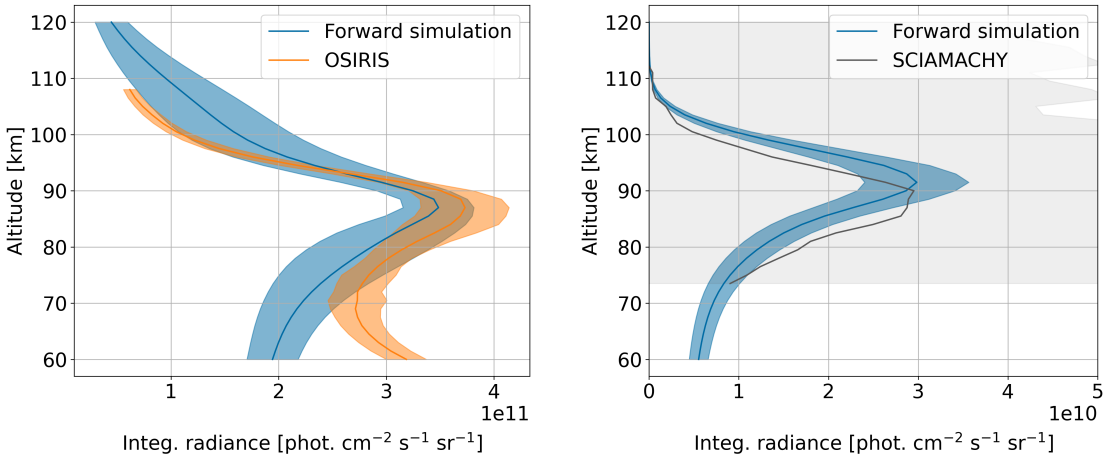

(a) (b)

Figure 4.3: Comparison of spectrally integrated limb radiance profiles, as observed by a satellite instrument and compared to the forward simulation results detailed in Section 4.1.2; mean and standard deviation of the respective profiles are presented a solid line and shaded area, respectively; (a) comparison between OSIRIS measurements and forward simulations during daytime conditions for SZA ranging from 60° to 80°; (b) comparison between SCIAMACHY measurements and forward simulations during nighttime conditions for SZA ranging from 120° to 145°

ulations based on HAMMONIA for the same month, focusing on a spectral region of interest between 759.5 nm to 765.8 nm for all three datasets. The results are presented in Figure 4.3, with the SZA matched to the available satellite observations. The forward simulations conducted under daytime conditions, as shown in Fig. 4.3a, demonstrate a satisfactory overall agreement with the observations by OSIRIS. There is an increase in radiance towards to lower tangent altitudes for OSIRIS observations, possibly attributed to upwelling stray light. The nighttime simulations, presented in Fig. 4.3b, agree well with the SCIAMACHY observations in terms of the magnitude of the integrated radiance. However, the standard deviation of the SCIAMACHY observations is notably large, possibly related to calibration processes in the software SciaL1C. Further investigation of this issue is beyond the scope of this comparison. Notably, there is an apparent altitude shift in the intensity peak. The simulated radiance reaches its peak intensity at 92 km, consistent with the simulations presented by Chen (2020) and Song et al. (2018), as well as the rocket measurements discussed in Murtagh et al. (1990). However, the observations from SCIAMACHY indicate the highest intensities

at 89 km. Yankovsky and Vorobeva (2020) argues that the Barth process is very variable with respect to atomic oxygen as it scales with the square its number density, as also presented in Eq. (2.9). When comparing the altitude distribution of atomic oxygen in the utilized test data set extracted from HAMMONIA runs, which peaks at 98 km, with the retrieved number density of atomic oxygen from SCIAMACHY data performed by Zhu and Kaufmann (2019), which peaks at 94 km, the altitude shift becomes plausible.

In summary, the comparison demonstrates that the signal strength derived from the forward model simulations based on climatological values are consistent with respective observations by OSIRIS and SCIAMACHY. These forward simulations therefore will allow a realistic performance assessment of the AtmoLITE instrument, as discussed in Section 4.2.

4.2 Performance of an ideal instrument

This section evaluates the expected performance of an ideal instrument without any instrument errors, where the statistical shot noise induced by the detector is the limiting factor. Hereby, the temperature precision of the observational method is analyzed regarding a homogeneous gas cell, for different temperature levels and signal strengths. These results are then used to give an estimate of the temperature precision dependent on tangent altitude, where the upper resolvable altitude limit is determined for day- and nighttime conditions. This is a reiteration of the results presented by Ntokas et al. (2023a), which are concluded with a full end-to-end simulation, where interferograms are simulated based on the radiative transfer model presented in Sec. 4.1 and temperature retrievals are performed where the forward model incorporates the radiative transfer equation as introduced in Sec. 3.4.1.

To illustrate the temperature dependency of the measurements, synthetic interferograms and spectra are shown for various temperatures in Fig. 4.4. The spectra in Fig. 4.4b are essentially the rotational distribution of the O_2 A-band emissions from Fig. 2.2 convolved with the instrument line shape (ILS) determined by the Norton-Beer strong apodization. As already mentioned in the discussion of Fig. 2.2, the lower sensitivity of the emissions at higher temperature is also visible in the spectrum as presented by the gradients in Fig. 4.4b. The

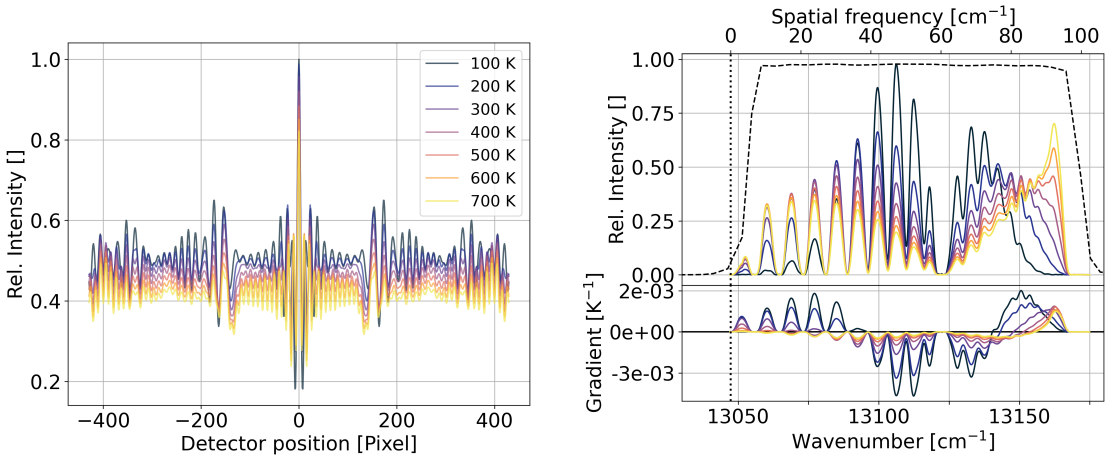

(a) (b)

Figure 4.4: (a) interferograms and (b) spectra for various temperatures; in (b) the dashed and vertical dotted line indicate the theoretical curve of the bandpass filter and the Littrow wavenumber, respectively; the top x-axis shows the spatial frequency at the detector; the gradient is calculated by finite difference along the temperature axis.

increase of intensity at 13 165 cm^{-1} is due to the high density of emission lines in this spectral region. The integrated intensity of the emissions within the band pass filter decreases, as the distribution becomes flatter and more intensity lying outside the band pass filter. This effect is also seen in the interferogram, where the peak at the center and the mean value is decreased in Fig. 4.4a.

Next, the temperature bias and the precision of a homogeneous gas cell for different temperatures and signal levels are analyzed. Hereby, noisy interferograms are generated following Eq. (3.4) for a given temperature and mean signal level, where the latter governs the noise level as shown in Sec. 3.3. The non-modulated part is subtracted. Subsequently, Norton-Beer strong (1.6) apodization and subsequent Fourier transformation are applied. The retrieval method for a homogeneous gas cell presented in Sec. 3.4.2 is applied to the spectra, gaining the retrieved temperatures.

Hereby, a Monte-Carlo simulation with 1 000 samples is performed for each signal level and temperature. Since the noise is the square root of the signal as presented in Sec. 3.3, the signal-to-noise ratio (SNR) is the square root of the interferogram's mean. Figure 4.5 shows the bias and the standard deviation of the retrieved temperatures obtained in the

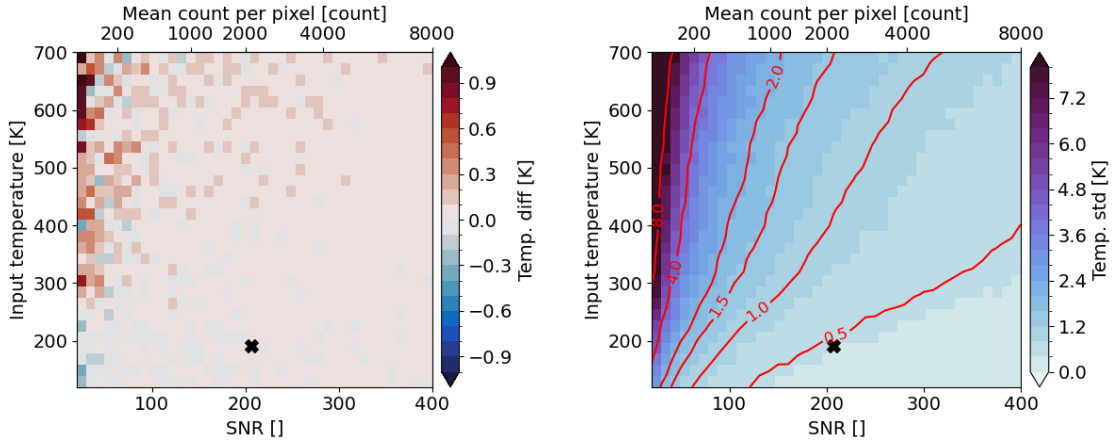

(a) (b)

Figure 4.5: Results of the Monte-Carlo simulations with 1 000 samples for different SNRs and temperatures; (a) mean temperature differences; (b) standard deviation of the retrieved temperatures; contour lines are calculated on smoothed data; the marker indicate the mean expected SNR and temperature of the daytime simulations in the mesopause region at 90 km altitude.

Monte-Carlo simulations. The top axis shows the mean signal assuming that 20 rows are accumulated, referred to as vertical binning, which increases the SNR by a factor of $\sqrt{20}$. Note that a binning of 20 is equivalent to a vertical resolution of 1.5 km, and this binning will be employed in the standard data processing. Further details related to this aspect can be found in Section 4.3. The lower sensitivity of the O_2 A-band emission at higher temperatures is also visible in the temperature precision displayed in Fig. 4.5b. The bias for low signals in Figure 4.5a is caused by using absolute spectra. When taking the absolute value of the spectrum, the spectral noise follows a Rice distribution (Talukdar and Lawing, 1991) which deviates from the normal distribution for spectral values close to zero. Therefore, low signals are affected more. More details on the spectral noise of a magnitudinal spectrum is given in Sec. 3.3 and Appx. A.8.

Subsequently, the estimated counts per pixel are calculated (as shown in Fig. 4.6a) based on the arriving radiance at the instrument's aperture for different tangent altitudes shown in Fig. 4.1c, where Eq. (3.24) is used for the conversion. Hereby, the integration time is set to 1 s and 10 s for day- and nighttime simulations, respectively, and a binning of 20 rows is assumed.

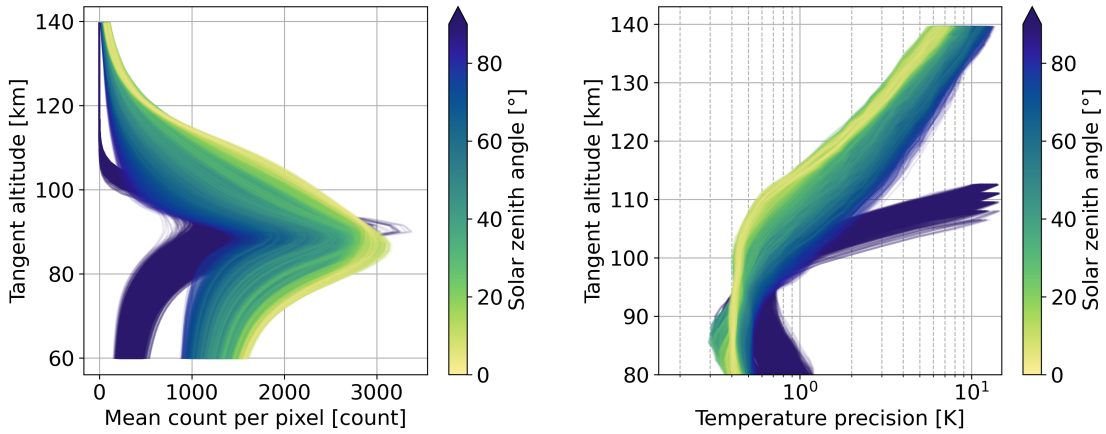

(a) (b)

Figure 4.6: (a) Estimated signal (count per pixel) received at the detector, considering the etendue and optical performance of the instrument; SZA above 90° refer to nighttime simulations; the integration time is set to 1 s and 10 s for day- and nighttime simulations, respectively. (b) Temperature precision calculated from the expected signal from (a) and the temperatures from 4.1a where the interpolated temperature precision field presented in Figure 4.5b is used, assuming a binning of 20 rows; note that signal counts below 100 counts are not considered which cuts off the nighttime simulations around 110 km.

To give a temperature precision estimate of a homogeneous gas cell for each altitude, the interpolated temperature precision field presented in Figure 4.5b is evaluated for the expected signal levels from Fig. 4.6a and for the input temperature profiles from Fig. 4.1a. The results are shown in Fig. 4.6b. The nighttime simulations give a temperature precision below 1 K for tangent altitudes between 85 km and 100 km. For the daytime simulations, a temperature precision of around 0.5 K can be achieved in the strong signal layer between 85 km and 100 km. The temperature precision then decreases for higher tangent altitudes due to the decrease in signal strength and higher temperatures.

In the next step, the upper altitude limit of the observational method is investigated. This is done by determining the required number of binning rows to achieve a certain temperature precision. Hereby, a contour line is extracted from the temperature precision field in Figure 4.5b, which defines the required signal for the temperatures presented in Figure 4.1a. The required signal then determines the required binning using the expected signal in Figure 4.6a. The results for different temperature precision levels are shown in Figure 4.7. During

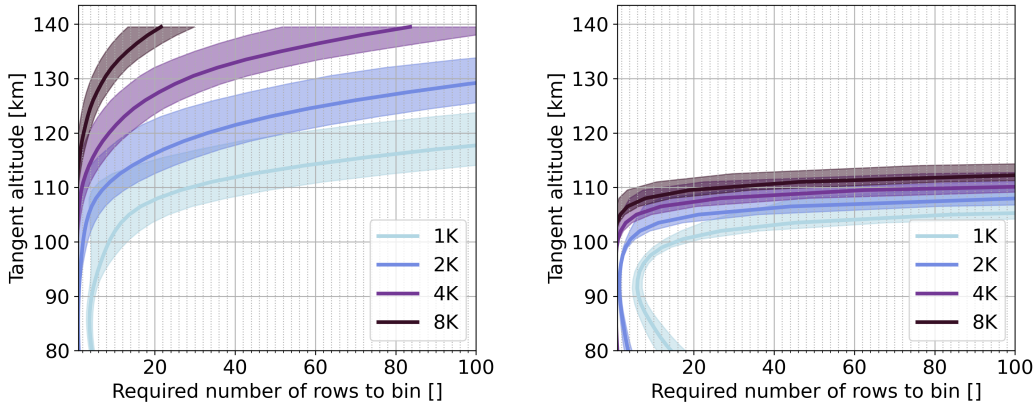

(a) (b)

Figure 4.7: Required binning of rows to achieve a certain temperature precision (a) during daytime and (b) during nighttime; the solid line shows the mean and the shaded area the standard deviation of all used samples from Figure 4.6a.

the daytime the ideal instrument can resolve the higher altitudes on average up to approximately 105 km, 115 km, 125 km and 140 km with a temperature precision of 1 K, 2 K, 4 K and 8 K, respectively, when a binning of 20 rows is applied. During nighttime simulations, accepting lower temperature precision does not help to resolve higher altitudes because the signal decreases strongly above 100 km, as shown in Fig. 4.6a. In general, larger binning can be applied to get more accurate results at the cost of spatial resolution along the vertical axis. For example Fig. 4.7a demonstrates that a temperature uncertainty of 4 K at a tangent altitude 120 km can be achieved with a binning of 8. To achieve a temperature uncertainty of 2 K at a same tangent altitude, a binning of 32 is required. Following this approach for different temperature uncertainties and tangent altitudes, it can be concluded that a fourfold increase in binning, which is equivalent to a reduction in spatial resolution by a factor of four, roughly results in a twofold increase in temperature precision.

Lastly, an end-to-end simulation is conducted, utilizing the temperature retrieval method that incorporates the radiative transfer model including self-absorption, as detailed in Sec. 3.4.1. Hereby, a Monte-Carlo simulation with 100 samples is performed, where different altitude regions for the daytime simulations are tested based on one sample extracted from the test data set presented in Sec. 4.1.1. The selected sample has medium signal strength

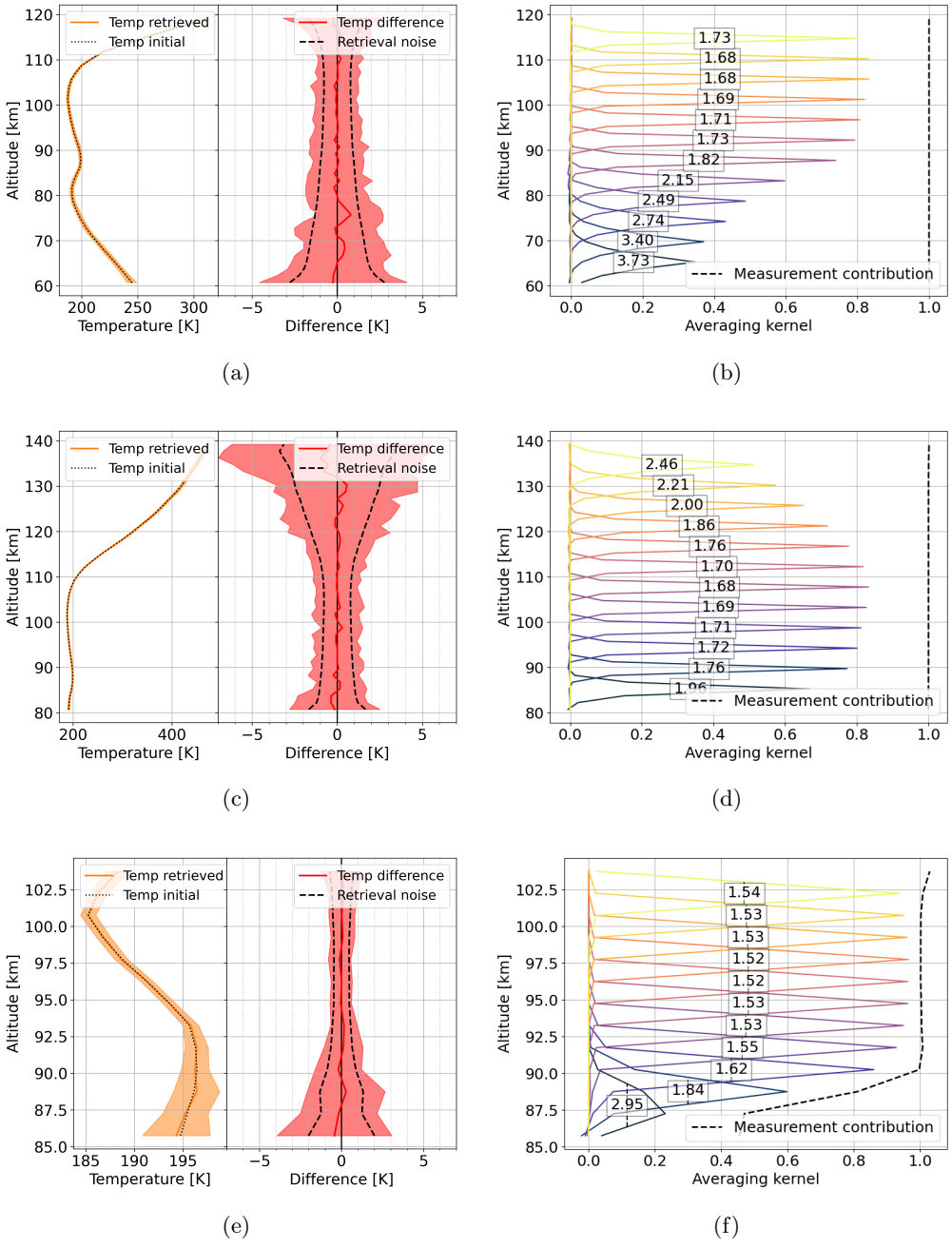

Figure 4.8: Retrieval results of end-to-end simulation using radiative transfer model from Sec. 3.4.1; the daytime simulations assume an integration time of 1 s and an altitude range of (a) 60 km to 120 km and (c) 80 km to 140 km; the nighttime simulations assume an integration time of 10 s and an altitude range of (e) 85 km to 105 km; the solid line and shaded area represent the mean and standard deviation of the 100 Monte-Carlo samples, respectively; the retrieval noise is extracted from the retrieval matrix defined in Eq. (3.30); (b), (d) and (f) averaging kernel including vertical resolution and measurement contribution for the corresponding temperature retrievals in (a),(d) and (e), respectively; note that for the daytime simulations only every 3th averaging kernel row is shown.

and thus shows an average noise level. An integration time of 1 s is assumed for the daytime simulations. The results are presented in Fig. 4.8.

When targeting an altitude range of 60 km to 120 km as presented in Fig. 4.8a, the highest temperature precision of 1 K to 1.5 K is observed at tangent altitudes between 85 km and 115 km. At tangent altitudes below 85 km, the impact of self-absorption becomes apparent, as illustrated in Fig. 4.2. This phenomenon progressively impacts temperature precision more significantly, reaching values as low as 4 K to 5 K for tangent altitude at 60 km. Also, the averaging kernel rows in Fig. 4.8b show that at lower tangent altitudes below 85 km the vertical resolution decreases due to the increasing effect of self-absorption. For tangent altitudes above 115 km, the temperature precision decreases gradually due to the decrease in signal strength as already shown in Fig. 4.6b. The retrieval noise extracted from the retrieval noise matrix defined in Eq. (3.30), displays a similar variation across the altitude range as the temperature precision derived from the Monte-Carlo simulation. However, it consistently underestimates the temperature precision by about 40 %. This discrepancy might arise from the linear assumption of diagnostic metrics, as discussed in Sec. 3.4.1, or from the Gaussian assumption for noise description, despite slight deviations in magnitudinal spectra, as elaborated in Sec. 3.3 and Appx. A.8. Consequently, while the retrieval noise derived from diagnostics serves as an initial approximation, it is important to consider the associated underestimation.

A second simulation with the same parameters is performed where the observed region is shifted upward by 20 km, covering an altitude range of 80 km to 140 km. The results are displayed in Fig. 4.8c. It shows a similar result as the previous simulation for the tangent altitudes between 80 km and 120 km. For higher tangent altitudes, the temperature uncertainty increases up to 6 K for tangent altitude at 140 km due to the decreasing signal strength, agreeing with the results in Fig. 4.6b. The averaging kernels show also a slight decrease in vertical resolution for higher tangent altitudes above 110 km in Fig. 4.8d. The overall temperature precision thus, adheres an hourglass shape with the thinnest point and thus the best temperature precision for tangent altitude at 100 km. To get the overall best temperature precision, the observed field of view thus should be centered at that tangent altitude, covering 70 km to 130 km.

For the nighttime conditions assuming an integration time of 10 s, the altitude region covers 85 km to 105 km. Tests with extended altitude range did not succeed due to the decreasing number density of excited O_2 molecules presented in Fig. 4.1b. The altitudes above 93 km can be retrieved with an high accuracy of around 1 K. Below that decreasing signal strength decreases the temperature precision down to 3 K to 4 K at 85 km. The averaging kernel rows in Fig. 4.8f reveal a similar result where the vertical resolution increases and the measurement contribution decreases for tangent altitudes below 90 km. It should be noted that the precision can be increased by either more vertical binning at a cost of vertical resolution, or by increased integration time or averaging multiple consecutive measurements at a cost of along-track sampling.

This section demonstrated that the current instrument design holds the potential to derive temperatures around the mesopause region with a precision of 1 K to 1.5 K, provided that all error sources are effectively compensated for. Consequently, the following section delves into the discussion of errors stemming from an imperfect instrument and their impact on the retrieved temperature data. Additionally, it explores strategies for mitigating these errors through on-ground calibration methods.

4.3 Assessment and correction of instrument errors

Figure 4.9 presents an outline of how the correction methods are integrated into the processing sequence. Only minimal processing is planned to be performed onboard the satellite platform. The primary onboard processing task involves a vertical binning of 20 rows by calculating the mean across these rows. It should be noted that both methods, accumulating and averaging 20 rows, increase the SNR by a factor of $\sqrt{20}$. Nevertheless, the detector is prone to exhibit failing pixels. This is a common artifact of detectors, which needs to be corrected, before binning. Otherwise, the false value of the bad pixel is incorporated into the mean value and can not be corrected thereafter. This step is further discussed in Sec. 4.3.1. After the downlink, the on-ground processing is typically divided into three steps. The L0-processing links the data to its geolocation and corrects errors in the interferogram space. This yields a corrected

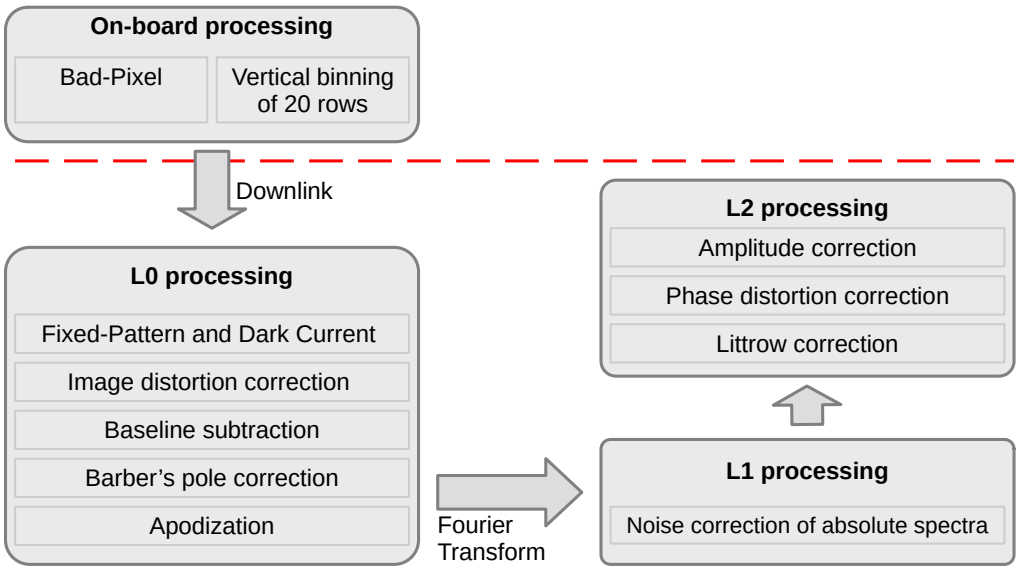

Figure 4.9: Overview of the processing chain

interferogram with corresponding metadata. In the L1-processing, a Fourier transformation is performed along the horizontal axis, converting row-wise the interferogram into a spectrum. After correction of all errors in the spectral domain, the outcome is a corrected spectrum that serves as the input for the retrieval. The L2-processing then mainly contains the temperature retrieval. Errors that are dependent on both spectral and spatial domains are indirectly corrected within the ILS and therefore, included in the forward model. It is worth noting that if an error is dependent on both spectral and spatial variables, yet remains independent in both, the error can be separated into spatial and spectral components and treated separately during L0- and L1-processing.

In the subsequent subsections, each currently identified error is outlined, along with its corresponding correction method developed during this thesis. Both the influence of the error and the efficacy of the correction approach are evaluated through temperature retrieval simulations. In Section 4.3.1, detector specific errors are reviewed including bad pixel, fixed pattern and dark current correction. Following this, the topics of image distortion and Barber's pole intensity variation are addressed in Sec. 4.3.2 and Sec. 4.3.3, respectively. Section 4.3.4 delves into discussions on intensity and contrast variation, succeeded by an exploration of phase distortion and Littrow calibration in Sec. 4.3.5 and Sec. 4.3.6, respectively. For insights into

apodization and Fourier transform, as well as noise correction arising from the application of magnitudinal spectra, please refer to Sec. 3.2.4, Sec. 3.2.1, and Appx. A.8, respectively.

4.3.1 Detector-specific processing

For completeness, this section gives a short overview on errors induced by the detector. The current AtmoLITE instrument employs a silicon based CMOS sensor (GSENSE400BSI). There are three main sources of noise affecting image quality that stem from the detector: bad pixels, fixed pattern noise, and dark current.

Bad pixels are the result of malfunctioning pixels within the sensor, leading to either high or low pixel values, commonly referred to as bright and dark pixels. Correcting for bad pixels is essential as they interfere largely after applying Fourier transform. Florczak et al. (2022a) developed an adaptive bad pixel removal method based on the previous AtmoSHINE mission, which detects outlier and replaces it by the median kernel. This method relies on high resolution data without binning to generate a bad pixel map, which is used for onboard calibration before binning of 20 rows is applied. Frequent updates of the bad pixel map are necessary as the sensor's degradation in space leads to an increased number of bad pixels, as demonstrated by Florczak et al. (2022b). This proposed method can also be applied to the AtmoLITE instrument, and an assessment of the GSENSE detector's degradation will be conducted after launch of the INSPIRESat-4 mission.

Fixed pattern noise is a consistent and repeatable pattern of undesired variations in pixel values across images, which remains relatively constant from one measurement to another. This noise can originate from manufacturing imperfections in the sensor, variations in pixel sensitivity, and electronic noise. It can be estimated through dark calibration measurements with an integration time of 1 ms, and the resulting pattern can be subtracted during on-ground processing.

Dark current refers to the generation of electrical signal in the sensor due to thermal excitation of electrons, even when there is no incident light. This undesired signal increases exponentially with the sensor's temperature. To mitigate dark current, the detector in the AtmoLITE instrument is maintained at temperatures below 0°, ensuring minimal dark current.

Calibration data from the INSPIRESat-4 mission has shown that dark current is uniformly distributed across the 2D spatial plane within the designated region of interest. According to Liu et al. (2019), the dark current's intensity can be described

$$C_d = t_{int} \exp(aT + b) + o \tag{4.1}$$

where C_d is the uniform intensity across the 2D spatial plane, t_{int} denotes the integration time, T refers to the detector temperature, o is a fitted offset, and a and b are fitting parameters. These fitting parameters can be obtained from calibration measurements without a light source for various detector temperatures and integration times. During data processing, the dark current can be calculated based on the detector temperature, integration time, and the calibrated fitting parameters. This information can then be used for subtraction during on-ground processing. Nevertheless, since the dark current is uniformly distributed within the region of interest, it is also accounted for in the baseline correction as described in Section 4.3.4.

4.3.2 Image distortion correction

The optical system of the instrument induces certain distortions into the measurements, which results in a non-linear geometrical mapping from the object to the image. As mentioned in Sec. 3.1, the front optics map the atmospheric scene onto the gratings and the camera optics map the produced interference pattern at the gratings onto the detector. Distortion in the front optics displace the spectral information, whereas the camera optics distort the spectral information as well as the interferogram patterns, which are exhibited in the phase of the cosine waves. The latter is present in the calibration data, where straight lines that do not run through the optical center are bowed towards the optical center. This distortion, classified as radial distortion, is commonly referred to as pincushion distortion. Liu et al. (2019) points out for the previous instrument version AtmoSHINE, that the distortion of the front optics can be neglected compared to the distortion by the camera optics. This is also assumed for the current instrument version and will be validated in Sec.4.3.5 and Sec. 4.3.6. Furthermore, Liu et al. (2019) tested different correction methods based on simulated ray-tracing data, which

concluded that the division model, proposed by Fitzgibbon (2001), is most favorable to correct the radial image distortion. It is given by

$$r_d = \frac{1}{1 + kr_u^2} r_u \tag{4.2}$$

where r_d and r_u is the distorted and undistorted radius with respect to the optical center and k is a fitting parameter.

To evaluate the radial distortion, a calibration data set is generated, where a rectilinear grid target is put in the focal plane of a broadband light source covering evenly the bandpass filter of the instrument. It should be noted, that the superposition of all frequencies of the light source results in a spatially slow varying intensity variation without any fringe pattern. This allows to extract the grid points. A typical measurement of that grid target is shown in Fig. 4.10a. The background is estimated using a 2D Savitzky-Golay filter presented by Gowri et al. (2013). After subtracting the background, the area around the ZOPD is not considered due to the strong variation which is discussed in detail in Sec. 4.3.3. The points are detected by Laplacian of Gaussian (LoG) following Lindeberg (2013). Following this, the center is determined by fitting a parabolic curve to each row and column. The center position is then assigned to the point where the parabolic curve transitions into a linear line. However, due to the missing columns in close proximity to the center, linear interpolation across the square parameter of the parabola is applied. This process provides an initial guess for the optical center. Subsequently, the division model defined in Eq. (4.2) is employed to optimize both the optical center and the parameter k. The objective of this optimization is to minimize the spatial variation of points along a line, effectively restoring the rectilinear appearance of the grid.

This procedure is performed for multiple measurements where the temperature of the instrument and specifically of the optical system is varied. The results are shown in Fig. 4.11. The optimized parameter k of the division model and the y- and x-coordinate of the optical center do not show any trend with varying temperature of the optical system. The final parameters, referring to the mean, including their uncertainties, derived from the standard

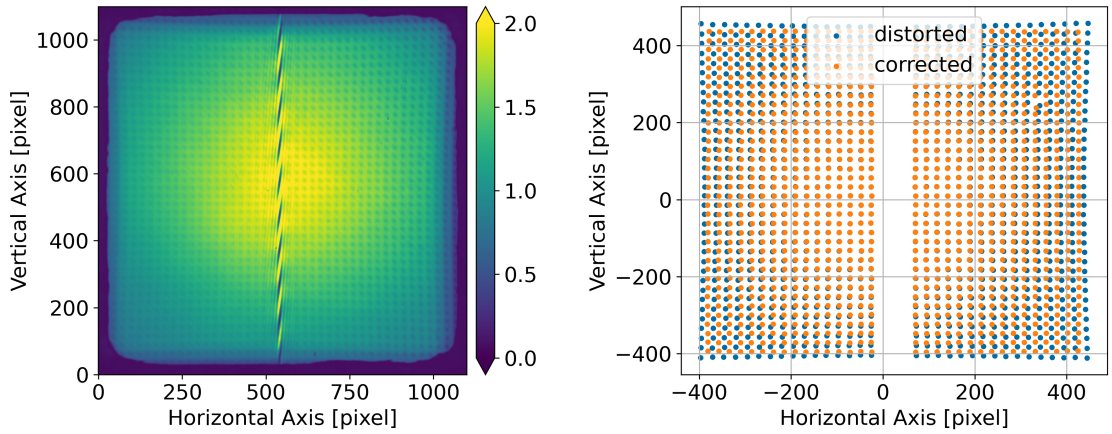

(a) (b)

Figure 4.10: (a) Measurement of rectilinear grid target; (b) detection of grid points and corrected grid after correction with the optimized radial distortion parameters.

deviation, are shown in Tab. 4.3.

A measured interferogram can be corrected by calculating the distance of each pixel with respect to the optical center, indicating the undistorted radius. Based on the undistorted radius the distorted radius is calculated using the division model given in Eq. (4.2), defining the positions of the distorted values. A mapping of the values at the distorted position to the undistorted position is performed. Note that the distorted position may lie on a sub-pixel position, where 2D interpolation is performed. One example is given in Fig. 4.12, where an interferogram is simulated with the radial distortion parameter k given in Tab. 4.3 for a temperature level of 200 K. The comparison of a spectrum for an ideal instrument without radial distortion and for an instrument with radial distortion in Fig. 4.12a reveals that the emission lines are shifted towards lower frequencies. Furthermore, it shows that higher frequencies are more affected than lower frequencies. When looking at a single ILS in Fig. 4.12b the same effect is present. This comes from the fact that the radial pincushion distortion pushes the fringe pattern radially away from the center and thus decreases the averaged frequency of one row. Furthermore, the shift toward lower frequencies increases also the side lobes corresponding to the lower frequencies. Correcting for radial distortion as explained above can eliminate most of the spectral differences as shown in Fig. 4.12a. Results of the temperature retrieval show

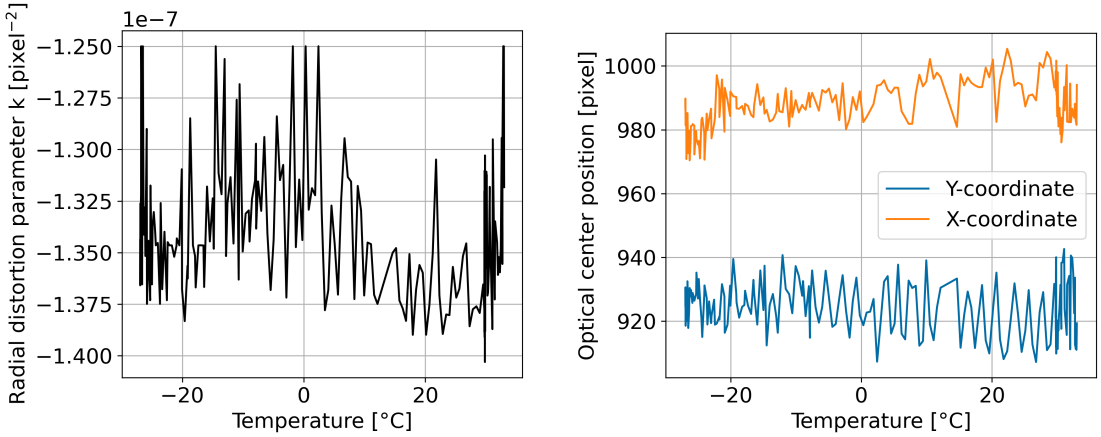

(a) (b)

Figure 4.11: Radial distortion parameter calibration for several temperatures of the optical system; (a) parameter of division model; (b) optical center; the pixel count of the optical center is given for the entire detector size of 2000 × 2000 pixels.

Table 4.3: Radial distortion parameters derived from Fig. 4.11; the value and uncertainty is given by the mean and standard deviation along the temperature axis.

Parameter	Value	Uncertainty
Fit parameter of division model k	$-1.35 \times 10^{-7}\,\mathrm{pixel}^{-2}$	$3.19 \times 10^{-9}\,\mathrm{pixel}^{-2}$
Optical center x-axis	990.6 pixel	7.2 pixel
Optical center y-axis	923.7 pixel	8.3 pixel

in Fig. 4.12c that if no radial distortion correction is applied, temperature errors up to 6 K occur in the upper and lowermost rows. It is thus crucial to apply radial distortion correction, which eliminates the temperature errors almost completely.

As last step, the sensitivity of the temperature retrieval to radial distortion and specifically to falsely derived radial distortion parameters are assessed. To this end, an interferogram is simulated with the radial distortion parameter k given in Tab. 4.3 for a temperature level of 200 K as before. This time however the interferogram is corrected with parameters being perturbed with the uncertainties given in Tab. 4.3. The results are shown in Fig. 4.13. The effect of perturbing the fit parameter of the division model increases with the distance of the pixels from the optical center, entailing the largest temperature errors of 0.5 K in the upper and lower rows. Perturbing the x-coordinate of the optical center has minimal impact

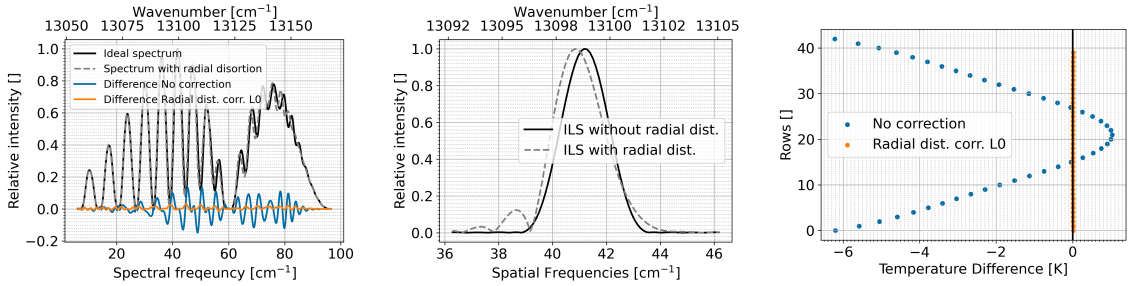

(a) (b) (c)

Figure 4.12: (a) Comparison of ideal and distorted spectra, along with the corresponding differences, in the case of processing with and without radial distortion correction; the spectra are presented for row 20. (b) ideal ILS compared to ILS including radial distortion; (c) temperature retrievals for different processing modes with binning of 20 rows

on temperature retrieval. However, perturbing the y-coordinate of the optical center shows larger temperature errors of 0.8 K for the upper and lower rows. The observed differences can be explained by the interferogram equation including radial distortion for a monochromatic input. The modulated part is expressed as

$$I_\sigma(x,y) = \cos\left(2\pi f(\sigma)\frac{1}{1+k\sqrt{(\Delta x)^2+(\Delta y)^2}}x\right) \tag{4.3}$$

where Δx and Δy are the distances of x and y with respect to the optical center, respectively, and σ refers to the frequency of the incoming light. Along the x-axis, the radial distortion induces a larger phase shift in areas farther away from the optical center, but only a minimal phase shift in areas near the optical center. As the Fourier transformation is applied along the x-axis, an averaged frequency information is extracted from the distorted cosine wave. This results in a subtle shift towards lower frequencies, as illustrated in Fig. 4.12b. This explains the low sensitivity of the temperature retrieval with respect to perturbation on the x-coordinate of the optical center. If however, Δy is not perfectly known, it induces larger errors onto all frequencies when Δy is large, such as for the top and bottom rows. This also explains why temperature errors are nearly negligible close to the optical center in row 20 but increase linearly with Δy. This highlights the greater precision required for determining the y-coordinate of the optical center compared to the x-coordinate. Furthermore, it's important

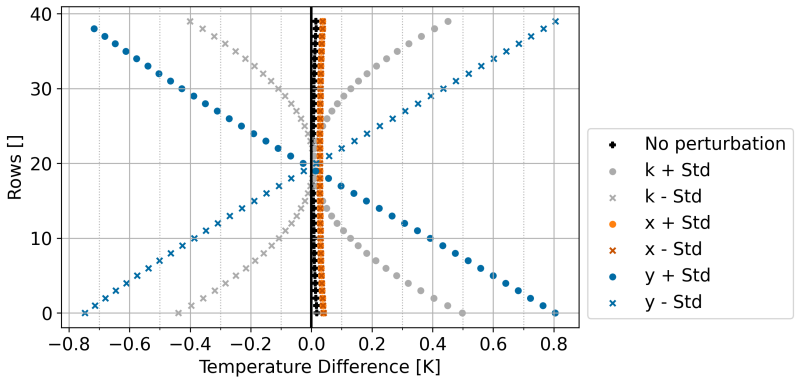

Figure 4.13: Sensitivity of temperature retrieval to perturbation in the radial distortion parameters given in Tab. 4.3; k refers to the fit parameter in the division model, x and y to the respective coordinate of the optical center; the standard deviation is taken from the uncertainties in Tab. 4.3; note that the results of 'x + Std' and 'x - Std' lie on top of each other.

to recognize that this effect becomes more pronounced at higher temperatures due to the declining sensitivity of the O_2 A-band at higher temperatures, as discussed in Sec. 2.2 and Sec. 4.2. Further discussions on radial distortion and its connection to phase distortion and the Littrow calibration are given in Sec. 4.3.5 and Sec. 4.3.6, respectively. It is worth emphasizing that incorrectly corrected radial distortion can still be addressed through phase correction.

In summary, the correction for radial distortion is crucial for obtaining a precise temperature product. Although the presented correction method demonstrates robust performance, it exhibit higher sensitivity to both the fit parameter k of the division model and the y-coordinate of the optical center. These parameters can be determined through calibration using a grid target; however, to further enhance the reliability of this method, efforts should be made to reduce the uncertainty associated with these determinations. Currently, the method's uncertainty can be as high as 1 K for temperatures at 200 K, which are present in the upper mesosphere and mesopause region. To enhance calibration accuracy, it is recommended to perform measurements without a grid target. This will enable the subtraction of variations around the ZOPD, thereby allowing for the detection of more points in closer proximity to the optical center. This refinement is expected to improve calibration precision.

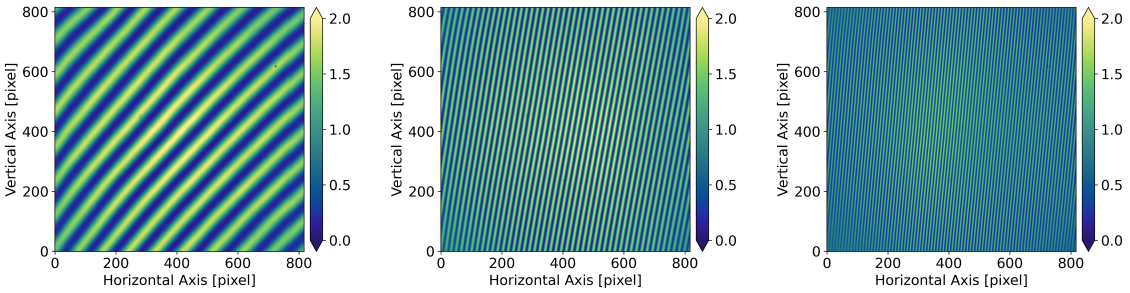

(a) (b) (c)

Figure 4.14: Example of monochromatic interferograms with spatial frequency (a) $9.44\,\mathrm{cm}^{-1}$, (b) $51.82\,\mathrm{cm}^{-1}$, (c) $92.57\,\mathrm{cm}^{-1}$

4.3.3 Barber's pole correction

Misalignment of the two gratings induces a rotation of the fringe pattern, when looking at monochromatic calibration data presented in Fig. 4.14. Since the instrument measures multiple emissions, the different fringe patterns are superimposed producing a Barber's pole like structure around the ZOPD, as shown in Fig. 4.16a. Revisiting Fig. 3.1, a grating can be misaligned by rotating it around its surface normal or by tilting it perpendicular to the dispersion direction. Wroblowski (2023) employed ray-tracing simulations and showed that both effects results in a rotation of the fringe pattern, where the rotation of the fringes is 10 times more sensitive to the grating tilt. In the following mathematical derivation, only the tilt of the two gratings are considered. The correction method however, extracts its knowledge from the rotation of monochromatic calibration data and thus includes both effect.

The mathematical derivation of a 2D monochromatic interferogram including a tilt perpendicular to the dispersion direction in the two gratings is shown in Sec. A.10, denoted by

$$I_\sigma(x,y) = \frac{1}{2}R(\sigma)\left[1+\cos(2\pi(f(\sigma)x+\alpha\sigma y))\right] \tag{4.4}$$

where $\alpha/2$ is the misalignment angle between the two gratings, x and y are the spatial variable of the horizontal and vertical axis, and $f(\sigma)$ is the spatial frequency corresponding to the wavenumber σ, defined in Eq. (3.3). The rotation of the monochromatic fringe pattern

with respect to the x-axis is represented by the angle η, which is derived from the vertical and horizontal wavelengths through the relationship

$$\tan\,\eta = \frac{\lambda_y}{\lambda_x} = \frac{f_x}{f_y} = \frac{4(\sigma - \sigma_L)\tan(\theta_L)M^{-1}}{\alpha\sigma}. \tag{4.5}$$

Assessing the limits for η assuming $\alpha \neq 0$ shows that

$$\lim_{\sigma\to\sigma_L} \eta = 0 \tag{4.6}$$

$$\lim_{\sigma\to\infty} \eta = \tan^{-1}\left(\frac{4\tan(\theta_L)M^{-1}}{\alpha}\right). \tag{4.7}$$

To put it in words, if an misalignment between the two gratings is present, the fringes will align horizontally for wavenumbers close to Littrow, especially noticeable at lower spatial frequencies. In real world application, due to imperfections of the grating alignment, this will always be the case. If the misalignment angle is a lot smaller than the Littrow angle ($\alpha \ll \theta_L$), wavenumbers away from Littrow produce a vertical fringe pattern as a perfect instrument suggests and are therefore, less affected by the misalignment.

The misalignment angle α can be derived from the rotation angle of monochromatic measurements. For each measurement, the rotation angle is estimated with respect to the horizontal axis using automatic contour detection, where the orientation of each contour is detected by Principal Component Analysis (PCA) following Wold et al. (1987). An example is shown in Fig. 4.15a for one frequency. Applying this to multiple monochromatic measurements and converting the rotation angle to the misalignment angle by Eq. (4.5) gives the results in Fig. 4.15b, which demonstrate a stable estimate of the misalignment angle over the frequency space.

To correct the rotation of the fringe patterns, a line-by-line model is assumed. Following Eq. (4.4) the modulated part of a 2D interferogram can be described by

$$I(x,y) = \frac{1}{2}\sum_{n=1}^{N} R(\sigma_n)\cos(2\pi(f(\sigma_n)x + \alpha\sigma_n y)) \tag{4.8}$$

$$= \frac{1}{2}\sum_{n=1}^{N} R(\sigma_n)\frac{1}{2}\left[e^{i2\pi f(\sigma_n)x}e^{i2\pi\alpha\sigma_n y} + e^{-i2\pi f(\sigma_n)x}e^{-i2\pi\alpha\sigma_n y}\right], \tag{4.9}$$

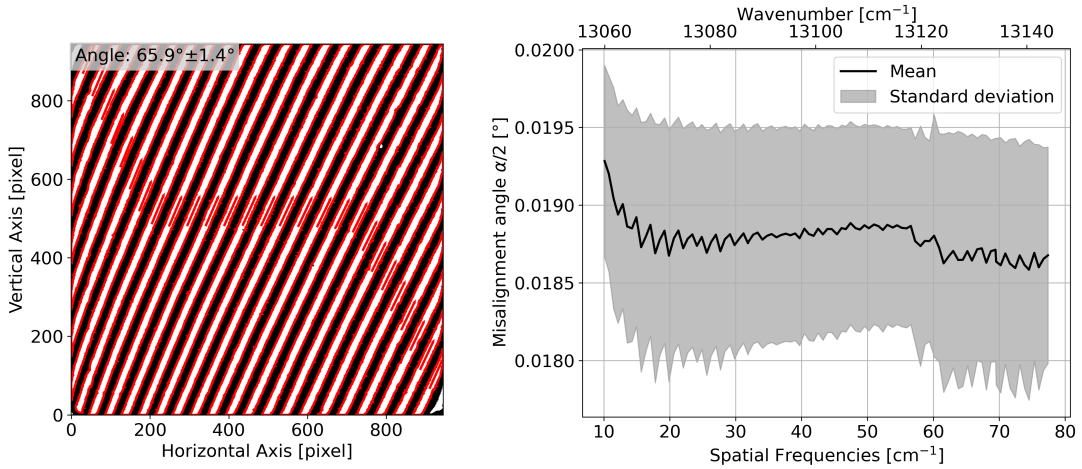

(a) (b)

Figure 4.15: (a) Angle of rotation estimation with respect to horizontal axis using automatic contour detection (red border lines) and orientation determination by PCA (red arrows); (b) misalignment angle between the gratings derived from the rotation angle following Eq. (4.5) for monochromatic measurements with various spatial frequencies; the standard deviation in (b) is the propagation of the standard deviation of the angle estimation in (a).

where N is the number of emission lines and Euler's theorem is applied in Eq. (4.9). Taking the Fourier transformation along the x-axis gives

$$\mathcal{F}(I)(\kappa, y) = \frac{1}{4} \sum_{n=1}^{N} R(\sigma_n) \left[F_{ILS}(\kappa - f(\sigma_n)) e^{i2\pi\alpha\sigma_n y} + F_{ILS}(\kappa + f(\sigma_n)) e^{-i2\pi\alpha\sigma_n y} \right]. \quad (4.10)$$

Hence, the tilt of the gratings results in a phase variation that depends solely on the spectral axis for a given row. It should be noted that since the Fourier transformation is applied along the x-axis, y acts as a scalar in the phase component $e^{i2\pi\alpha\sigma_n y}$. In theory, it is eliminated when working with absolute spectra as discussed in Sec. 3.2.1. When working with complex spectra, the interferogram can be corrected by multiplying the negative and positive frequencies with $e^{i2\pi\alpha\sigma_n y}$ and $e^{-i2\pi\alpha\sigma_n y}$, respectively. Both approaches assume an infinitesimally small resolution of the ILS. However, real-world applications do not meet this assumption, as finite interferograms induce a broad ILS with infinite support as shown in Sec. 3.2.2. Thus, the phase component induced by the grating misalignment does not only

influence the local support of the Dirac-impulse, but an infinitely wide spectral range of the ILS. Apodization, introduced in Sec. 3.2.4 can help here, which increases the degree of localization of the ILS as depicted in Fig. 3.3b.

To show this in an example, an interferogram including the misalignment of the gratings is simulated using Eq. (4.8) with a constant temperature of 200 K over the entire field of view. The misalignment of the gratings is set to the mean angle derived from calibration data in Fig. 4.15b. Subsequently, a temperature retrieval of a homogeneous gas cell is performed row-wise as explained in Sec. 3.4.2. The simulated interferogram with grating misalignment is presented in Fig. 4.16a. For reference, the spectra without grating misalignment are presented in Fig. 4.16b for both the case without apodization and with Norton-Beer strong apodization. Furthermore, the deviations in spectra resulting from grating misalignment are depicted for both scenarios. This analysis highlights that with the application of apodization, the observed spectral differences are considerably diminished. This reduction is attributed to the diminished side lobes resulting in improved temperature retrieval performance, as demonstrated in Fig. 4.16c. The wavy pattern evident in the retrieved temperature aligns with twice the vertical frequency component of the Barber's pole. Furthermore, Fig. 4.16d illustrates temperature errors in the case where vertical binning of 20 rows is applied as it is typically carried out in the onboard processing. The outcomes appear scattered and lack a clear pattern. Nevertheless, the results remain within the same range of temperature error as seen without binning.

An interferogram can still be approximately corrected, by taking the Fourier transformation, multiplying the inverse phase component for the positive and negative spectral area, and apply inverse Fourier transformation. The result is an interferogram with a straight fringe pattern, as it is shown in Fig. 4.17. Such a correction might be applied, for instance, when searching for the ZOPD when working with complex spectra instead of absolute spectra. Notably, this correction becomes particularly crucial for the novel processing technique explored in Chapter 5, which divides the field of view at the center to extract two temperature values from a single row. However, applying this correction step cannot recover perfectly the undistorted interferogram as shown in Fig. 4.17c, due to the infinite support of the ILS as explained above. A processing including the correction method results in the same temperature error

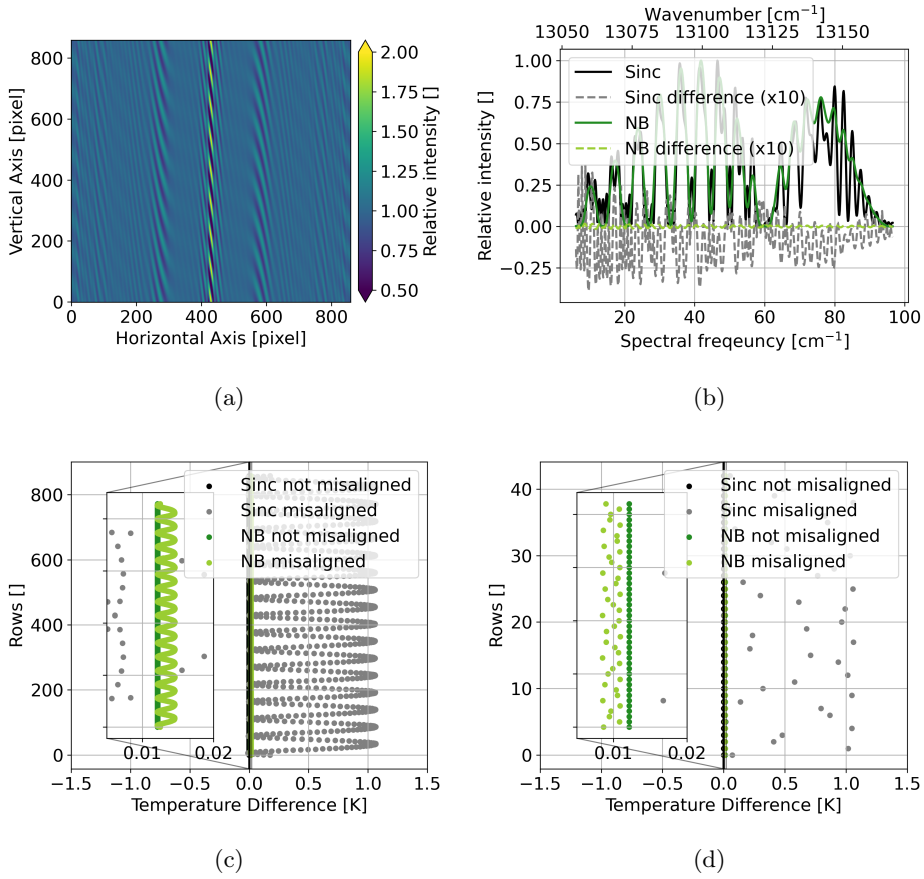

Figure 4.16: (a) Interferogram simulation including grating misalignment; (b) Analytical spectrum without grating misalignment for the case without apodization (sinc) and with apodization using Norton-Beer strong; corresponding spectral differences of spectra including grating misalignment shown as dashed lines; (c) temperature differences in the retrieval, and (d) temperature differences in the retrieval with binning of 20 rows

ranges as in the case without correction.

In conclusion, grating misalignment induces a rotation of the fringe pattern, with the rotation angle dependent on the incident light's frequency. Measuring a poly-chromatic radiance results in a Barber's pole like pattern encircling the ZOPD. Due to the infinite support of the ILS, complete analytical correction of this error is unattainable. Nonetheless, its impact can be sufficiently reduced using apodization. In the context of Barber's pole variation, it's important to note that correction remains feasible, resulting in an interferogram with straight lines. While this correction does not directly enhance temperature accuracy, it proves beneficial for other processing stages such as ZOPD determination and the application of split field of view

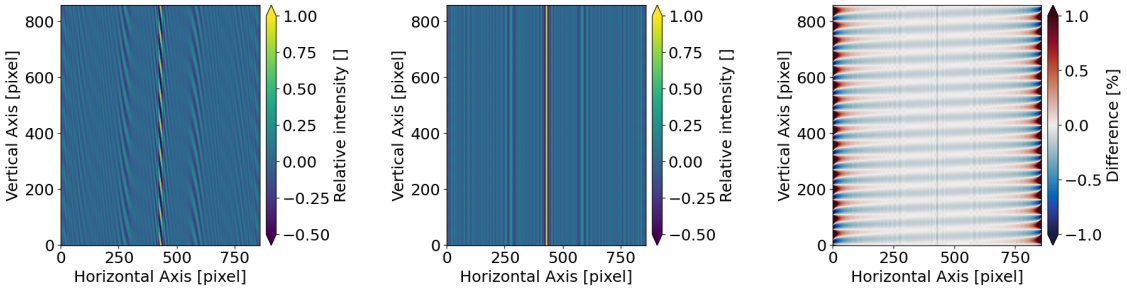

(a) (b) (c)

Figure 4.17: (a) Interferogram simulation including grating misalignment; (b) corrected interferogram using grating misalignment correction; (c) difference between the corrected and the ideal interferogram

retrievals.

4.3.4 Baseline and amplitude correction

Distortion of the optical path due to an imperfect optical system induces an intensity and contrast variation into the raw data. A common effect is a gradual decrease in brightness from the center of the image towards the periphery, which is also known as vignetting. It is thus mainly a spatial variation of image's brightness. Furthermore, variation in contrast and therefore the envelope of the sinusoidal wave are typical for an SHI instrument (Englert and Harlander, 2006; Langille et al., 2019). This section thus shows a method how to extract the intensity and contrast variation from monochromatic measurements and presents a correction method using the extracted information.

A 2D monochromatic interferogram with an intensity and contrast variation is given by

$$I_\sigma(x,y) = R_\sigma \left[B_\sigma(x,y) + A_\sigma(x,y) \cos(2\pi f(\sigma) x) \right], \tag{4.11}$$

where x and y are the horizontal and vertical spatial variable, respectively, B_σ refers the intensity variation in the non-modulated part, A_σ denotes the envelope of the modulated part and σ is the wavenumber of the incident light. Subsequently, B_σ and A_σ are called baseline and amplitude, respectively.

Englert and Harlander (2006) proposed to measure the baseline or so called flatfield during

on-ground calibration by blocking each grating individually. This procedure prevents interference from occurring and enables the measurement of spatial intensity distribution across the field of view for each arm, which can be subsequently used to correct the interferogram. This approach however assumes that the baseline is independent in spatial and spectral variables, allowing it to be split into spatial and spectral components. These components are then treated separately during L0- and L1-processing. However, this assumption does not hold for the presented instrument, as demonstrated later in this section. In light of these considerations, an alternative correction method is presented, aiming to estimate the baseline from monochromatic calibration data. This data, already used for various other calibration steps such as extracting amplitude (in this section) or phase (in Sec. 4.3.5), renders the individual flatfield calibration procedure redundant, thereby saving valuable calibration time. The following paragraph presents the proposed baseline and amplitude estimation method, followed by its application to monochromatic calibration data obtained for the INSPIRESat4 mission. Subsequently, a correction method is outlined along with its efficacy.

The baseline can be estimated using a 2D Savitzky-Golay filter presented by Gowri et al. (2013). An example for spatial frequency close to $15\,\mathrm{cm}^{-1}$ is shown in Fig. 4.18b and 4.18e. Subsequently, the baseline is subtracted isolating the modulated part of the interferogram. Following Luo et al. (2009), the envelope of a signal can be estimated by the absolute value of the complex analytical signal denoted here by

$$Z(x) = \tilde{I}(x) + i\hat{I}(x) \tag{4.12}$$

where $\tilde{I}$ is the modulated part of a one dimensional interferogram and $\hat{I}$ is the Hilbert transform of $\tilde{I}$. The Hilbert transform is defined by

$$\hat{I}(x) = \frac{1}{\pi x} * \tilde{I}(x) \tag{4.13}$$

which corresponds to a 90° positive phase shift for positive frequency components and a 90° negative phase shift for negative frequency components. The absolute value of the complex signal then estimates the envelope. Applying this procedure row wise and smoothing the result

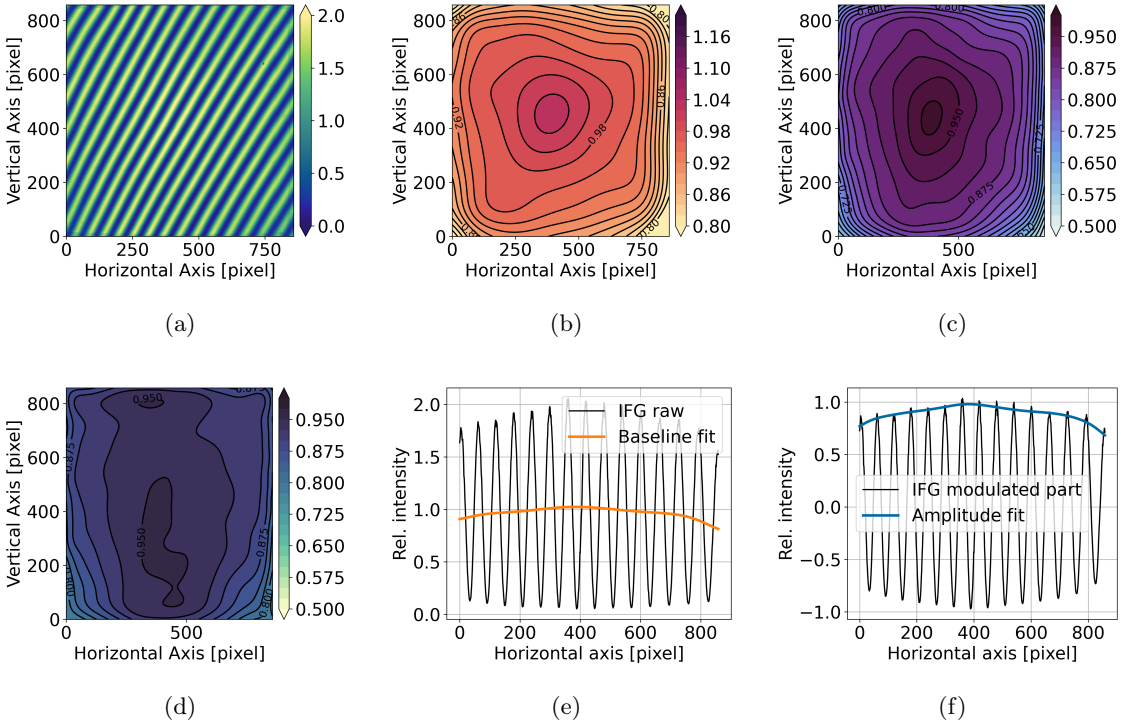

Figure 4.18: (a) Normalized interferogram; (b) baseline fit using 2D Savitzky-Golay filter; (c) amplitude fit by performing Hilbert transformation along the horizontal axis and subsequent smoothing by 2D Savitzky-Golay filter; (d) visibility defined as the ratio of amplitude and baseline; cross-section of (e) baseline and (f) amplitude fit at row 400, respectively; spatial frequency of 14.93 cm^{-1} is selected.

with a 2D Savitzky-Golay filter gives a smooth 2D variation estimate of the envelope field as presented in Fig. 4.18c and Fig. 4.18f. The ratio between envelope and baseline, also known as visibility, gives a measure how much of the signal strength enters the modulated part, which is used for the temperature retrieval. The goal is to achieve a high visibility, which increases the usable signal strength and therefore increases the temperature precision. The visibility of the example is shown in Fig. 4.18d.

Monochromatic measurements were conducted across various wavelengths to cover the entire range of the bandpass filter. For each measurement, the baseline, amplitude, and visibility was estimated, as explained in the preceding paragraph. In Fig. 7.11, these three estimates are illustrated for a range of spatial frequencies. The baseline fields shown in Fig. 7.11b exhibit a spectral variation with a sharper peak and higher spatial variation for increasing frequencies.

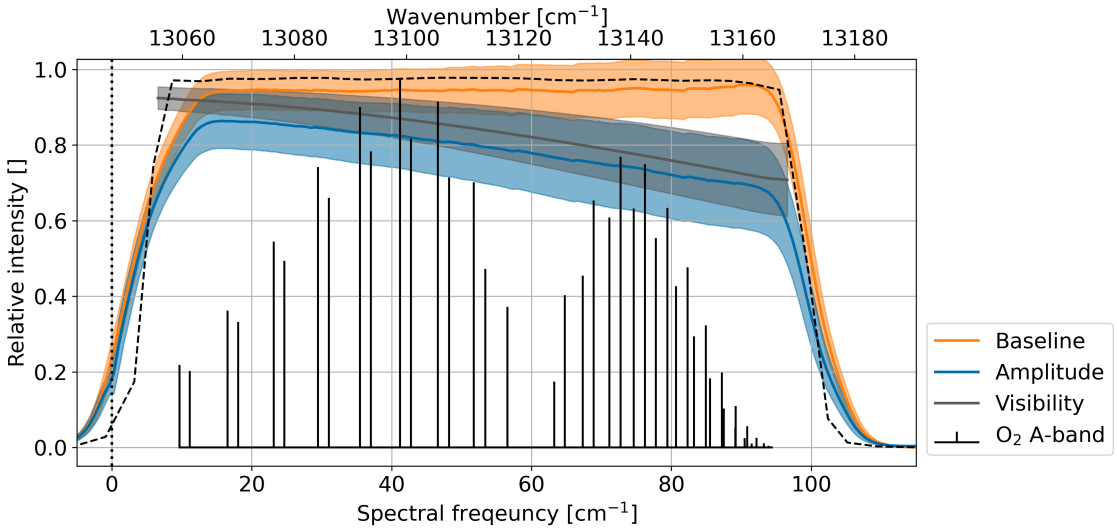

Figure 4.19: Baseline, amplitude and visibility estimates derived from monochromatic measurements for several wavelengths ranging over the frequency range of the O_2 A-band emission; mean (solid line) and standard deviation (shaded area) are calculated across the spatial detector field for each estimate and given frequency; Littrow wavenumber and theoretical filter curve of the band pass filter are shown by the dotted vertical and dashed line, respectively; O_2 A-band emissions at 200 K are shown for orientation.

This shows that the baseline is not independent in the spatial and spectral variables. The amplitude fields displayed in Fig. 7.11c show a decrease and a downward-shifted peak for higher spatial frequency. These two effects cause a decrease and a doughnut shape in the visibility for higher frequencies as portrayed in Fig. 7.11d. In Figure 4.19, the mean and standard deviation over the spatial domain is presented for the entire frequency space. The baseline estimate closely aligns with the theoretical filter curve, displaying minor deviations primarily at the edges. Also here, the larger variation for higher spatial frequencies is visible. The decrease in amplitude, leading to a corresponding decrease in visibility at higher spatial frequencies, is attributed to imperfections in the camera optics, which induces a subtle smearing effect into the wave fronts and consequently affect the interference pattern. This effect decreases the contrast, which affects higher frequencies more. Consequently, the average visibility decreases from 92 % at low spatial frequencies to 70 % at high spatial frequencies.

To correct these two effects, again a line by line model is used. An interferogram consisting of multiple emission lines thus is given by

$$I(x,y) = \sum_{n=1}^{N} R_{\sigma_n} B_{\sigma_n}(x,y) + \sum_{n=1}^{N} R_{\sigma_n}(x,y) A_{\sigma_n}(x,y) \cos(2\pi f(\sigma_n) x) \tag{4.14}$$

where the first term is the non-modulated part, governed by the baseline variation and the second part is the modulated part distorted by the amplitude variation. It should be noted that since a line-by-line model is assumed, also the baseline and amplitude variation are needed only for the frequencies of the emission lines. Since the two measures are slowly varying along the spectral axis as shown in Fig. 7.11, linear interpolation along the spectral axis is employed to extract the baseline and amplitude corresponding to the emission lines. The non-modulated part can be estimated using again a 2D Savitzky-Golay filter. Subtracting the non-modulated part isolates the modulated part of the interferogram. If the amplitude did not vary with frequency, it could be corrected by multiplying the inverse value of the amplitude onto the modulated interferogram. This however is not hold as presented in Fig. 7.11c. It is frequency and location dependent and therefore, needs to be corrected indirectly via the ILS, as shown in the following. To analyze the influence of the amplitude variation onto the spectrum, the Fourier transform of the modulated part in Eq. (4.14) is taken, denoted by

$$\begin{aligned} \mathcal{F}(I(\cdot,y))(\kappa) = \sum_{n=1}^{N} R_{\sigma_n} [&\mathcal{F}\left(A_{\sigma_n}(\cdot,y)\right)(\kappa) * F_{ILS}(\kappa - f(\sigma_n)) + \\ &\mathcal{F}\left(A_{\sigma_n}(\cdot,y)\right)(\kappa) * F_{ILS}(\kappa + f(\sigma_n))] \end{aligned} \tag{4.15}$$

where F_{ILS} is the ILS governed by the apodization function. The ILS thus is slightly distorted by the Fourier transform of the extracted amplitude. Since the amplitude shows a 2D bell shape spatial variation, it acts like a very soft apodization function and broadens the ILS. To correct for the amplitude variation, the ILS in the forward model is manipulated accordingly.

To show the efficacy of the correction method, a simulation example is conducted in the following. Hereby, a 2D interferogram is simulated for a constant temperature of 200 K following Eq. (4.14), which incorporates a baseline and amplitude variation derived from monochromatic calibration data. Figure 4.20a shows an ideal spectrum without any baseline or amplitude vari-

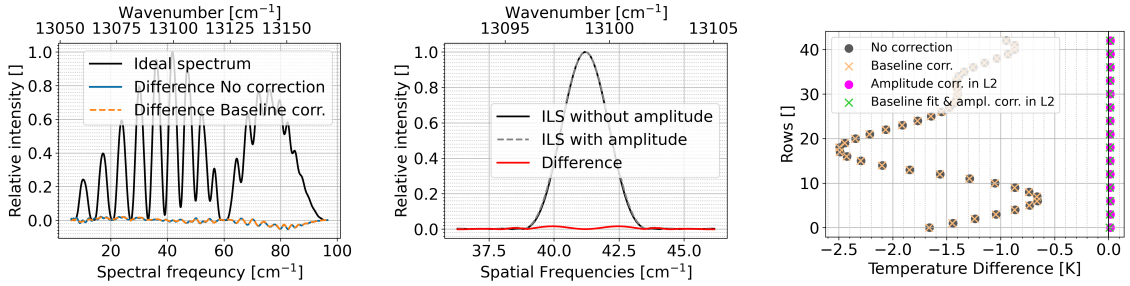

(a) (b) (c)

Figure 4.20: (a) Ideal spectrum and difference of spectra including baseline and amplitude, where for the non-modulated part the mean value of the interferogram ('No correction') and a baseline fit is subtracted ('Baseline corr.'); (b) ideal ILS compared to the ILS including amplitude variation; (c) temperature retrievals for different processing modes with binning of 20 rows; note that only every third data point is shown for the two retrievals close to 0 K.

ation as a reference. It also displays the differences between spectra including baseline and amplitude components with respect to the reference for two processing methods. The first processing method eliminates the non-modulated by simply subtracting the mean value of the interferogram referring to 'no correction'. The second method estimates the baseline by a Savitzky-Golay filter and subsequently subtracts it, referring to 'baseline correction'. Both processing methods show similar differences with respect to the ideal spectrum. This comes from the fact that the baseline is slowly varying over the spatial domain which only affects frequencies close to zero. These frequencies are outside of the filter and therefore not considered in the optimization process of the retrieval. It should be noted that the here applied Norton-Beer strong apodization confines this effect to the lower frequencies. For weaker apodization functions, the effect of the baseline variation can affect higher frequencies due to the increased side lobes. The effect of decreasing amplitude for higher frequencies is also visible here, when looking at spatial frequencies above 60 cm^{-1}. The slight ILS broadening due to the amplitude's bell shape variation is presented in Fig. 4.20b. The ILS incorporating the amplitude variation as explained in Eq. (4.15) shows a slight increase of 2 % at the flanks. The effect of these manipulations are assessed in a temperature retrieval following Sec. 3.4.2. Figure 4.20c shows the results, where a binning of 20 rows is applied. It reveals that the baseline variation and therefore also its correction in fact has a very little influence onto the temperature retrieval.

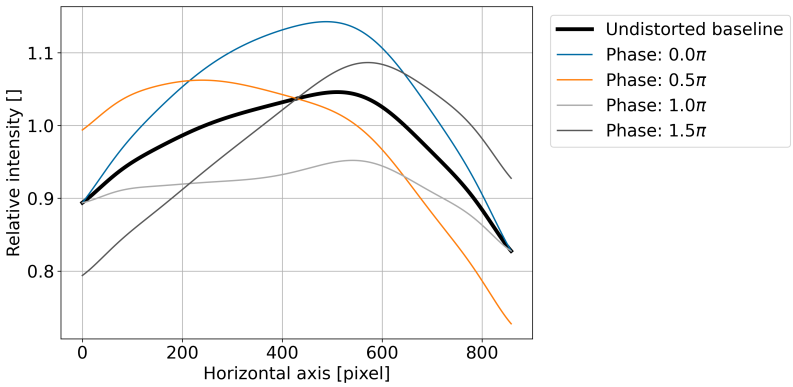

Figure 4.21: Example of baseline distortions for varying phase; measured baseline at spatial frequency equal to 46.6 cm^{-1} (undistorted baseline) used as reference; distorted baselines are the sum of undistorted baseline and a half-wave sinusoidal perturbation following Eq. (4.16) with amplitude equal to 0.1 and phase given in the legend for the individual lines.

The amplitude variation however shows a larger effect onto the retrieval, inducing a temperature error up 2.5 K, if it is not corrected. The amplitude correction in L2 processing however, is very effective and can mitigate the error down to less than 0.1 K.

To assess the sensitivity of the baseline and amplitude variation onto the retrieved temperature, both are perturbed separately by adding a sinusoidal perturbation defined by

$$C(x) = A_d \sin(\pi x + \phi_d) \tag{4.16}$$

where A_d refers to the amplitude and ϕ_d to the phase of the distortion. The variable x is normalized by the interferogram length such that it ranges from 0 to 1. The distortion thus is half a sinus wave with different phase shifts scaled by different amplitudes. An example for the baseline distortion with varying phase and constant amplitude equal to 0.1 is shown in Fig. 4.21.

Subsequently, an interferogram is simulated with the perturbed baseline or amplitude. In the processing, the mean value of the interferogram is subtracted to eliminate the non-modulated part. Thus, the baseline is not specifically corrected. Furthermore, the amplitude variation extracted from the calibration data is incorporated into the ILS. These simulations hence show, how accurate the baseline and amplitude needs to be known from calibration data. The whole process is performed for several sinusoidal perturbations, where A_d and ϕ_d

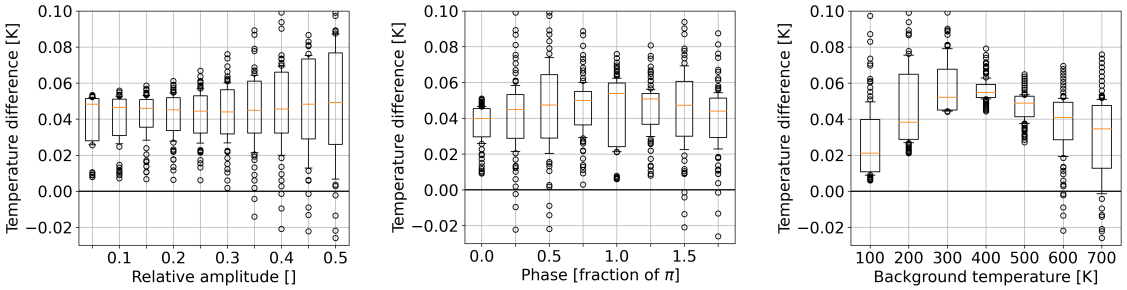

(a) (b) (c)

Figure 4.22: Sensitivity of temperature retrieval to disturbed baseline variation; the additive disturbance is defined in Eq. (4.16); results are shown for different (a) amplitudes, (b) phases and (c) simulation temperatures; whisker of the boxplots show the 16th and 84th percentile corresponding to the standard deviation of a Gaussian distribution.

are varied. Furthermore, the analysis is conducted for several temperature levels, to account for the changing sensitivity of the O_2 A-band emissions with respect to temperature as discussed in Sec. 2.2 and Sec. 4.2.

The results concerning the perturbation in baseline are displayed in Fig. 4.22. These results reveal that temperature retrieval exhibits minimal sensitivity in response to baseline variation. Note that the baseline variation is not treated specifically and still it propagates only small errors into the temperature retrieval below 0.1 K, even for perturbations up to 50 % (distortion amplitude of 0.5 in Fig. 4.22a). These results are similar to the result in Fig. 4.20c, following an analogous explanation.

The results for the amplitude perturbation are shown in Fig. 4.23, which show an overall higher sensitivity. Figure 4.23a illustrates that as the amplitude or strength of the perturbation increases, there is a corresponding rise in the temperature error, following the intuitive expectations. The phase of the distortion plays an important role. Figure 4.23b shows, that if the added perturbation is close to linear (0.5π and 1.5π), the effect onto the temperature retrieval is marginally small. However, an added down- and up-facing perturbation results in larger positive and negative temperature errors, respectively. It should be noted, that the temperature errors increases with the temperature level as shown in Fig. 4.23c. To cover all temperatures up to 700 K referring to altitudes up to 140 km with a temperature error of less than 1 K, the amplitude needs to be determined with an accuracy of 3 %. The Savitzky-Golay

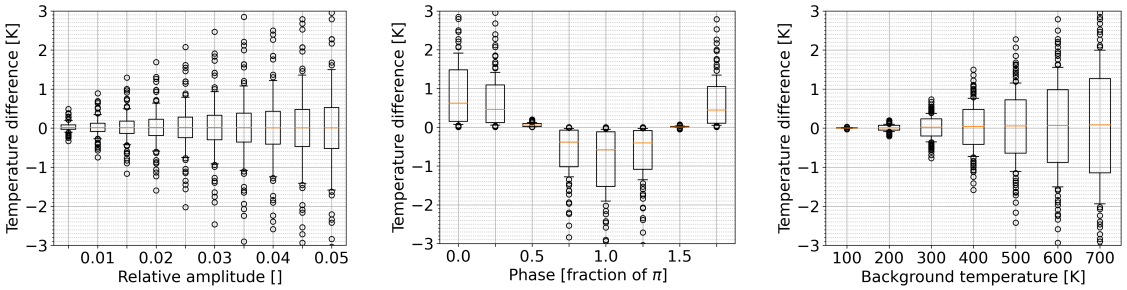

(a) (b) (c)

Figure 4.23: Sensitivity of temperature retrieval to disturbed amplitude variation; the additive disturbance is defined in Eq. (4.16); results are shown for different (a) amplitudes, (b) phases and (c) for different simulation temperatures; whisker of the boxplots show the 16th and 84th percentile corresponding to the standard deviation of a Gaussian distribution.

filter is capable to estimate the baseline and amplitude with an accuracy of less than 1 % under ordinary condition and with some user expertise as shown in an example in Appx. A.12.

In summary, the baseline correction is of lesser significance, given that temperature retrieval exhibits low sensitivity to baseline variations. These variations primarily affect lower spatial frequencies, which are excluded from the optimization process. However, the amplitude variation plays a more substantial role. Firstly, the decreasing amplitude towards higher frequencies also damps higher frequencies in the spectrum. Secondly, the spatial bell shape of the amplitude slightly broadens the ILS of the individual emission lines. Consequently, these two effects entail an increased sensitivity of the temperature retrieval to amplitude variations, necessitating an indirect correction by assimilating the variation into the ILS. Moreover, the sensitivity analysis demonstrated that the amplitude should be determined in a 3 % range, to acceptably mitigate the temperature error induced by the amplitude variation. It is important to emphasize that the amplitude estimate depends on the baseline estimation of a monochromatic interferogram. Consequently, a careful evaluation of baseline estimations is equally essential.

4.3.5 Phase correction

Phase distortion refers to alterations in the wave front's shape, leading to spectral distortions after the Fourier transformation. Consequently, this phenomenon can introduce errors in the

temperature derivation. It can be caused by multiple error sources, some of which have already been discussed. For instance, the misalignment of the gratings presented in Sec. 4.3.3 causes a row-dependent phase shift which results in the rotation of the fringe pattern. Another example is the radial image distortion shown in Sec. 4.3.2, which drags the fringe pattern towards the optical center, causes an increasing phase distortion with spatial frequency and with distance from that center. Another frequently encountered error source arises from the imperfect sampling of the continuous interferogram by the detector pixels, where the ZOPD falls on a sub-pixel position. This leads to a minor shift in the interferogram, inducing a linearly increasing phase with frequency, independent of the spatial domain. This phenomenon is commonly known as a phase shift (Englert et al., 2004; Forman et al., 1966; Brault, 1987). Other imperfections within the optical system and errors in the gratings introduce phase distortions that not only vary with frequency but also span across the detector area.

The investigation into phase distortion starts with a presentation of the foundational mathematical background, which is the base for the correction method, mainly following Englert et al. (2004). Subsequently, the extracted phase estimations from the monochromatic calibration data are shown. Finally, a correction method is presented along with its efficacy.

The modulated part of an interferogram including phase distortion is denoted by

$$I(x,y) = \frac{1}{2}\sum_{n=1}^{N} R_{\sigma_n}\left(e^{i[2\pi f(\sigma_n)x + \Phi_{\sigma_n}(x,y)]} + e^{-i[2\pi f(\sigma_n) + \Phi_{\sigma_n}(x,y)]}\right) \tag{4.17}$$

where x and y are the horizontal and vertical spatial variable, respectively, σ_n refers to the wavenumbers of the emission lines, and Φ_{σ_n} refers to the phase distortion at wavenumber σ_n. Applying the Fourier transformation to Eq (4.17) gives

$$\begin{aligned}\mathcal{F}(I(\cdot,y))(\kappa) = \sum_{n=1}^{N} R_{\sigma_n}[&\mathcal{F}F_{ILS}(\kappa - f(\sigma_n)) * \mathcal{F}(e^{i\Phi_{\sigma_n}(\cdot,y)})(\kappa) + \\ &F_{ILS}(\kappa + f(\sigma_n)) * \mathcal{F}(e^{-i\Phi_{\sigma_n}(\cdot,y)})(\kappa)],\end{aligned} \tag{4.18}$$

which shows that each emission line is convolved with the Fourier transform of the respective positive and negative phase components.

Following Ben-David and Ifarraguerri (2002) and Englert et al. (2004), the phase Φ can be split in a linear and non-linear part denoted by

$$\Phi_{\sigma_n}(x,y) = 2\pi f(\sigma)\Delta x + \Phi_{\sigma_n}(x,y) \tag{4.19}$$

where $2\pi f(\sigma)\Delta x$ is the one-dimensional phase shift caused by a shift in the interferogram of Δx with respect to the ZOPD. The interferogram shift can be removed by exploiting the well-known shift theorem (Forman et al., 1966; Brault, 1987; Learner, 1995; Englert et al., 2004). Following Eq. (3.6) and the discussion thereafter, the linear phase component is eliminated when working with magnitudinal spectra, as it is the case in the presented retrieval processing in Sec. 3.4.1. However, if the ZOPD wants to be found, also this correction step needs to be applied. This is especially crucial for the processing method of split field of view in Sec. 5. The remaining non-linear phase, denoted by $\hat{\Phi}$, can be corrected following Englert et al. (2004). If $\hat{\Phi}$ is independent of the spectral variable, the interferogram in Eq (4.17) can be multiplied with $e^{-i\hat{\Phi}(x,y)}$. This corrects the positive frequencies, but induces twice the phase error onto the negative frequencies. If the phase varies only slowly over the spatial domain, the Fourier transform of the phase component is localized in the spectral domain. Therefore, the phase errors induced onto the negative frequencies have only little impact on the positive frequencies. The negative frequencies thus can be disregarded in the further processing. If however the phase Φ is dependent on frequency and space, $\mathcal{F}(e^{\pm i\hat{\Phi}(\cdot,y)})$ needs to be convolved with the ILS. The phase distortion is therefore included in the forward model, similar to the amplitude correction in Sec. 4.3.4.

The non-linear phase can be calculated from monochromatic calibration data following Englert et al. (2004), which is summarized as follows. By focusing on the modulated part of a monochromatic interferogram and applying a Fourier transformation, the positive frequency is isolated by employing a spectral bandpass filter. Applying the inverse Fourier transformation results in an interferogram consisting only of the positive frequencies denoted by

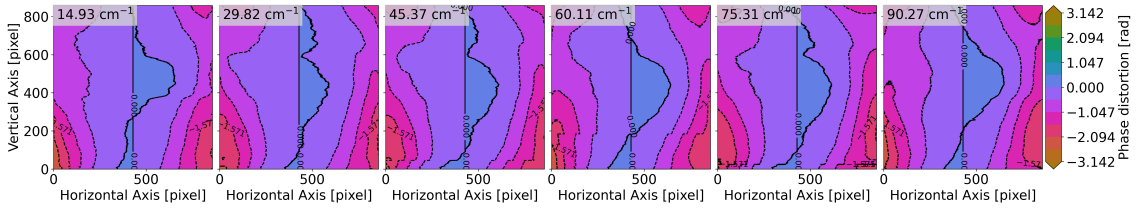

(a)

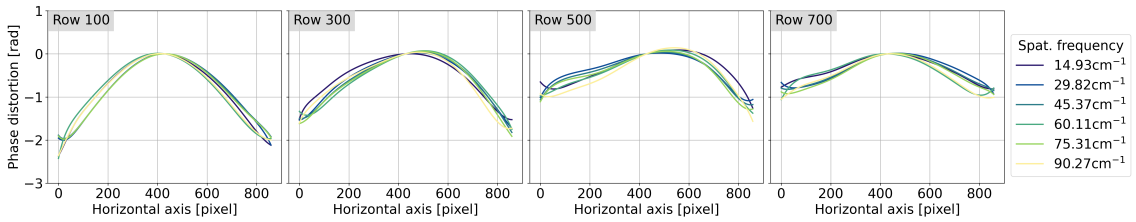

(b)

Figure 4.24: Estimated phase distortion for selected spatial frequencies; (a) 2D spatial variation, where spatial frequencies are given in the upper left corner of each subplot; (b) 1D spatial variation for selected rows, which are indicated in the upper left corner

$$I(x) = R_{\sigma_n} e^{i[2\pi f(\sigma_n)x + \Phi_{\sigma_n}(x)]} \tag{4.20}$$

where the expression is presented for only one row. The total phase can be calculated by

$$2\pi f(\sigma_n)x + \Phi_{\sigma_n}(x) = \arctan\left(\frac{\mathrm{Im}[I(x)]}{\mathrm{Re}[I(x)]}\right) \tag{4.21}$$

where Re and Im are the real and imaginary part of the interferogram. The non-linear phase function is obtained by subtracting $2\pi f(\sigma_n)x$ from the total phase. Applying this procedure for each row individually results in a 2D phase distortion field.

Following the same approach, the non-linear phase estimation derived from the monochromatic calibration data of the INSPIRESat4 mission are presented in Fig. 4.24 for various wavelengths. It shows a negative phase distortion towards the corners of the field-of-view, but only little variation along the spectral axis. This shows already that the image distortion correction worked well. Otherwise, an increasing phase distortion along the spectral axis would

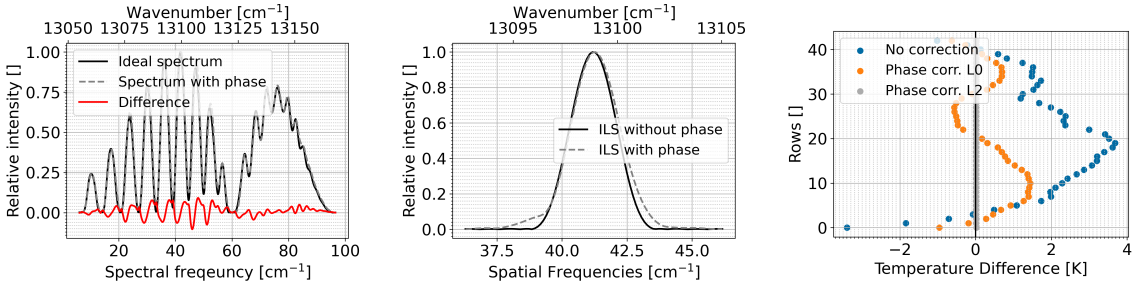

(a) (b) (c)

Figure 4.25: (a) Ideal spectrum in comparison to a spectrum including phase distortion; (b) ideal ILS compared to ILS including phase distortion; both (a) and (b) refer to row 20; (c) temperature retrievals for different processing modes with binning of 20 rows

be observed.

To test the influence of the phase distortion onto the temperature retrieval, an interferogram is simulated for a temperature of 200 K including the extracted phase distortion at each emission line employing Eq. (4.17). Subsequently, the two mentioned phase correction methods are applied and compared to a temperature retrieval without any correction. The first phase correction method assumes that the phase's dependency on frequency is small so that it can be neglected. In this case, the phase distortion can be corrected in the interferogram space and therefore is performed in the L0 processing. The second method considers the phase distortion of each emission line and incorporates it into the ILS. The results are shown in Fig. 4.25. Comparing an individual ILS in Fig. 4.25b shows that the phase distortion induces a slight shift towards higher frequencies. Furthermore, the lower flanks are distorted. When looking at the spectrum in Fig. 4.25a, the slight shift to higher frequencies can be also seen in the spectrum with phase distortion. Performing a temperature retrieval where a binning of 20 rows is applied shows that the phase distortion induces errors up to 4 K, if it is not corrected. Correcting the phase distortion in the L0 processing as explained above reduces the largest temperature error to 1.5 K. Only the second correction method, where the phase distortion is incorporated into each ILS, eliminates the error to less than 0.1 K.

To assess the sensitivity of the temperature retrieval to phase distortion, a similar study is conducted as for the baseline and amplitude variation in Sec. 4.3.4. Hereby, the phase is

disturbed by adding a sinusoidal perturbation defined by an amplitude and phase shift following Eq. (4.16). In the temperature retrieval, the phase is corrected in L2 processing, but incorporating the unperturbed phase in the ILS. This sensitivity study thus gives the requirements for the phase determination throughout calibration. This simulation is performed for different temperature levels to account for the varying sensitivity of the O_2 A-band emissions as discussed in Sec. 2.2. The results are shown in Fig. 4.26. Figure 4.26a shows that for increasing amplitude of the perturbation, the temperature error increases as well. The phase of the perturbation in Fig. 4.26b shows that if the perturbation is symmetric (phase of the perturbation equal to 0 and π), the induced temperature error is almost zero. However, if the phase perturbation is close to linear (phase of the perturbation equal to 0.5π and 1.5π), the temperature errors are large. This comes from the fact, that if the phase is symmetric, the convolution with the Fourier transform of $e^{-i\Phi}$ only distorts the side lobes of the ILS. However, if the phase is linear, the convolution with the Fourier transform of $e^{-i\Phi}$ results in a shifted ILS, inducing a shift in the emission lines in the retrieval and therefore larger errors in the minimization procedure of the retrieval entailing larger temperature errors. The analysis over different temperature levels in Fig. 4.26c aligns with the decreasing sensitivity of the O_2 A-band emissions at higher temperatures as shown in Sec. 4.2. In summary, this sensitivity analysis shows the necessity of estimating phase with a precision of 0.07 rad to achieve a temperature product within the accuracy range of less than 1 K when accounting for all temperature levels. This requirement could be relaxed if a greater temperature uncertainty is acceptable at higher altitudes. The current approach for estimating phase distortion is tested through simulation in Appendix A.13. The results indicate that the phase can be estimated with an accuracy of 0.1 rad across most of the field, which slightly exceeds the previously established requirement. Hence, it is anticipated that the current phase estimation method contributes significantly to the observed temperature errors.

In conclusion, the phase distortion influences the position and disturbs the side lobes of the individual ILSs. A spatially linear phase distortion induces a shift and a bell shaped phase distortion induces distorted side lobes. These two effects need to be corrected to obtain an accurate temperature estimate. Specifically in the current instrument, the phase distortion ex-

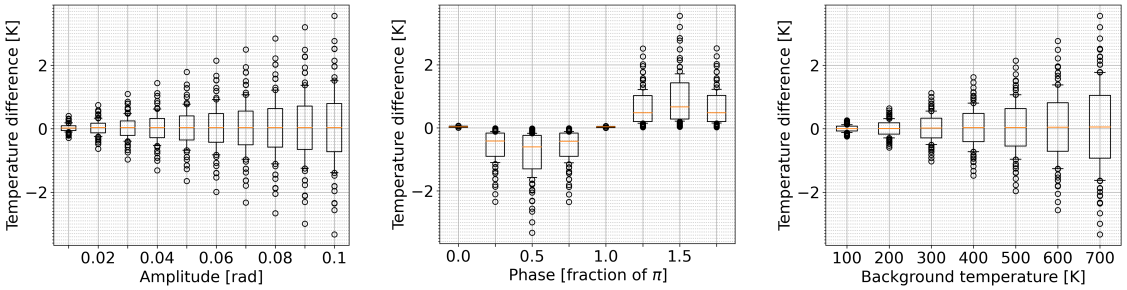

(a) (b) (c)

Figure 4.26: Sensitivity of temperature retrieval to spatial perturbations in the phase distortion; the additive perturbation is defined in Eq. (4.16); results are shown for different (a) amplitudes, (b) phases and (c) for different simulation temperatures; whisker of the boxplots show the 16th and 84th percentile corresponding to the standard deviation of a Gaussian distribution.

hibits a too large dependency onto frequency, so that the phase needs to be corrected within the L2 processing. This entails incorporating the phase distortion into the ILS for each emission line individually. The sensitivity study demonstrates that to maintain a temperature error within 1 K for tangent altitudes up to 140 km and temperatures up to 700 K, the phase must be determined with an accuracy of 0.07 rad. However, the current phase estimation method slightly surpasses this requirement. Hence, further research in this domain would prove beneficial. Furthermore, it is important to note that since the retrieval involves magnitudinal spectra, the spectrally linear phase component does not need to be considered, as it is eliminated by taking the absolute value of the spectrum.

4.3.6 Littrow calibration

The translation from frequency of the incoming light to the spatial frequency seen on the detector is defined in Eq. (3.3). It dependents on the magnification factor, the Littrow wavenumber and Littrow angle. While these parameters are initially determined during instrument design, their validation is essential through calibration data. It is crucial since these parameters influence the position of the emission lines, thereby impacting the entire spectrum's abscissa in the forward calculation of the retrieval.

The parameters can be derived from monochromatic calibration data, where the input

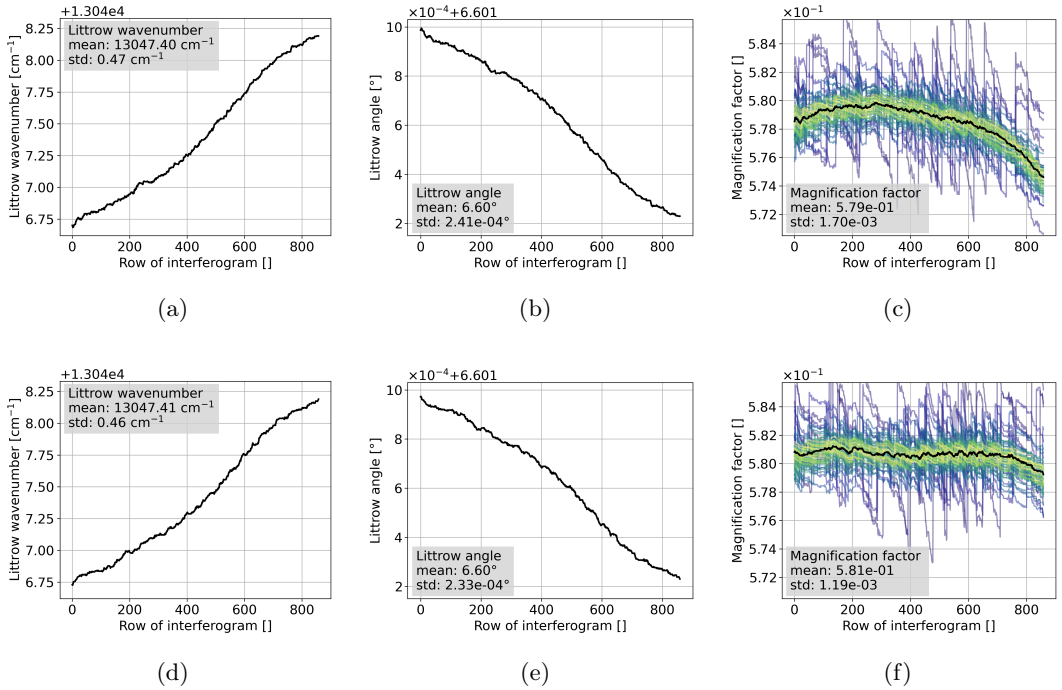

Figure 4.27: Results of Littrow calibration when using radial distortion parameters denoted in Tab. 4.3 for (a) Littrow angle, (b) Littrow wavenumber and (c) magnification factor of the camera optics; results of Littrow analysis when optimizing radial distortion parameters so that the magnification factor's variation is minimized for (d) Littrow angle, (e) Littrow wavenumber and (f) magnification factor of the camera optics; the magnification factor is evaluated on each spectral sample, where the dark and bright colors refer to low and high spatial frequencies, respectively.

frequency of the light source is given for each monochromatic image. The spatial frequency can be read out from the maximal value of the spectrum after applying the Fourier transformation to a monochromatic measurement. Repeating this procedure to multiple images corresponding to various wavenumbers provides a data set of spatial frequencies with corresponding input wavenumbers for each row. The Littrow wavenumber can be extracted by rearranging Eq. (3.3) denoted by

$$\sigma = \frac{1}{4\tan(\theta_L)M^{-1}} f(\sigma) - \sigma_L, \tag{4.22}$$

and applying liner regression over the $(\sigma, f(\sigma))$ data points, where the Littrow wavenumber is the intercept. The Littrow angle can be subsequently calculated by Eq. (3.2), which is

Table 4.5: Fine tuning of the radial distortion parameters via Littrow analysis, where the variation of the magnification factor is minimized

Parameter	Value
Fit parameter of division model k	$-1.14 \times 10^{-7}\,\mathrm{pixel}^{-2}$
Optical center x-axis	1004.9 pixel
Optical center y-axis	943.8 pixel

derived from the grating equation. Finally, the magnification factor can be estimated by again rearranging Eq. (4.22).

Performing this procedure for each row gives the results shown in Fig. 4.27(a)–(c). The extracted Littrow wavenumber shows an upward trend of about $1.5\,\mathrm{cm}^{-1}$ from the lowermost to the uppermost row. Translating that into Littrow angle space shows that the change in angle is very small in the magnitude of $10^{-4\circ}$. This small angle error could come from imperfect gratings or another source, which is not identified yet. However, it causes a noticeable shift in the Littrow wavenumber and therefore in the entire spectrum of the forward model, which needs to be accounted for by a varying Littrow wavenumber over the vertical axis. The Littrow wavenumber and angle are subsequently used to calculate the magnification factor of the camera optics. The magnification factors shown in Fig. 4.27c are evaluated on each monochromatic measurement, where the transition from dark to bright colors refers to increasing spatial frequencies. The results exhibit a bell-shaped decline as the rows increase. This can be attributed to an inaccurate extraction of radial distortion parameters from the grid target calibration measurements in Sec. 4.3.2. In fact, this curved pattern arises due to incorrect fit parameters within the division model, while the decline towards higher row numbers is influenced by erroneous optical center coordinates. To address this, an optimization was conducted on the radial distortion parameters, aiming to minimize the standard deviation of the derived magnification factors across all frequencies and rows. When repeating the analysis with the updated radial distortion parameters, the variability of the magnification factor across rows was noticeably reduced, as demonstrated in Fig. 4.27(f). This method can be considered a refinement of the radial distortion parameters. The refined parameters are

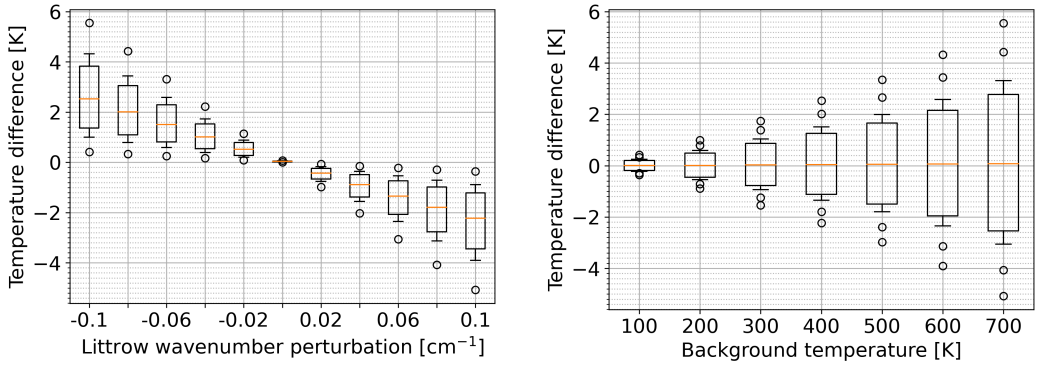

(a) (b)

Figure 4.28: Sensitivity of temperature retrieval to Littrow wavenumber variations; results are shown for different (a) perturbation in the Littrow wavenumber and (b) simulation temperatures; whisker of the boxplots show the 16th and 84th percentile corresponding to the standard deviation of a Gaussian distribution.

presented in Table 4.5.

In the final stage, a sensitivity analysis of the temperature retrieval is conducted, assessing the impact of a varying Littrow wavenumber for different temperature levels. The results are depicted in Fig. 4.28. Remarkably, even minor deviations of $0.1\,\mathrm{cm}^{-1}$ lead to substantial temperature errors, as illustrated in Fig. 4.28a. As anticipated, temperature errors increase at higher temperatures (Fig. 4.28b) due to the increased sensitivity of the temperature retrieval at higher temperatures, as discussed in Sec. 4.2. It is unlikely that the Littrow wavenumber can be determined with such an accuracy. Therefore, a more practical approach involves treating the Littrow wavenumber as a variable parameter within the optimization process. This gives the retrieval variability along the spectral axis.

4.4 End-to-End simulation based on monochromatic calibration data

This section consolidates all correction methods and undertakes an error analysis using actual calibration data. Hereby, monochromatic calibration measurements for frequencies lying close to the emission lines of the O_2 A-band are selected. It should be noted that the calibration is

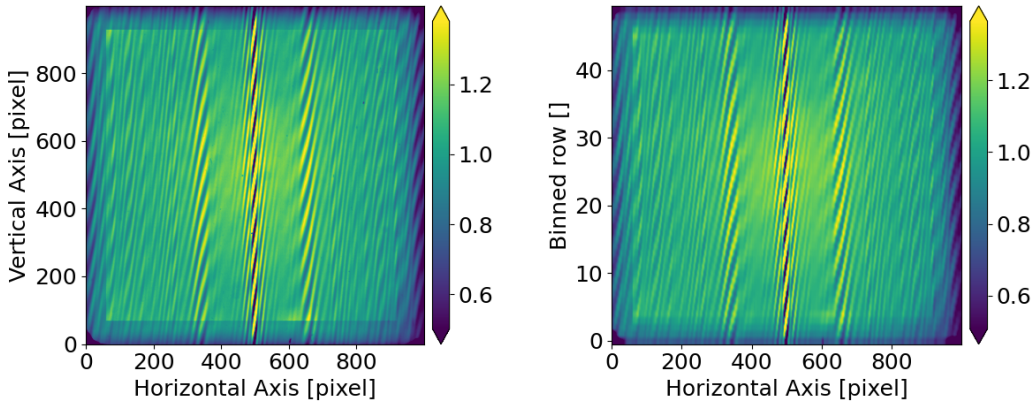

(a) (b)

Figure 4.29: (a) Simulated interferogram based on real monochromatic calibration measurements for constant temperature of 200 K, normalized by the 2D spatial mean; (b) interferogram from (a) where binning of 20 rows is applied

performed on an equidistant spectral grid, which does not always coincide with the frequencies of the emission lines. Subsequently, the rotational distribution of the emission lines using Eq. (2.10) is calculated with deviating wavenumbers assuming a constant temperature over the field of view. The selected monochromatic calibration data are subsequently scaled with the intensities of the rotational distribution and summed up. This process enables the simulation of an interferogram based on real calibration data incorporating all instrument errors at the calibration stage. The generated interferogram is shown in Fig. 4.29a, while the interferogram with binning of 20 rows, as performed in on-board processing, is displayed in Fig. 4.29b.

The subsequent step involves the preparation of the calibration data from the monochromatic measurements. The latter are corrected by background measurements, conducted during calibration to compensate for any unsought intensity sources in the laboratory environment. Thus, the monochromatic measurements and hence the derived interferogram are already corrected for fixed pattern and dark current, which are discussed in Sec. 4.3.1. In Section 4.3.3 it is shown that the phase variation close to the ZOPD, referred to as the Barber's pole, does not need specific treatment if apodization is applied and thus is omitted in this section. To ensure consistency with on-board interferogram processing, the monochromatic calibration measurements are also binned by 20 rows. The monochromatic calibration measurements are corrected

for radial image distortion with the method presented in Sec. 4.3.2 and the refined parameters in Tab. 4.5. Subsequently, the amplitude and phase are extracted following Sec. 4.3.4 and Sec. 4.3.5, respectively, which will be needed for the correct ILS implementation. Lastly, the Littrow wavenumbers and magnification factors for each row and emission line is extracted following Sec. 4.3.6, which defines the precise positions of the ILSs.

Moving to the processing of the binned interferogram displayed in Fig. 4.29b, the initial step involves estimating the baseline using a 2D Savitzky-Golay filter. Subsequently, this estimated baseline is subtracted to extract the modulated part of the interferogram. The radial image distortion is corrected with the method presented in Sec. 4.3.2 and the updated parameters in Tab. 4.5, mirroring the preparation of the calibration data. Next, apodization is applied where Norton-Beer strong is taken. The apodization function is defined in Sec. 3.2.4. The Fourier transformation is applied along the horizontal axis to transform the interferograms into spectra. The construction of the individual ILSs for each row and emission line incorporates the phase, amplitude, Littrow wavenumber, and magnification factor, all of which were extracted from the calibration data as explained in the previous paragraph. The spectra and ILSs serves as an input into the retrieval following Sec. 3.4.2, allowing to retrieve temperature for each row. It should be noted that the forward model evaluates the intensity distribution on the frequencies of the monochromatic measurements used for the interferogram generation. In the subsequent step regularization is applied where larger weights are assigned onto the first order derivative to smooth neighboring rows as explained in Appx. A.9.2. It should be noted that the forward model for homogeneous gas cells are used, as introduced in Sec. 3.4.2. The use of a forward model incorporating the radiative transfer equation, as applied in the actual retrieval processing detailed in Sec. 3.4.1, is not feasible here. This is due to the fact that the input frequencies derived from monochromatic measurements do not align with the emission lines of the O_2 A-band emission, as previously explained. Spectral interpolation of the monochromatic calibration data is not feasible, as the frequency of the fringe pattern changes with the frequency of the incoming light.

The results are shown in Fig. 4.30a. The retrieved temperature scatter with a standard deviation of $\pm 1\,\mathrm{K}$ for a gas cell simulation. Averaging over all rows reveals that the results

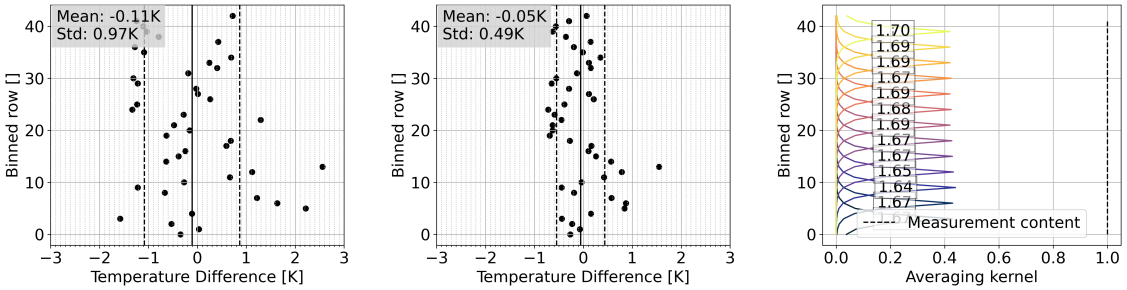

(a) (b) (c)

Figure 4.30: Temperature error of interferogram simulation base on monochromatic measurements and thus, including all instrument errors at the calibration stage, where a simulation is applied (a) without and (b) with regularization; the solid and dashed lines represent the mean and standard deviation over all rows; (c) averaging kernel of temperature retrieval with regularization; the FWHM of each averaging kernel is indicated by the displayed values measured in binned rows.

Table 4.7: Mean and standard deviation of temperature differences, calculated over rows analogous to the results presented in Fig. 4.30a, conducted for different temperature levels

Temperature level [K]	Mean [K]	Standard deviation [K]
100	0.07	0.38
200	-0.11	0.97
300	-0.23	1.68
400	-0.25	2.47
500	-0.20	3.41
600	-0.18	4.29
700	-0.23	5.16

show a small negative bias of 0.1 K. Applying regularization can mitigate the temperature error as displayed in Fig. 4.30b. However, this comes at a cost of vertical spatial resolution as shown by the increased FWHMs of the averaging kernels presented in Fig. 4.30c. The same end-to-end simulation is conducted for different temperature levels to account for the varying sensitivity of the retrieval to different temperature levels. To get an overall idea of the scattering of the temperature error, the mean and standard deviation over all rows are shown in Tab. 4.7. It shows that the standard deviation of the temperature error stays below 1.7 K for temperature levels below 300 K which are mainly present at altitudes below 110 km–120 K when looking at the temperatures of the HAMMONIA model runs in Fig. 4.1a. For higher

altitudes, the standard deviation is increased up to 5 K at 700 K, corresponding to altitudes at 140 km during solar maximum conditions in the HAMMONIA model runs. It should be noted that the largest errors occur mostly at the same rows for all analyzed temperature levels, like at row 5 or 13 (compare to Fig. 4.30a). This indicates that localized errors are present, which have not been captured and corrected yet. It is expected that further in-depth analysis will decrease the temperature error further.

4.5 Chapter summary

This chapter comprehensively evaluates the instrument's overall performance. It starts with radiative transfer calculations, which simulates the expected radiances arriving at the instrument's aperture. These calculations are used for the performance assessment of an ideal instrument, serving as a benchmark for the potential of the presented observational method. Subsequently, it discusses errors stemming from instrument imperfections. This includes a detailed presentation of their mathematical characteristics and the corresponding correction methodologies. To further enhance the understanding, a sensitivity analysis of these errors is conducted, along with an assessment of the effectiveness of the correction methods in relation to the accuracy of retrieved temperatures. Building upon these findings, the chapter concludes with an end-to-end simulation based on actual calibration measurements, which includes all errors. This final simulation serves the purpose of establishing a realistic error assessment for the current processing state.

In terms of radiative transfer calculations, as discussed in Section 2.1, emission stems from three sources, all active during the day but reduced to one source at night. This leads to a noticeable decrease in radiance during nighttime simulations, about one order of magnitude lower compared to daytime conditions. Extending integration time helps to compensate for this, but nighttime observations encounter limitations below 85 km and above 105 km due to low signal strength. Similarly, daytime measurements face constraints above 120km, which could be mitigated with higher temperature uncertainties. Self-absorption affects observations below 85 km, reducing information content. Comparing model simulations with satellite ob-

servations shows good agreement during day- and nighttime conditions, which highlights the model's effectiveness to estimate the signal strength arriving at the instrument.

The analysis of the ideal instrument's performance reveals that the temperature precision of the observational method diminishes as temperatures rise due to reduced sensitivity to O_2 A-band emissions. Trivially, precision increases with higher signal-to-noise ratios (SNRs). A comprehensive end-to-end simulation is conducted, involving the generation of interferograms through the radiative transfer model described in Chap. 2, followed by temperature retrievals as outlined in Sec. 3.4.1. Results from this simulation demonstrate that, in daytime scenarios, the overall temperature precision takes on an concave shape. Optimal precision of 1 K to 1.5 K is achieved at a tangent altitude of 100 km. Precision decreases to 4 K to 5 K for a tangent altitude at 60 km due to pronounced self-absorption effects. At higher tangent altitudes, around 140 km, precision diminishes to 6 K, attributed to elevated temperatures and reduced signal strength, consequently leading to a decreased SNR. For the nighttime simulations, temperatures in the altitude range of 85 km to 105 km are resolvable. This arises from signal generation exclusively by the Barth process, confined to this altitude interval. For the upper tangent altitudes above 93 km, a temperature precision of about 1 K can be attained. Below this threshold, precision decreases to 3 K to 4 K at 85 km, impacted by self-absorption effects and rapidly declining signal strength. It is important to note that these simulations utilized vertical binning of 20 rows and integration times of 1 s and 10 s for day- and nighttime simulations, respectively. Enhancing signal strength can be achieved by increasing vertical binning at the cost of vertical resolution or by extending integration times at the expense of along-track sampling, ultimately leading to improved temperature precision.

Subsequently, errors induced by an imperfect instrument are investigated. For each error, a sensitivity analysis is conducted to determine its impact on the retrieved temperature. Additionally, corresponding correction methods including their efficacy are presented. The main points are summarized as follows.

Firstly, radial distortion is discussed, which can be determined from grid target measurements and fitting the presented division model. A simulation with temperature level of 200 K, incorporating radial image distortion, showed that uncorrected distortions introduce temper-

ature errors of up to 6 K. However, these errors can be considerably reduced to below 0.1 K, if the presented correction method is applied. The radial distortion correction depends of a fitting parameter for the applied division model and the accurate determination of the optical center. A sensitivity analysis showed that the temperature retrieval is very sensitive to the fitting parameter and the y-coordinate of the optical center, thereby emphasizing the critical need for precise extraction of these two parameters.

Subsequently, the influence of imperfect grating alignment is addressed, which leads to a phase variation dependent on the vertical axis. The misalignment angle can be estimated from the rotation angle of the fringe pattern of monochromatic measurements. Analytically, perfect correction for the error is not feasible. Still, the proposed correction method can produce a recovered interferogram with straight fringe patterns, particularly valuable when estimating the interferogram center. The impact onto the temperature retrieval is small and the retrieved temperature error is bounded. Apodization helps to decrease this bound to an acceptable level, and therefore, this error does not need to be considered in the usual processing.

Moreover, calibration measurements show decreasing intensity and contrast of the measured wave pattern toward the periphery of the image, mainly induced by the optical system. A method is presented to extract these two measures. Simulations including intensity and contrast variations demonstrate that the temperature retrieval is sensitive to the contrast variation. Correcting for the contrast variation results in a temperature product with errors of less than 0.1 K. Conversely, the retrieval remains insensitive to intensity variation, as it primarily impacts low frequencies excluded from the retrieval process. However, obtaining an accurate intensity estimate remains crucial for an reliable contrast estimate.

Furthermore, the instrument induces a phase variation, which can be extracted from monochromatic measurements as well. Simulations incorporating resulting phase distortion underscore the sensitivity of retrieval accuracy to this variation, necessitating correction. The presented correction method exhibits good performance, nearly eliminating all temperature errors related to phase distortion. However, estimation of phase from monochromatic measurements remains the limiting factor in this context.

Lastly, the Littrow wavenumber and magnification factor of the camera optics is cali-

brated. The study demonstrates the retrieval's high sensitivity to the precise determination of the correct Littrow wavenumber. This observation aligns with intuition, as an inaccurate Littrow wavenumber causes a significant shift in the entire fitted spectrum. Therefore, it is recommended to treat the Littrow wavenumber as a variable parameter within the optimization process of the retrieval.

In the final step, end-to-end simulations based on real monochromatic measurements are performed for different temperature levels. These simulations include all instrument errors at the calibration stage and incorporate all previously introduced correction methods. The simulations reveal that the standard deviation of the temperature errors remains below 1.7 K for temperature levels below 300 K, referring to altitudes below 110 km–120 K. At higher temperatures of 700 K, corresponding to altitudes around 140 km during solar maximum conditions, the standard deviation increases to 5 K. It is important to note that the most significant errors tend to cluster around the same rows across all analyzed temperature levels, suggesting the presence of localized errors. These specific errors have not been addressed in this study and will require identification and correction in future research.

The analyses in this chapter demonstrate that the processing chain approaches a temperature uncertainty of 1 K within the mesopause region. The predominant error stems from the limitations in phase estimation performance. By delving deeper into the examination of localized errors and enhancing phase estimation techniques, it is expected that further reduction in temperature errors can be achieved.

Chapter 5

Split field of view to resolve horizontal temperature variations

This chapter delves into the potential of the instrument to resolve horizontal temperature variations and follows mainly Ntokas et al. (2023a). This ability stems from the instrument's capacity to maintain the spatial distribution of the atmospheric scene throughout its optical system. Revisiting Fig. 3.1, the front optics map the captured atmospheric scene onto the gratings, while the subsequent camera optics further map the image from the gratings onto the detector. As described in Sec. 3.1, the spectral information is contained on the x-axis due to constructive and destructive interference induced by the gratings. The 2D interferogram therefore contains spatial information on the vertical (y-axis) and superimposed spectral and spatial information on the horizontal axis (x-axis). The idea is to split the interferogram at zero optical path difference (ZOPD), utilizing each half individually. The spectral information is fully contained in one half since the interferogram is symmetric around the ZOPD by definition. Mirroring each side around the ZOPD gives a full interferogram for each side which can be employed to derive two independent temperatures along the horizontal axis. Each interferogram then contains temperature information of the associated side of the field of view, resulting in two 1D temperature profiles derived from one image. This can be subsequently used in a wave analysis to derive some 3D information on wave parameters, as it is shown in a simulation study by Chen et al. (2022) for the presented instrument. The concept to mirror

the interferogram at the ZOPD has already been used by Johnson et al. (1996) for the far-infrared spectrometer (FIRS)-2 and by Gisi et al. (2012) for the TCCON FTIR spectrometer to gain a higher spectral resolution by increasing the length of the interferogram and therefore decreasing the FWHM of the ILS. Here, this processing approach is used to gain some insight into the horizontal temperature variation.

This chapter is organized as follows: First, the methodology is explained using simple examples and the noise propagation is analyzed in Sec. 5.1. Subsequently, Section 5.2 investigates the sensitivity of the temperature retrieval with respect to the temperature variation in horizontal direction. Further exploration involves discussions on the locations of retrieved temperatures when utilizing half interferograms for simulated horizontal temperature variations typically caused by gravity waves in Sec. 5.3. The effect of apodization onto the retrieval using half interferograms is assessed in Sec. 5.4. Lastly, the methodology and a concise simulation example is given for a split field of view in three segments in Sec. 5.5.

5.1 Methodology and noise error analysis

This section outlines the split field of view processing methodology and evaluates the propagation of shot noise within this approach. Employing a line-by-line model, a 1D interferogram resulting from a horizontal temperature variation is defined by

$$I(x) = \sum_{n=N}^{I} R_{\sigma_n}(x) \left[1 + \cos(2\pi f(\sigma_n)x)\right], \tag{5.1}$$

which is similar to the general interferogram equation given in Eq. (3.4), but $R_{\sigma_n}(x)$ is dependent on the horizontal spatial variable to account for the radiance variation across the horizontal field of view. After generating the interferogram, it is split at the ZOPD, and subsequently, each side is mirrored symmetrically around the ZOPD, exploiting the interferogram's inherent symmetry. This results in two interferograms of equal length as using the full interferogram, which entails the same spectral resolution. When using the full interferogram, one half of the shot noise propagates into the real and the other half into the imaginary part of the spectrum, as discussed in Appx. A.8. Mirroring the interferogram however causes the shot

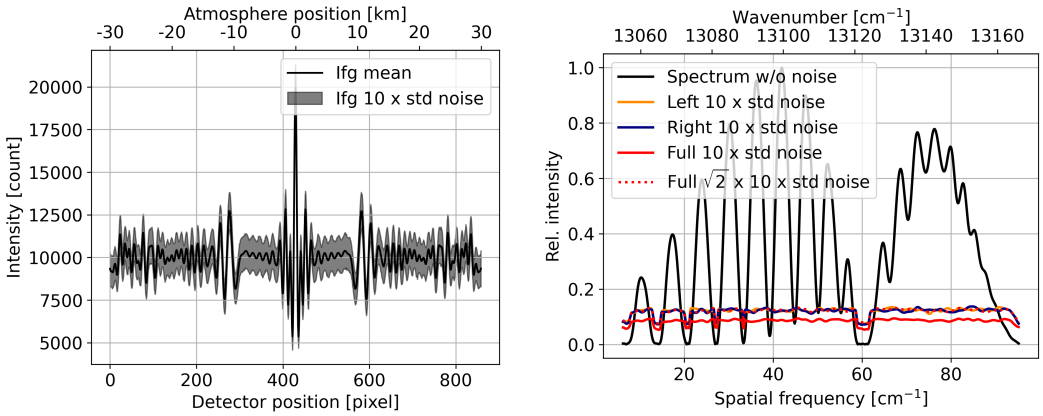

(a) (b)

Figure 5.1: Results of Monte-Carlo simulations with 300 samples where shot noise is propagated into the spectrum for an interferogram with a constant temperature of 200K; (a) mean and 10 × the standard deviation of the 300 interferogram samples; (b) spectrum without noise as a reference; 10 × the standard deviation of the spectral noise using full interferograms and left- and right-side of the interferograms; standard deviation of the noise using the full interferograms multiplied by a factor of $\sqrt{2}$ is shown as red dotted line; Norton-Beer strong apodization is applied.

noise to be symmetric, so that it is then fully propagated into the real part of the spectrum, resulting in a higher noise level by a factor of $\sqrt{2}$.

To show this numerically, a Monte-Carlo simulation with 300 samples is performed, where an interferogram is simulated using Eq. (5.1) for a constant temperature of 200 K across the horizontal field of view. The signal level is set to a signal-to-noise ratios (SNR) of 100 (equivalent to an interferogram's mean intensity of 10 000), which results in a temperature precision of approximately 1 K. Figure 5.1a shows the mean and the standard deviation of the interferogram samples including shot noise following Sec. 3.3. In the following step, the interferograms are split at the ZOPD and mirrored. The spectra are shown in Fig. 5.1b after individual Fourier transformation is applied. As a reference, the spectrum without noise is shown. Further, the standard deviation of the noise of the 300 samples are shown for the case using the full interferogram and the two cases using mirrored single-sided interferograms. As stated before, the noise level is increased by a factor of $\sqrt{2}$ for the mirrored single-sided interferograms compared to the full interferogram. Subsequently, the temperature is retrieved following the retrieval method of a homogeneous gas cell explained in Sec. 3.4.2 for each

Monte-Carlo sample. All three methods result in a temperature accuracy of less than 0.1 K. Using the full interferogram results in an expected temperature precision of 1 K. Using the left- and right-side of the interferograms however, results in a decreased temperature precision of 1.4 K. Note that normally the noise is evenly distributed in the spectrum. If the signal however is close to zero, the noisy signal can take positive and negative values. Considering only magnitudinal spectra, the negative values are mirrored, resulting in a smaller standard deviation. More discussion on this is given in Appx. A.8.

Conducting an analogous analysis for various SNRs and temperature levels, similar to the approach undertaken for the full interferogram in Sec. 4.2, provides the temperature precision associated with the right single-sided interferograms, as illustrated in Fig. 5.2a. The difference between the temperature precision using the right single-sided interferogram and using the full interferogram scaled by a factor of $\sqrt{2}$ is shown in Fig. 5.2b. It reveals a consistent trend across a range of temperature and SNR levels, indicating that the temperature precision is diminished by a factor of $\sqrt{2}$ when using the right single-sided interferogram. The same simulation has been performed for the left single-sided interferogram and showed a similar result. Thus, it can be concluded that the increase of spectral noise by a factor of $\sqrt{2}$ results in a reduction in temperature precision by the same factor.

To study the ability to retrieve horizontal temperature gradient information from a single interferogram, a simple example is presented first. A linear temperature gradient of 20 K over the horizontal field of view of 60 km, shown in Fig. 5.3a, is incorporated into the interferogram by using Eq. (5.1). Figure 4.4b shows that for higher temperatures the integrated intensity within the bandpass filter decreases since the distribution of the emission lines becomes flatter, as observed in Fig. 4.4. Following Eq. (5.1), the interferogram is just the sum of cosine waves with amplitude and offset equal to the intensity of the emission lines. The interferogram's baseline therefore also shows a decrease with higher temperatures, as shown in Figure 5.3b, aligning with the variation of the integrated intensity within the bandpass filter.

To perform a statistical analysis, a Monte-Carlo simulation with 300 samples is performed, where shot noise is considered in the interferogram space. After the interferogram is split and mirrored, a spectrum and a corresponding temperature is obtained for each sample. Note

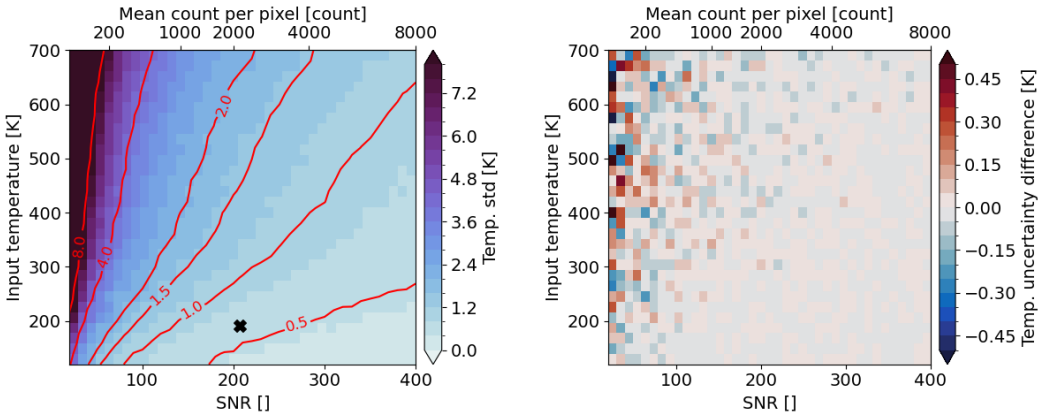

(a) (b)

Figure 5.2: (a) Temperature precision of using the right single-sided interferograms assessed for different SNRs and temperatures; (b) difference of temperature precision using the right single-sided interferograms and temperature precision of full interferogram in Fig. 4.5b multiplied by $\sqrt{2}$

that the temperature gradient results in a tilted non-modulated part which is fitted and subtracted before splitting the interferogram. Figure 5.3c shows the mean of all noisy spectra with constant temperature at 200 K as a reference. Furthermore, the smoothed mean difference of the noisy spectra incorporating the linear temperature gradient with respect to the reference spectrum is shown. Using the full interferogram, the mean difference shows only little differences across the spectral axis, which shows that the spectrum contains an averaged temperature information of the given temperatures within the field of view. In fact, the Fourier transformation maps a weighted sum of all spatial samples in the interferogram to a sample in the spectrum. Thus, the temperature information is localized in the interferogram, but fully distributed across the spectrum. The retrieved temperature is therefore an average of the temperature information within a given region of interest in the interferogram.

Using only the left side of the interferogram entails that the interferogram contains only temperatures from 190 K to 200 K. As explained in Sec. 2.2, lower temperatures means higher intensities in the central spectral region and lower intensities at the edges of the bandpass filter, which fits to the simulation results. Analogously, the same argumentation can be applied to the right side of the interferogram. The mean and standard deviation of the retrieved

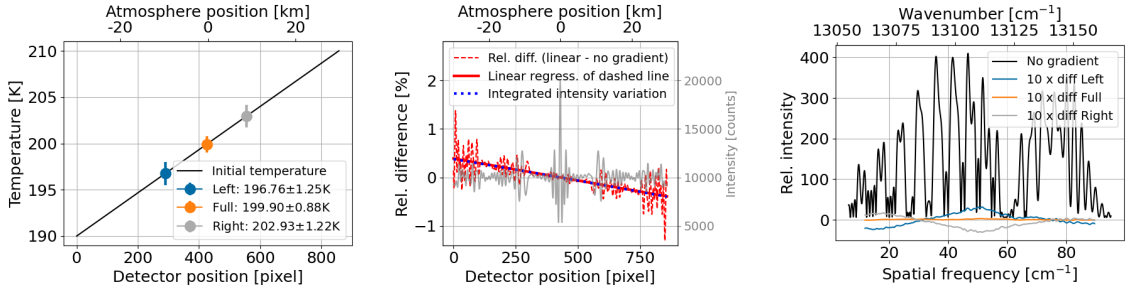

(a) (b) (c)

Figure 5.3: Results of Monte-Carlo simulations with 300 samples where shot noise is propagated through the spectrum into the temperature retrieval for an interferogram with linear temperature gradient from 190K to 210K; (a) used temperature gradient and retrieved temperatures; (b) interferogram with constant temperature at 200K and a mean signal level of 10 000 (gray line, right y-axis); difference between interferogram with temperature gradient from (a) and reference interferogram relative to the value 10 000 (mean of interferogram without temperature gradient) including its linear regression (red lines, left y-axis); integrated intensity variation within the bandpass filter due to the temperature gradient relative to the intensity corresponding to the central temperature of 200K (blue line, left y-axis); (c) mean of noisy spectra with constant temperature at 200 K as reference; mean difference between the noisy spectra incorporating the linear temperature gradient and the reference, when using full or half-sided interferograms; no apodization is applied.

temperatures are shown in Figure 5.3a. The precision of the temperature retrieval is again decreased by $0.3\,\mathrm{K}-0.4\,\mathrm{K}$. Thus, the decrease in the temperature precision mainly comes from the mirrored shot noise. The retrieved temperatures of the single-sided interferograms lie on average 6 K apart of each other, which is smaller than the mean temperature of each side suggests (10 K). This origins from the interferogram's large intensity variations around the ZOPD contributing more to the spectrum due to the Fourier transformation acting like a weighted sum. Consequently, these deviations carry a greater amount of temperature information within the spectrum. Eq. (5.1) shows that the large variations comes from the fact that the interferogram consists of superimposed cosine waves with zero phase at ZOPD. This is the reason why no apodization is applied which applies higher weights to the central region of the interferogram. This will be discussed more in detail in Sec. 5.4.

It is important to acknowledge that the accuracy of the split field of view processing method relies on accurate knowledge of the ZOPD location, as pointed out by Ben-David and Ifarraguerri (2002) and Brault (1987). A sensitivity study to assess the impact of the

ZOPD location was conducted for this instrument by Ntokas et al. (2022), which concluded that precise knowledge of the ZOPD on a sub-pixel scale is necessary to achieve the desired temperature accuracy and precision. Mirroring around the false ZOPD position increases all frequencies inherent in the interferogram on one side while decreases them on the other side. Failure to account for this phenomenon during processing leads to inaccuracies in the temperature estimates. To accurately determine the ZOPD, correction techniques can be employed, which have already been applied to real-world data by Kleinert et al. (2014) and Ungermann et al. (2022) for imaging Michelson interferometers. These methods effectively compensate for the interferogram shift by subtracting the linear phase from the spectrum. Furthermore, the barber's pole variation also needs to be corrected following Sec. 4.3.3 to accurately find the ZOPD. Other extracted calibration data used in the instrument line shape (ILS) like the amplitude and phase need to be split and mirrored as well.

5.2 Sensitivity to horizontal temperature variations

In this section the sensitivity of the temperature retrieval to horizontal temperature variations is assessed. Hereby, a scalar function is defined denoted by

$$g : \boldsymbol{T} \mapsto T_{ret} \tag{5.2}$$

which maps the horizontal temperature variation $\boldsymbol{T}$ to a retrieved average temperature T_{ret}. The derivative of g with respect to $\boldsymbol{T}$ is approximated by finite differences. Since the emission has different sensitivities at different background temperatures, as shown in Fig. 4.4b, the derivatives are calculated for a range of encountered temperatures in Fig. 4.1a. The result is shown in Figure 5.4a. It shows an overall wavy pattern representing changing intensities of emission lines and its modulation through the instrument. The matrix shows that for any temperature level, the retrieved temperature is most sensitive to temperatures close to the main lobe. Figure 5.4b shows smoothed rows for selected temperature levels of the matrix in Fig. 5.4a. Lower temperatures below 300 K show a lower sensitivity around the main lobe and more sensitivity to the side. Temperature levels around 500 K have the highest central

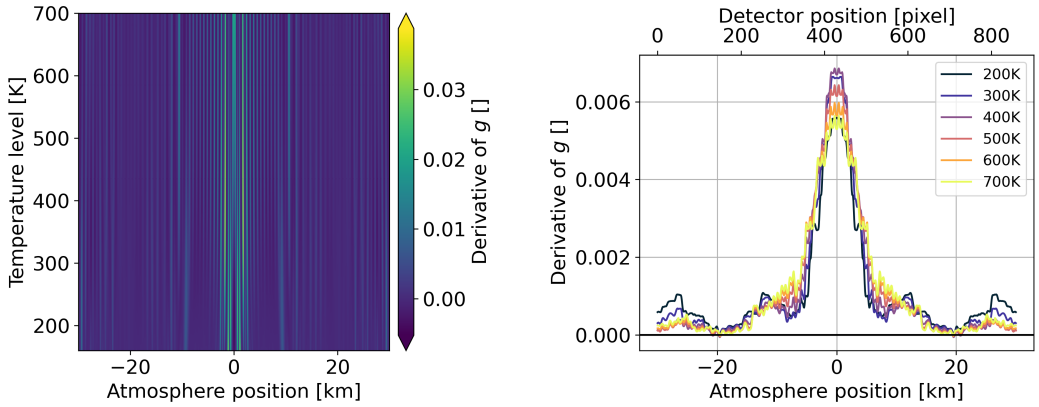

(a) (b)

Figure 5.4: (a) Derivative of the scalar function g defined in Eq. (5.2) at a given horizontal position evaluated for multiple temperature levels; (b) Selected rows of (a) and smoothed by a running mean with window size 101 pixels

peak and the lowest sides. This effect is attenuated for temperatures above 500 K. Thus, the temperature retrieval is least sensitive to horizontal temperature variations around 500 K.

The Jacobian matrix in Figure 5.4a can be used in Taylor's theorem to linearly approximate function g defined in Eq. (5.2). Hereby, the 2D field is interpolated thus, deriving the continuous derivative with respect to temperature variation. The temperature variation is split into background and residuals, denoted by $\boldsymbol{T} = \bar{T} + \boldsymbol{T'}$. The retrieved temperature can be then estimated due to Taylor's theorem by

$$\tilde{T}_{ret} = \left(\nabla g(\bar{T}) \cdot \boldsymbol{T'}\right) + \bar{T}, \tag{5.3}$$

where $\cdot$ denotes the scalar product of two vectors.

To evaluate this approximation, the simulated temperature variations from Sec. 5.3 are used. The estimated retrieved temperatures using the Jacobian matrix in Fig. 5.4a and Taylor's theorem in Eq. (5.3) are compared to the retrieved temperature running through the temperature retrieval of a homogeneous gas cell explained in Sec. 3.4.2. The results are shown in Fig. 5.5, which shows an overall good agreement with 98 % being within an error of less than 0.05 K. A slight but negligible bias of 0.02 K can be seen. The minimal and maximal

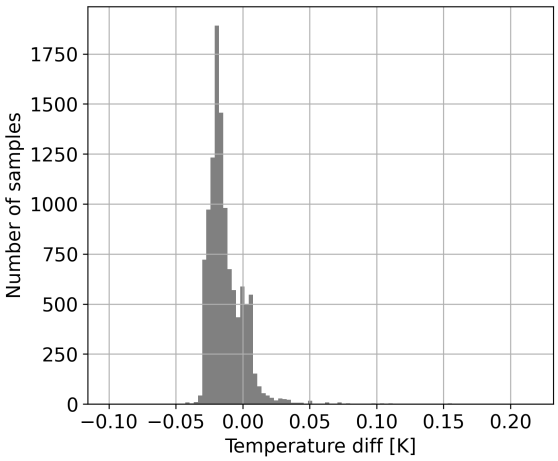

Figure 5.5: Temperature error using derivative matrix from Figure 5.4a and Eq. (5.3) to estimate retrieved temperature

error are at $-0.10\,\mathrm{K}$ and $0.28\,\mathrm{K}$, respectively. Thus, the explained method can be used to approximate the retrieved temperature for varying horizontal temperature variations without running through a full end-to-end simulation.

5.3 Retrieval results of split field of view processing

To get a comprehensive picture of the split interferogram processing method, interferograms are simulated which incorporate temperature variations typically produced by gravity waves. Subsequently, the interferogram is split at the ZOPD and the temperature is retrieved for each side. When observing temperature variations produced by an atmospheric wave, it is essential to localize that information in space to obtain proper wave characteristics from that data. To this end, sinusoidal horizontal temperature variation are simulated by

$$h(x, \bar{T}) = \bar{T} + A_h \cos\left(2\pi \frac{x}{\lambda_h} + \phi_h\right) \tag{5.4}$$

where $\bar{T}$ is the background temperature, A_h the amplitude, λ_h the horizontal wavelength, ϕ_h the phase and x is the horizontal scale. The horizontal field of view is assumed to be $\pm 30\,\mathrm{km}$. Following Fig. 4.1a, background temperatures from $160\,\mathrm{K}$ to $700\,\mathrm{K}$ are modeled. Following Chen et al. (2022), the horizontal wavelength is altered from $200\,\mathrm{km}$ to $2000\,\mathrm{km}$

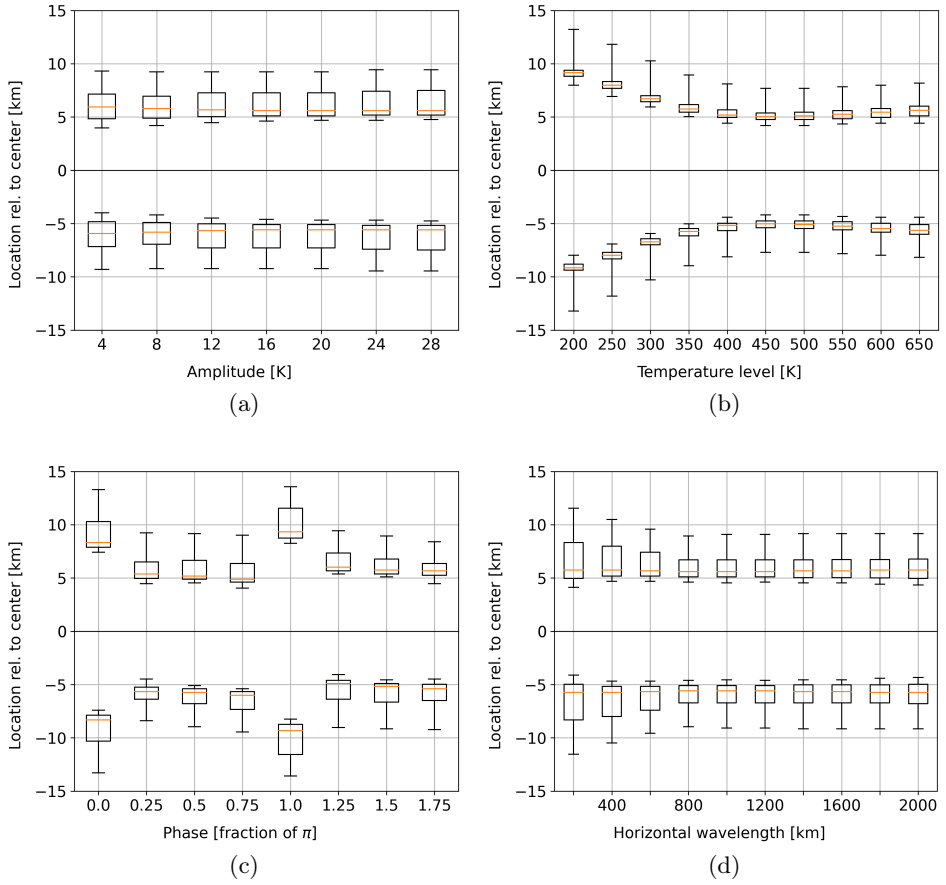

Figure 5.6: Relative location of the retrieved temperatures within the temperature variation using single sided interferograms (a) for varying amplitude, (b) for varying temperature background level, (c) for varying phase and (d) for varying horizontal wavelength; the box extends from the lower to upper quartile values, the whiskers extend from the 5th to 95th percentile.

and the amplitude from 4 K to 30 K. In total, 4220 simulated temperature variations are analysed. It should be noted that temperature variations with a min-max value smaller than 1 K are excluded, because they cannot be resolved due to the aimed instrument's temperature precision. For the further analysis the term 'location' of a retrieved temperature is introduced. This is defined by the abscissa of the atmospheric model temperature, which is equal to the retrieved one.

The location of the retrieved temperatures of each side relative to the center are shown in Figure 5.6. Hereby, one parameter is varied while showing the distribution of all waves for the remaining parameters. Note that the distance between the locations of each side can be seen

as a measure for how well the presence of a horizontal temperature variation can be characterized. Figure 5.6a shows no influence of the amplitude of the temperature residual onto the location of the retrieved temperatures. Figure 5.6b shows that the temperature background affects the distance of the retrieved temperatures due to the different sensitivities of the O_2 A-band emission with respect to temperatures. The results in Sec. 5.2 explain that interferograms of lower temperatures carry a higher information content at the sides compared to that of higher temperatures and thus, resulting in retrieved temperatures laying further apart of each other when using single-sided interferograms. The minimum of this effect is around 500 K with a slight increase for temperatures above. When looking at the phase in Figure 5.6c, $\phi = 0$ and $\phi = \pi$ are outliers referring to the crest and trough of the captured temperature residual. In both cases, the temperature variation is low within the center and large at the edges. This counteracts the increased temperature information around the center and results in temperatures being further apart from each other. The horizontal wavelength of the temperature variation affects only slightly the distance of the retrieved temperature as shown in Figure 5.6d. Short wavelengths results in a larger spread of the location distribution due to the fact that the phase of the temperature variation plays a greater role. To conclude, if one takes the background temperature into account one can give a good estimate of the location of the retrieved temperature. The effect of the phase will introduce a systematic error at the crest and trough. Compensating these two effects in the wave analysis, one gets a good estimate of the horizontal wave parameter components.

5.4 Effect of apodization onto split field of view processing

In this section the influence of apodization onto the retrieval of split interferograms is assessed. This is evaluated for horizontally linear temperature gradients with a spread of ± 10 K for central temperature levels from 160 K to 700 K and for the Norton-Beer apodization functions introduced in Sec. 3.2.4. The results are shown in Fig. 5.7. Using the full interferogram, the mean temperature can be recovered for each temperature level independent of the strength of the apodization. Using a single-sided interferogram, stronger apodization decreases the

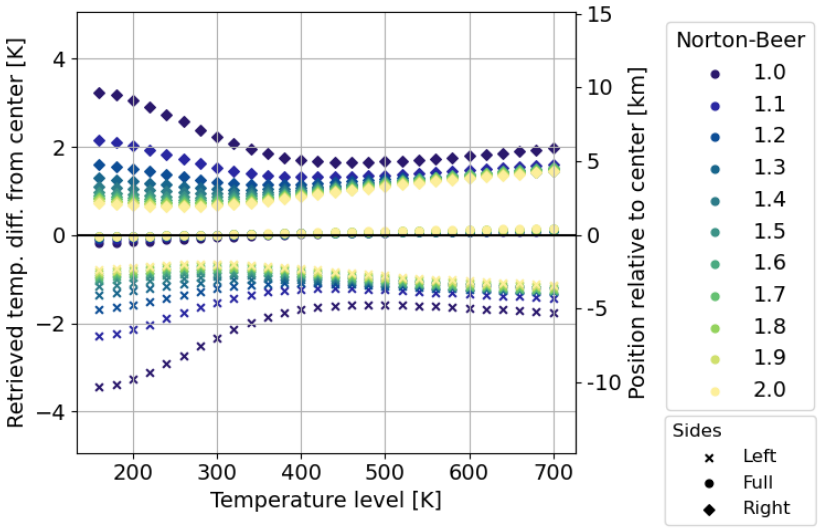

Figure 5.7: Retrieved temperatures using a linear temperature gradient for multiple temperature levels and different strengths of apodization

localization difference between the retrieved temperatures of the left and right side. Revisiting Fig. 3.3a, the apodization functions decreases the intensity of the interferogram towards the edges and thus put a greater weight on the information content in the central region. The effect that the retrieved temperatures are closer to the center as explained in Sec. 5.1 is consequently amplified by the apodization function. The case without apodization (Norton-Beer 1.0) shows a decrease in the temperature difference between the two sides for temperature levels between 160 K and 500 K and a slight increase for higher temperatures. This shape is consistent with the results shown in Fig. 5.6b. The cases with apodization follow similar shapes.

To conclude, when using mirrored single-sided interferograms, apodization is not only a trade off between spectral resolution and decrease of the side lobes, but also a trade off between spatial resolution of the two retrieved horizontal temperature data points and robustness against errors (see Sec. 3.2.4 for link between apodization and robustness and Sec. 4.3.3 for an example where apodization helps to mitigate instrument errors). Using single-sided interferograms therefore increases the requirements for instrument error mitigation, if the distance between the two retrieved temperature data points wants to be kept large.

5.5 Multiple split field of view

This section shows the theoretical framework of splitting the field of view into multiple parts, enhancing the horizontal resolution of the retrieved temperature product. Subsequently, this theoretical concept is applied to split the interferogram into three parts, each enabling a derivation of a distinct temperature value. This section serves as a proof of concept associated with employing a multi-split field of view approach, albeit it is essential to acknowledge that the feasibility of this approach in a real-world application remains subject to further research.

The concept of utilizing only a segment of the interferogram aligns with the general concept of the ILS outlined in Sec. 3.2.2. This can be mathematically expressed as the product of an infinite interferogram multiplied with a shifted boxcar function, denoted by

$$I(x) = \Pi(x)\tilde{I}(x) \tag{5.5}$$

where $\tilde{I}$ refers to the infinite interferogram and Π is the shifted boxcar denoted by

$$\Pi(x) = \begin{cases} 1 & \text{if } x \in [l_1, l_2] \\ 0 & \text{else} \end{cases} \tag{5.6}$$

where l_1 and l_2 are the bounds of the considered area of the split field of view along the horizontal axis. The Fourier transform of this shifted boxcar defines the ILS required for the forward calculation in the retrieval process, which is denoted by

$$F_{ILS}(\kappa) = \frac{1}{-i2\pi\kappa}\left(e^{-i2\pi\kappa l_2} - e^{-i2\pi\kappa l_1}\right). \tag{5.7}$$

Employing this complex ILS in the forward calculation, theoretically allows to perform a temperature retrieval on any section of the interferogram. It should be noted that this allow a retrieval without apodization. The complex ILS in Eq. (5.7) exchanges the sinc function, which defines as ILS in the processing of a symmetric interferogram, as introduced in Sec. 3.2.2. In a real world application, the boundaries of the selected segment, denoted here by $l1$ and $l2$,

needs to be defined accurately, similar to the previous requirement for knowing the ZOPD to split the interferogram at its center in Sec. 5.1.

To illustrate this theoretical framework, an interferogram including a linear temperature gradient ranging from 190K to 210K is simulated. The mean value of the interferogram is set at 10 000 counts, corresponding to a temperature precision of 1 K for a retrieval using the full interferogram, as elaborated in Sec. 5.1. Subsequently, the interferogram is split into three segments. The outcomes are presented in Fig. 5.8. The interferogram without noise, is depicted in Fig. 5.8b, showcasing the splitting positions. The spectra resulting from the Fourier transformation are displayed in Fig. 5.8c. The spectrum derived from the central interferogram segment exhibits a similar shape as the spectra of the split and mirror method in Fig. 5.3c), albeit the spectral resolution is reduced by a factor of three. Utilizing the left or right third introduces a large alteration in the spectrum due to the shift in the boxcar. However, compensating for the boxcar shift using the complex ILS formulated in Eq. (5.7), allows to derive temperatures from each of the three segments. Evaluation of temperature uncertainties through a Monte Carlo simulation involving 300 samples, incorporating shot noise on the interferogram, reveals that temperature retrievals using the central segment yields a slightly decreased temperature precision compared to that of using the full interferogram, as shown in Fig. 5.3a. Remarkably, despite a spectral resolution reduction by a factor of 3 and a spectral noise increase by a factor of $\sqrt{3}$, the temperature precision only marginally decreases. A study by Galli et al. (2014) explores the impact of spectral resolution in Fourier-transform spectrometers on satellite retrievals, demonstrating a comparatively small increase in retrieval precision with lower spectral resolution. In contrast, utilizing the outer segments leads to a reduction in temperature precision by more than a factor of two. Mapping the three retrieved temperatures back to the initial atmospheric temperature locations indicates that these three temperature data points are well-distributed across the field of view at -22 km, 0 km, and 21 km for the left, center, and right interferogram segments, respectively.

In summary, the theoretical framework outlined here underscores the instrument's capacity to split the field of view into multiple segments. The small-scale simulation, which involved three segments, demonstrates the potential to resolve three horizontally distributed

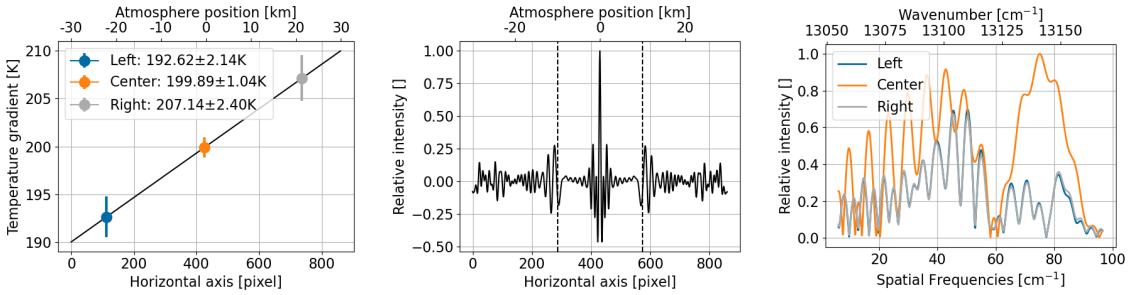

(a) (b) (c)

Figure 5.8: Results of Monte-Carlo simulations with 300 samples where an interferogram with linear temperature gradient including shot noise is split into three parts and subsequently three temperatures are retreived; (a) used temperature gradient from 190K to 210K and retrieved temperatures; (b) interferogram without shot noise showcasing the split positions indicated by the vertical dashed lines; (c) spectra after applying Fourier transformation onto the three parts of the interferogram in (b)

temperatures, although with lower temperature precisions in the two outer segments. When considering the horizontal distribution of the retrieved temperatures, the approach utilizing three segments demonstrates more promising outcomes than the approach using a split field of view into two parts outlined in Sec. 5.1. The latter suffered from small distances between the two retrieved temperatures, leading to limited potential for characterizing horizontal temperature variations. Nonetheless, investigating practical constraints involving the maximum number of segments and their compatibility with apodization and all instrument-related errors requires further exploration.

5.6 Chapter summary

This chapter discusses the instrument's potential to resolve horizontal temperature variations. This objective is achieved by splitting the interferogram at the center and using each mirrored side individually to derive two temperatures from each row, resulting in two 1D temperature profiles from a single image. These horizontally distributed temperature products can be used in wave analysis gaining insights into horizontal wave parameters.

The feasibility of this processing method is first presented in simple examples, showcasing the extraction of two independent temperatures from a 1D interferogram. These examples

reveal that the retrieved temperatures tend to be closer together compared to the central temperatures of each side. This phenomenon arises due to the larger intensity variations of the interferogram close to the center, which carry more temperature information into the spectrum. Additionally, the spectral shot noise is amplified by a factor of $\sqrt{2}$ due to the mirroring of the interferogram and thus also the noise, leading to a corresponding reduction in temperature precision by the same factor.

Exploration of temperature retrieval sensitivity concerning horizontal temperature variations for different background temperatures reveals patterns closely linked to the temperature sensitivity of the O_2 A-band emissions. Lower sensitivity to higher temperatures results in closer retrieved temperature distances for single-sided interferograms at elevated temperatures. Consequently, while temperature variations prevalent in the mesosphere and mesopause regions can be characterized by larger differences between the two retrieved temperatures, those in the lower thermosphere with higher background temperatures yield less precise outcomes.

A comprehensive simulation involving interferograms incorporating temperature variations, often attributed to gravity waves, shows the substantial influence of background temperature and phase of the temperature variation on the distribution of derived temperatures. By compensating for these influences in the wave analysis, accurate estimation of horizontal wave parameter components can be attained.

Given the pronounced impact of larger intensity variations near the interferogram center on this methodology, the effects of apodization are assessed. It is evident that stronger apodization decreases the differences between the retrieved temperatures, thereby diminishing the resolution of horizontal temperature variation. However, apodization primarily serves to counteract instrument-induced errors. Consequently, the selection of apodization degree therefore is a trade off between spatial resolution of the two retrieved horizontal temperatures and resilience against errors.

Lastly, the methodology of a multi-split field of view approach is presented to enhance the horizontal resolution of the retrieved temperature product. This method is subsequently applied to a interferogram split into three segments. The simulation results demonstrates

the potential to resolve three horizontally distributed temperatures with a better horizontal distribution compared to the split approach into two parts, although with lower temperature precisions in the two outer segments. Its compatibility with apodization and all instrument-related errors still needs to be investigated.

Chapter 6

Summary and outlook

Summary

This thesis delves into the data processing of a spatial heterodyne limb sounding interferometer, focusing on the temperature retrieval in the mesosphere and lower thermosphere (MLT). The research centers around the AtmoLITE instrument, which will be deployed in various subsequent sciences missions. It examines the performance and the present status of the data processing, while also addressing error corrections stemming from the as-built instrument. To this end, four topics have been identified in Chap. 1, for which the results are summarized in the following.

Investigating the impact of self-absorption in the radiative transfer model

The radiative transfer model plays a pivotal role in the retrieval process and particularly in simulating the signal strength originating from the oxygen A-band emission. This signal strength is a critical factor influencing noise levels and thus, governing the precision of temperature measurements. One significant improvement is the so far neglected influence of self-absorption, presented in detail in Sec. 4.1.2. Through a series of simulations, it becomes evident that self-absorption's impact escalates at lower altitudes, notably for tangent altitudes below 85 km. Including the self-absorption into the forward model results in radiance simulations comparable to satellite observations taken by OSIRIS and SCIAMACHY. Neglecting self-absorption

results in a steady increase of radiance for decreasing altitudes as depicted by Wroblowski (2023), inducing errors for lower tangent altitudes. Consequently, it is recommend to include self-absorption considerations for tangent altitudes below 85 km.

Assessing the precision of retrieved temperatures from simulated observations taken by AtmoLITE

Given its deployment in forthcoming missions, it is necessary to determine its overall performance and associated uncertainties. An in-depth analysis, presented in Sec. 4.2, reveals a decreasing temperature precision with increasing temperature levels. In summary, daytime simulations exhibit an optimal temperature precision of 1 K to 1.5 K at a tangent altitude of 100 km, assuming an integration time of 1 s. Precision decreases to 4 K for tangent altitudes at 60 km due to pronounced self-absorption effects. For higher altitudes, the precision decreases to 6 K at 140 km due to elevated temperatures and reduced signal strength. Nighttime observations are constrained to the altitude range of 85 km to 105 km due to the rapid attenuation of signals. A higher integration of 10 s allows to gain a temperature precision of about 1 K for tangent altitudes above 93 km with a decreasing temperature precision for lower tangent altitudes. In general, enhancing signal strength can be achieved by increasing vertical binning at the cost of vertical resolution or by extending integration times at the expense of along-track sampling.

Developing correction methods and evaluating their efficacy in terms of retrieved temperatures

A critical topic of this work involves addressing errors stemming from the inherent imperfections of the instrument. A suite of correction methods is proposed and their efficacy are assessed in Sec. 4.3. These error categories span radial distortion, misalignment of gratings, variations in intensity and contrast, phase distortions, and varying Littrow parameters.

Regarding the radial distortion, simulations show that uncorrected distortions introduce a substantial temperature error, which can be considerably reduced by the proposed correction method. However, a sensitivity analysis of that method emphasizes the critical need for precise

extraction of its parameters.

Imperfect grating alignment leads to a phase variation dependent on the vertical axis. Analytically, perfect correction for the error is not feasible. Still, the proposed correction method can help when estimating the interferogram center. The impact onto the temperature retrieval without correction is small and can be decreased to an acceptable level by apodization. Therefore, this error does not need to be considered in the usual processing.

Variations in intensity and contrast are introduced by the instrument's optical system. Simulations demonstrate that the temperature retrieval is sensitive to the contrast variation, which can be considerably reduced by the proposed correction method. Conversely, the retrieval remains insensitive to intensity variation. However, obtaining an accurate intensity estimate remains crucial for a reliable contrast estimate.

The instrument induces a phase variation. Simulations underscore the sensitivity of retrieval accuracy to this error, necessitating correction. The presented correction method exhibits good performance, nearly eliminating all temperature errors related to phase distortion. However, estimation of phase from monochromatic measurements remains the limiting factor in this context.

The Littrow wavenumber and magnification factor can vary, which affects the positioning of instrument line shapes. It is shown that the retrieval is very sensitive to the precise determination of the correct Littrow wavenumber. This aligns with intuition, considering an inaccurate Littrow wavenumber shifts the entire fitted spectrum.

Finally, an end-to-end simulation based on real monochromatic measurements includes all instrument errors at the calibration stage. Performing a data processing including all correction methods reveal that temperature can be retrieved with an accuracy of 1 K for low temperatures, which are present in the upper mesosphere and mesopause region. For higher temperatures and, consequently, for higher tangent altitudes, there is a noticeable increase in temperature error due to the reduced sensitivity of the O_2 A-band. It is important to note that the most significant errors tend to cluster around the same rows across all analyzed temperature levels, suggesting the presence of localized errors that have yet to be identified and corrected.

Exploring a novel processing technique that utilizes a split field of view to resolve horizontal temperature variations

As last topic, this work investigates the instrument's capacity to resolve horizontal across-track temperature variations in Chapter 5. This method involves splitting the field of view, which allows to retrieve two 1D temperature profiles from one image. While simulations demonstrate the feasibility, it is essential to note that the spatial representation of the derived temperatures, defined by the abscissa of the atmospheric model temperature being equal to the retrieved one, is dependent on various parameters of the observed temperature variation.

In general the retrieved temperature differences are smaller than anticipated by half of the field of view, mainly due to heightened intensity variations near the interferogram's center. Additionally, the differences in temperature between the two sides depend on the background temperature and phase of the observed temperature variation. Compensating these influences during the wave analysis enables an accurate estimation of horizontal wave parameters. However, splitting the field of view increases spectral noise, and thus reducing temperature precision. Stronger apodization diminishes temperature differences by giving more weight to the interferogram's center, while enhancing resilience against errors. Therefore, selecting the apodization degree involves a trade-off between horizontal across-track resolution and error robustness.

Moreover, the methodology of a multi-split field of view approach is presented to enhance the horizontal resolution. Simulations with an interferogram split into three segments demonstrate the potential to retrieve three 1D temperature profiles from one image. However, this method's compatibility with apodization and instrument-related errors requires further investigation.

Outlook

The presented data processing development has yielded satisfactory results in terms of temperature accuracy. Nevertheless, several areas for potential improvement are worth considering, which could be part of future research.

The estimation of spatial phase variation showed the highest contribution to the temperature error throughout the applied suite of correction methods. It would be thus beneficial to find a better performing mathematical method for the phase estimation from monochromatic calibration data, to get a more accurate temperature product.

The point spread function (PSF) is not discussed in this work. It can be divided into the PSF of the front optics and the PSF of the camera optics. The latter blurs the interference pattern at the detector, particularly for higher spatial frequencies, which is already addressed by the varying contrast correction. The PSF of the front optics distorts the intensity variation of the incoming radiance, causing a displacement of temperature information. Reliable calibration data from upcoming missions may allow for convolution of the PSF in the 2D spatial domain with simulated radiances in the forward model. However, the challenge remains in accurately splitting the combined PSF into front and camera optics components.

Furthermore, the study does not account for the effect of stray light, primarily impacting daytime simulations. Recent assessments by Kaufmann et al. (2023), utilizing simulated stray light kernels, indicate that tangent altitudes below 85 km are affected by upwelling radiation, while tangent altitudes above 120 km are influenced by stray light due to low signal strength. The validation of simulated stray light kernels using laboratory measurements is ongoing, and potential correction methods could be explored in future research.

In summary, it can be stated that the anticipated accuracy of AtmoLITE as known today will be sufficient to achieve its main objectives to provide a realistic depiction of the dynamic structures in the mesopause region. Over an extended observation period, these measurements will enable the detection of climate change-induced alterations in the dynamics of the upper atmosphere.

Appendices

A.1 List of abbreviations

AIRS	Atmospheric Infrared Sounder
AMSU	Advanced Microwave Sounding Unit
AtmoHIT	Atmospheric Heterodyne Interferometer Test
AtmoLITE	Atmospheric Limb Interferometer for Temperature Exploration
AtmoSHINE	Atmospheric Spatial Heterodyne Interferometer Next Explorer
COTS	Commercial off-the-shelf
FPA	Focal plane array
FTS	Fourier transform spectroscopy
FWHM	Full width at half maximum
GMT	Greenwich mean time
HAMMONIA	Hamburg Model for the Neutral and Ionized Atmosphere
HWHM	Half width at half maximum
ILS	Instrument line shape
INSPIRE	International Satellite Program in Research and Education
LoG	Laplacian of Gaussian
LOS	Line of sight

MATS	Mesospheric Airglow/Aerosol Tomography and Spectroscopy
MIGHTI	Michelson Interferometer for Global High-resolution Thermospheric Imaging
MLS/AURA	Microwave Limb Sounder
MLT	Mesosphere and lower thermosphere
non-LTE	Non-local thermodynamic equilibrium
OSIRIS	Optical Spectrograph and InfraRed Imaging System
PCA	Principal Component Analysis
PSF	Point spread function
REXUS	Rocket EXperiments for University Students
SABER	Sounding the Atmosphere using Broadband Emission Radiometry
SCIAMACHY	SCanning Imaging Absorption spectroMeter for Atmospheric CartograpHY
SHI	Spatial heterodyne interferometer
SHIPAS	Spatial Heterodyne Interferometer Performance Assessment in Space
SNR	Signal-to-noise ratio
SZA	Solar zenith angle
ZOPD	Zero optical path difference

A.2 List of mathematical notation

In this work, conventional italicized symbols (e.g. I, f) are employed to represent real and integer numbers, as well as functions. Bold italicized notation (e.g. $\boldsymbol{x}$) is utilized for vectors, while standard bold symbols (e.g. $\mathbf{S}_\mathrm{a}$) are used for matrices. The most utilized mathematical symbols throughout this work are summarized in the subsequent table for reference.

$\mathbf{A}$	Averaging kernel matrix
A_d	Amplitude of sinusoidal disturbance or perturbation used in sensitivity analyses
A_{ij}	Einstein coefficient from upper state i to lower state j
A_σ	Spatial contrast variation for wavenumber σ, also referred to as amplitude
B_σ	Spatial intensity variation for wavenumber σ, also referred to as baseline
C_d	Dark current
d^{-1}	Grating groove density
e	Exponential function
f	Spatial frequency function
F	The forward model mapping an atmospheric state onto simulated radiances
$\mathcal{F}$	Fourier transformation
F_{ILS}	Instrument line shape of an ideal instrument determined by the Fourier transform of the apodization function
$\mathbf{F}'(\boldsymbol{x})$	Jacobian matrix of F evaluated at $\boldsymbol{x}$ via finite difference
g	Function mapping a horizontal temperature variation onto a retrieved temperature
h	Horizontal temperature variation function
$\mathbf{G}$	Gain matrix
i	Imaginary number
I	Interferogram function

$\mathbf{I}_\mathrm{N}$	Identity matrix with dimension of $\mathbb{R}^{N\times N}$
J	Source or emission function
k	Fitting parameter of division model used in radial distortion correction
k_a	Absorption coefficient
L	Half of the interferogram length
M^{-1}	Magnification factor of camera optics
n_i	Number density of excited O_2 in rotational state i
p	Pressure
R	Radiance function
r_u	undistorted radius
r_d	distorted radius
s	Line of sight (LOS) distance fron the instrument
S	Spectrum function
$\mathbf{S}_\epsilon$	Covariance matrix of the measurement error ϵ
$\mathbf{S}_\epsilon^{-1}$	Measurement error precision matrix; inverse of $\mathbf{S}_\epsilon$
$\mathbf{S}_\mathrm{a}$	Covariance matrix of the differences between a priori and state parameter vector
$\mathbf{S}_\mathrm{a}^{-1}$	A priori precision matrix; pseudo-inverse of $\mathbf{S}_\mathrm{a}$
T	Temperature
$\boldsymbol{T}$	Horizontal temperature variation
$\boldsymbol{T'}$	Horizontal temperature residual
$\bar{T}$	Horizontal background (mean) temperature
t_{int}	Integration time
x	Horizontal axis on the detector and across-track axis in the atmosphere
$\boldsymbol{x}_s$	Atmospheric state parameter

$\boldsymbol{x}_f$	Final retrieval result
$\boldsymbol{x}_a$	A priori knowledge of atmospheric state
$\boldsymbol{x}_t$	True atmospheric state
y	Vertical axis on the detector
$\boldsymbol{y}$	Measurement vector
z	Vertical atmospheric axis
$\hat{z}$	Axis perpendicular to the detector plane
$\frac{\alpha}{2}$	Misalignment angle between the two gratings
$\boldsymbol{\varepsilon}$	Measurement error vector
η	Rotation angle of monochromatic fringe pattern
θ_L	Littrow angle
κ	Spatial frequency
λ	Wavelength
Π	boxcar function
σ	Wavenumber
σ_L	Littrow wavenumber
ϕ_d	Phase of sinusoidal disturbance or perturbation used in sensitivity analyses
Φ	General phase of Fourier Transform
Φ_σ	Spatial phase variation for wavenumber σ
Ш	Infinite impulse train

A.3 Overview of spaceborne instruments used for gravity wave research

Since the early 1990s, one effective method for studying gravity waves is radio occultation, which involves GPS-satellites. The successful application of this technique in observing gravity waves has been demonstrated by Rocken et al. (1997) and Tsuda et al. (2000). Notably, the COSMIC-1 satellite constellation, launched in 2006, has been utilized to observe gravity waves in the altitude range below 30 km, as illustrated by Hindley et al. (2015). Moreover, with the introduction of the updated COSMIC-2 constellation in 2019, further data will be made available for studying the lower atmosphere region (Schreiner et al., 2020).

Another technique is passive remote sensing, as introduced in the introduction in Chap. 1. This observational method has already been used by multiple spaceborne instruments to observe gravity wave activity in several regions of the atmosphere. An overview of instruments flown in the last decades and their corresponding altitude ranges used for the gravity wave research is shown in Fig. 7.1 with more details and references for each instrument given in Tab. 7.3. AIRS and AMSU are both nadir instruments, which refers to the downward-facing viewing geometry. The rest of the presented instruments use limb geometry. Alexander and Barnet (2007) demonstrates that nadir instruments excel in horizontal resolution while lacking in vertical resolution. Conversely, limb instruments exhibit the opposite pattern, boasting good vertical resolution while their horizontal resolution is comparatively limited. Preusse et al. (2008) shows that nadir instruments have the capability to resolve gravity waves with vertical wavelengths larger than 15 km. On the other hand, limb sounding instruments can achieve higher vertical resolution, allowing them to effectively resolve gravity waves with vertical wavelengths larger than 2 km, provided that the instrument's vertical resolution is sufficiently high. Examining the timeline presented in Fig. 7.1a, it becomes evident that no new missions have been initiated between 2008 and 2018. Although there are still a few instruments in space, such as SABER, OSIRIS, and MLS/AURA, that continue to provide reliable data, they have significantly surpassed their estimated lifetimes and are likely to cease functioning soon. Recently launched instruments like MIGHTI and MATS attempt to address the 'thermospheric gap' in

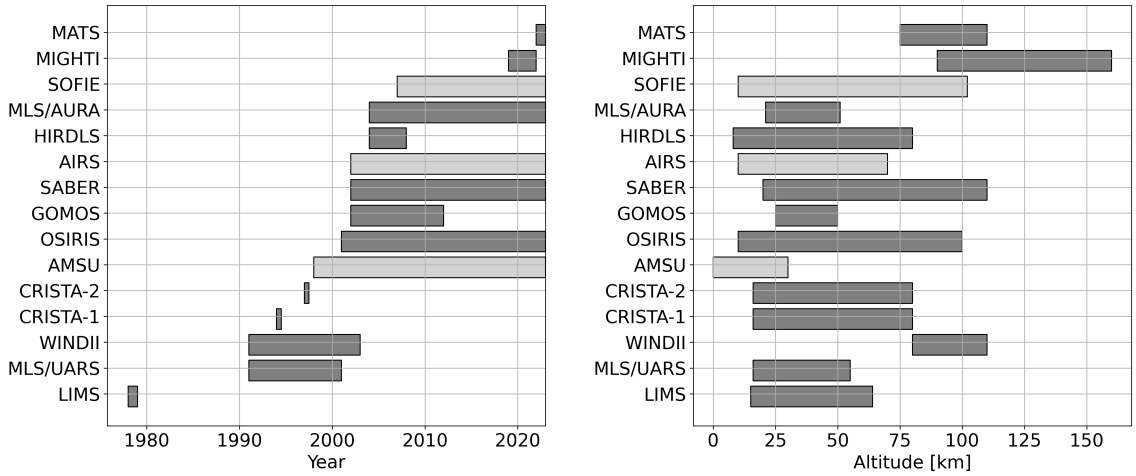

(a) (b)

Figure 7.1: Overview of spaceborne instruments used for gravity wave research in the last decades; (a) temporal range of operation (b) altitude range used for gravity wave observation; full name of the instruments and references are given in Tab. 7.3; AIRS and AMSU are nadir instruments and thus have a weak vertical resolution; SOFIE measures only in the polar region and thus has a low coverage;

the MLT region. Nevertheless, MIGHTI concluded its mission as intended by the end of 2022, while MATS is projected to have a mission span of approximately two years. Consequently, a void in atmospheric data suitable for gravity wave research is anticipated to arise.

Table 7.3: Full name of instruments used in in the overview presented in Fig. 7.1;

Acronym	Full instrument name	Satellite	References
MATS	Mesospheric Airglow/Aerosol Tomography and Spectroscopy	MATS	Gumbel et al. (2020)
MIGHTI	Michelson Interferometer for Global High-resolution Thermospheric Imaging	ICON	(Englert et al., 2017; Triplett et al., 2023)
SOFIE	The Solar Occultation forIce Experiment	AIM	Liu et al. (2014)
MLS/AURA	Microwave Limb Sounder	AURA	Wu and Eckermann (2008)
HIRDLS	High Resolution Dynamics Limb Sounder	AURA	Gille et al. (2008)
AIRS	Atmospheric Infrared Sounder	Aqua	Alexander and Barnet (2007); Hoffmann and Alexander (2009); Ern et al. (2017)
SABER	Sounding the Atmosphere using Broadband Emission Radiometry	TIMED	Russell III et al. (1999); Preusse et al. (2006); Huang et al. (2006)
GOMOS	Global Ozone Monitoring by Occultation of Star	Envisat	Sofieva et al. (2007)
OSIRIS	Optical Spectrograph and Infrared Imager System	Odin	Llewellyn et al. (2004); Sheese et al. (2010)
AMSU	Advanced Microwave Sounding Unit	multiple satellites	Wu (2004)
CRISTA	Cryogenic Infrared Spectrometers and Telescopes for the Atmosphere	space shuttles	Offermann et al. (1999); Preusse et al. (2002)
WINDII	WIND Imaging Interferometer	UARS	Shepherd et al. (1993, 2012)
MLS/UARS	Microwave Limb Sounder	UARS	Wu and Waters (1996); McLandress et al. (2000); Huang et al. (2006)
LIMS	Limb Infrared Monitoring of the Stratosphere	Nimbus-7	Fetzer and Gille (1994)

A.4 Number density of oxygen in excited and ground state

In Section 2.3, it is argued that the absorption can be effectively represented as if it were in LTE. This assertion follows from the population ratio of excited $O_2(b^1\Sigma_g^+, v = 0)$ molecules to those in their ground state ($O_2(X^3\Sigma_g^-, v = 0)$) being exceedingly small. Consequently, the line strengths of the emission lines in a non-LTE environment closely approximate those in LTE, as demonstrated by López-Puertas and Taylor (2001). The number density of O_2 molecules in excited and ground state within the O_2 A-band emission and their ratios are thus shown in Fig. 7.2a and 7.2b, respectively, which validates this assumption.

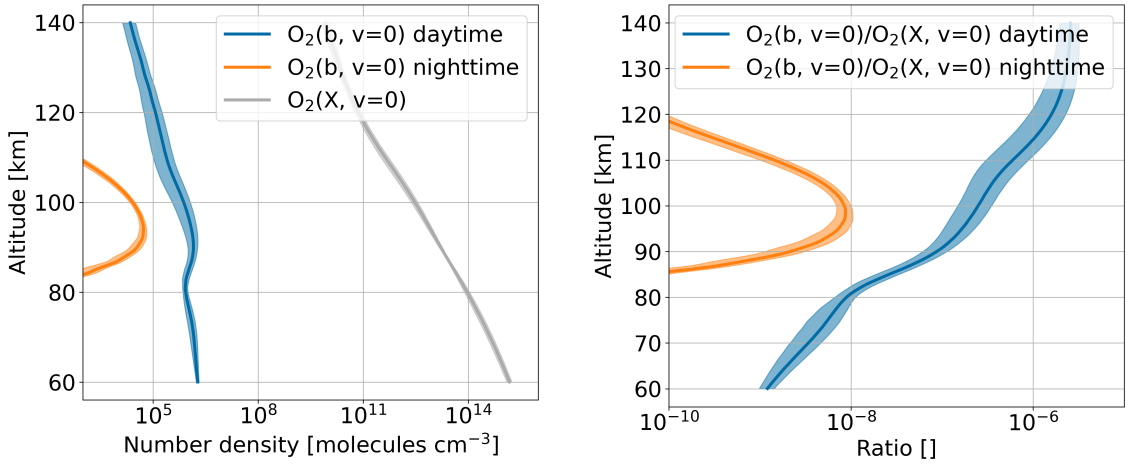

(a) (b)

Figure 7.2: (a) Simulated number density of oxygen molecules in excited state $O_2(b^1\Sigma_g^+, v = 0)$ and in ground state $O_2(X^3\Sigma_g^-, v = 0)$; (b) ratio of number density of oxygen molecules in excited state to those in ground state; the mean and standard deviation are shown in solid line and shaded area, respectively, using the test data set from HAMMONIA model runs, defined in Sec. 4.1.1;

A.5 Implementation, limitations and possible improvements of the radiative transfer model

A.5.1 Implementation

The implementation approximates the continuous radiative transfer equation presented in Eq (2.13). Hereby, a 1D atmospheric model with spherical geometry is assumed where the variables are only dependent on altitude. As shown in Fig. 7.3, the path length along the LOS for a given altitude can be calculated by Pythagorean theorem following

$$d_{kl} = \begin{cases} \sqrt{(z_l + r_E)^2 - (z_{t_k} + r_E)^2} & \text{if } z_l \geq z_{t_k} \\ 0 & \text{else} \end{cases} \tag{A.5.1}$$

$$\Delta d_{kl} = d_{kl} - d_{k(l+1)} \tag{A.5.2}$$

where z_l refers to the atmospheric altitude layer l, z_{t_k} denotes the k^{th} tangent altitude of a given LOS, and r_E is the Earth's radius. Each atmospheric layer is treated as homogeneous gas cell, where the emission and absorption can be tabulated for each cell locally. Subsequently, the LOSs for different tangent altitudes are defined and Eq (2.13) is approximated by two Riemann integrals.

An investigation into the sensitivity of the radiative transfer model is conducted with respect to variations in spatial and spectral step sizes, as well as line shape. This study is

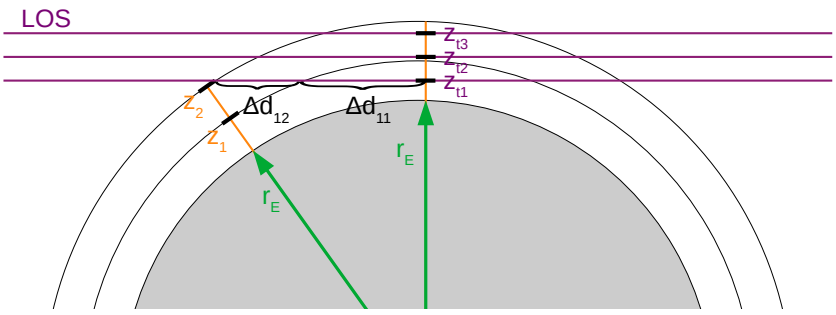

Figure 7.3: Path length along the LOS for given tangent altitudes; z and z_t refers to the altitude coordinate and the tangent altitude, respectively; r_E denotes the Earth's radius;

Table 7.5: Sensitivity study results of the radiative transfer model; the errors are given based on the spectrally integrated radiance evaluated at various tangent altitudes; detailed results are given in Appx. A.6

Parameter	Value	Error
Vertical discretization	$<0.5\,\mathrm{km}$	$<3\,\%$
Layers above tangent altitudes	$>20\,\mathrm{km}$	$<2.5\,\%$
Line shape	Gaussian	$<0.05\,\%$
Spectral discretization	$<0.01\,\mathrm{cm}^{-1}$	$<0.01\,\%$

thoroughly presented in Sec. A.6. The main finding are summarized in Tab. 7.5.

Section A.6.4 shows that the model needs a fine discretization of the spectral axis with a step size smaller than $0.01\,\mathrm{cm}^{-1}$ to resolve the shape of the emission lines. However, most of the spectrum is close to zero as the emission lines are very narrow. To decrease the computational cost, the spectral axis is only evaluated on small windows around each emission lines. A few emission lines at the upper end of the spectrum are spectrally overlapping, where special care is taken for those by placing them in the same window. As proxy for the window size, four times the maximal FWHM of the emission lines is taken to ensure that the sides of the emission lines approach zero. The maximal difference between a simulation on small windows compared to the simulation evaluated on the full spectral grid is six magnitudes lower compared to the signal. Thus, the sparse method is used as the standard for the forward calculation due to the decrease of the computational cost by a factor of five.

A.5.2 Limitations and possible improvements

The current implementation employs an equidistant grid, which requires a fine vertical sampling of the atmosphere of at least 0.5 km. This level of resolution is critical to prevent errors in the tangent layer, where the LOS path length is significantly longer compared to the atmospheric layers above. However, it is important to note that the fine vertical discretization is unnecessary for the layers situated above the tangent layer. To enhance the model's efficiency, a potential improvement involves a coarser sampling approach for the general atmosphere and applying fine sampling exclusively around the tangent altitudes. A different approach could

involve merging multiple layers by Curtis-Godson approximation (López-Puertas and Taylor, 2001; Rodgers, 2000). Implementing such improvements however, would require a smart approach, potentially exploiting parallelization, to beat the current implementation in terms of computational cost, which relies on the array-based parallelization of *numpy*.

Moreover, given that higher tangent altitudes remain unaffected by self-absorption effects, as depicted in Fig. 4.2b, one potential optimization involves excluding the transmittance term from the radiative transfer equation for these layers. This adjustment has the potential to further accelerate the radiative transfer model's computations.

It's important to highlight that the speed of the forward model holds significant importance, as it is call several 100 times within the temperature retrieval optimization process introduced in Section 3.4.1.

A.6 Sensitivity study of the radiative transfer model

In this section, we showcase the outcomes of the sensitivity study pertaining to the parameters of the radiative transfer model. The key highlights of these results can be found in Tab. 7.5.

A.6.1 Vertical discretization

A sufficiently small vertical discretization step size is crucial, because it defines the step size of the Riemann integrals approximating the double integral in the radiative transfer equation given by Eq. (2.13). Multiple simulation runs were conducted using different vertical step sizes in the 1D spherical atmospheric model. The spectrally integrated radiances are presented in Fig. 7.4a and Fig. 7.4b for day- and nighttime conditions, respectively. The simulation with a step size of 0.1 km is taken as a reference. In the daytime simulation, larger discretization errors are observed for tangent altitudes below 110 km. Conversely, in the nighttime simulation, the opposite trend is observed, with higher tangent altitudes above 110 km being more affected. However, the signal in this region is low, resulting in relatively small absolute errors. Based on the outcomes of these simulations, it is advisable to choose a vertical step size below 0.5 km, which limits the error to 3 %.

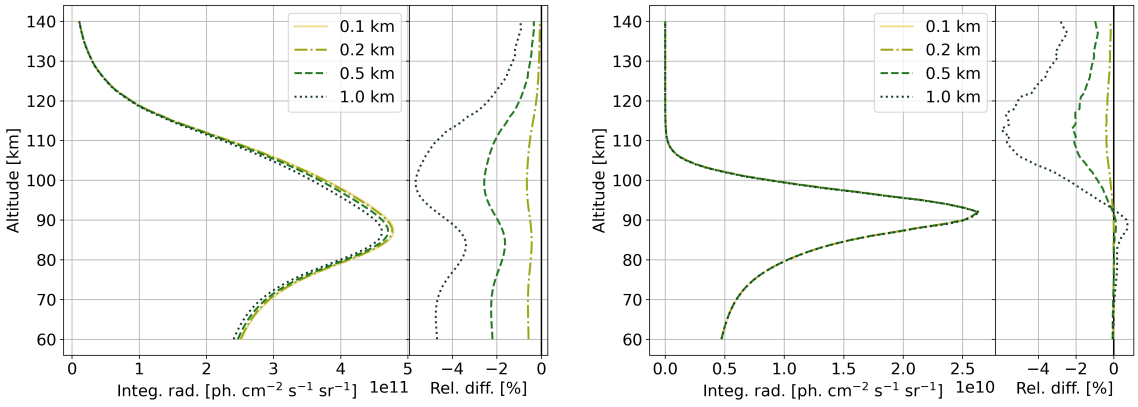

(a) (b)

Figure 7.4: Spectrally integrated radiance computed for simulations employing varying vertical discretization step sizes, considering (a) daytime and (b) nighttime conditions; the relative differences in the right panel are given with respect to the simulation using a step size of 0.1 km;

A.6.2 Modeling the top of the atmosphere

Incorrect modeling of the top of the atmosphere can introduce errors, particularly in higher tangent altitudes. In order to assess this effect, multiple simulation runs were conducted, considering varying top of atmosphere altitudes. The spectrally integrated radiance of the daytime simulations depicted in Figure 7.5a reveal that the simulated atmosphere should be extended by at least 20 km above the highest tangent altitude. This extension helps to limit the errors to 2.5 % in the upper tangent altitudes. The nighttime simulations displayed in Figure 7.5b are less affected by errors and the signal approaches zero for high tangent altitude entailing a small absolute error.

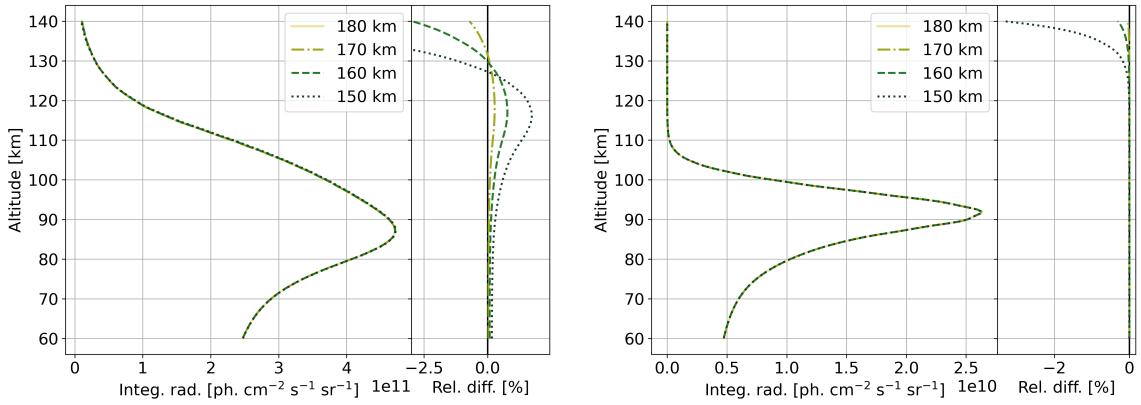

(a) (b)

Figure 7.5: Spectrally integrated radiance computed for simulations employing varying top of atmosphere altitudes, considering (a) daytime and (b) nighttime conditions; the relative differences in the right panel are given with respect to the simulation using a top of atmosphere at 180 km;

A.6.3 Line shape

Emission lines can be widened due to collisions between molecules, referred to as pressure broadening, and due to thermal motions of the molecules, referred to as Doppler broadening. The line shape due to Doppler broadening follows a Gaussian shape and is defined in Eq. (2.14). The pressure broadening is temperature and pressure dependent and described by a Lorentzian shape denoted by

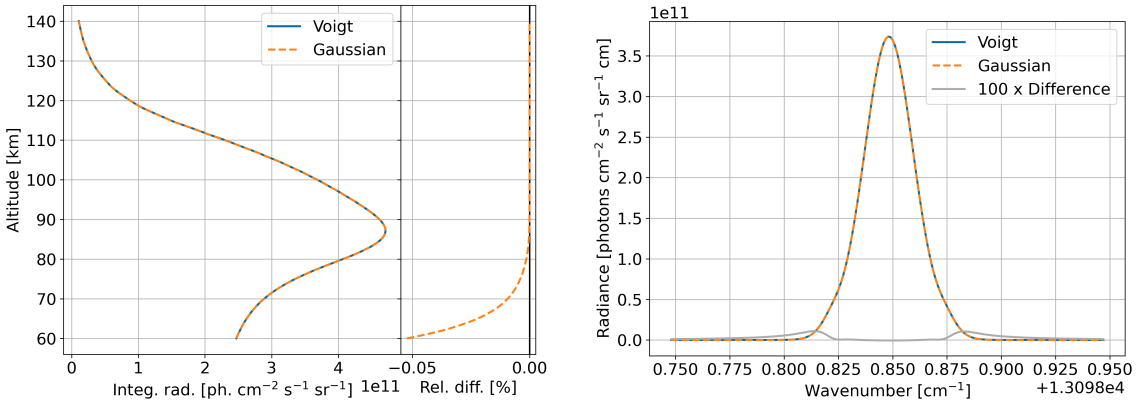

(a) (b)

Figure 7.6: (a) Spectrally integrated radiance of daytime simulations using Voigt and Gaussian line shape; right panel shows the difference of the simulation using a Gaussian line relative to the simulation using Voigt line shape; (b) strongest emission line within the simulation using the Voigt line shape compared to the same emission line in the simulation using Gaussian line shape; the difference (Voigt - Gaussian) is amplified by a factor of 100;

$$P_{ij}(\sigma, p, T) = \frac{1}{\pi} \frac{\alpha_P(p,T)}{\alpha_P(p,T)^2 + (\sigma - \sigma_{ij}^*)^2}, \tag{A.6.1}$$

where $\sigma_{ij}^* = \sigma_{ij} + \delta(p_{ref})p$ is the pressure shift corrected line position, and $\alpha_P(p,T)$ denotes the HWHM of the line shape defined by

$$\alpha_P(p,T) = \alpha_{ref} \frac{p}{p_{ref}} \left(\frac{T_{ref}}{T} \right)^k \tag{A.6.2}$$

where α_{ref} is the HWHM at reference temperature T_{ref} and standard pressure p_{ref}, and k is a coefficient dependent on the emission line.

If both broadening mechanisms are present at the same time, the convolution of the Gaussian and Lorentzian shape is taken, which is referred to as Voigt profile. The latter is numerically approximated following Schreier (2011) which is based on Humlíček (1982) and Weideman (1994). Note that for decreasing pressure, α_P in Eq. (A.6.2) converges to zeros, causing the Voigt line shape to converge towards a Gaussian profile.

In order to evaluate the altitude at which pressure broadening becomes significant, two simulation runs are conducted: one considering only Doppler broadening, and the other in-

corporating both broadening effects. Figure 7.6a shows the spectrally integrated radiance during daytime for the two simulation runs. The simulation using the Gaussian line shape exhibits slight deviations for tangent altitudes below 80 km. Nevertheless, these deviations are extremely small and can be disregarded. The slightly enhanced flanks of the Voigt line shape, attributed to the pressure-induced Lorentzian shape, become apparent only when the differences are amplified, as demonstrated in Figure 7.6b.

A.6.4 Spectral discretization

This section determines the spectral discretization step size necessary to resolve narrow emission lines. To achieve this, simulations with various spectral step sizes are conducted and compared. Figure 7.7b demonstrates that a step size of at least $0.01\,\mathrm{cm}^{-1}$ is necessary to resolve the peak of the emission line. Evaluating the spectrally integrated radiance for each tangent altitude in Figure 7.7a reveals that only minor errors are introduced. However, it is still recommended to run the simulation with a step size below or equal to $0.01\,\mathrm{cm}^{-1}$ in order to accurately capture the shape of the emission lines and prevent the leakage of line strength to neighboring samples.

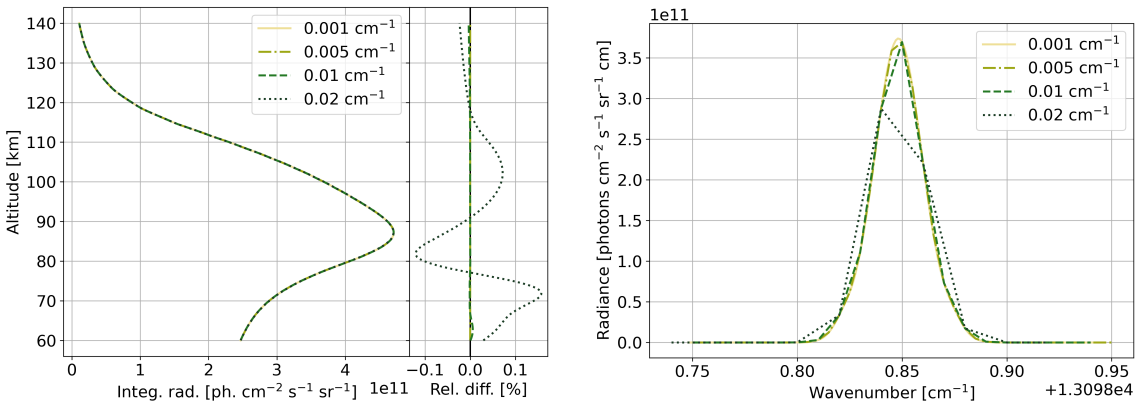

(a) (b)

Figure 7.7: (a) Spectrally integrated radiance using various spectral discretization step sizes for daytime conditions; the relative differences in the right panel are given with respect to the simulation using a step size of $0.001\,\mathrm{cm}^{-1}$; (b) one example of a resolved emission line for different spectral discretization step sizes; the strongest emission line within the simulation is selected;

A.7 Additional material to Norton-Beer apodization

Section 3.2.4 shows that the Norton-Beer apodization has favorable properties for Fourier-transform spectroscopy. Norton and Beer (1976) and Norton and Beer (1977) provide the analytical solution of the Fourier transform for the Norton-Beer weak, medium and strong apodizations. This is not provided for the extended apodization functions given by Naylor and Tahic (2007), which is defined by Eq. (3.23) with the parameters given in Tab. 7.7. Therefore, a general analytical solution for its Fourier transform is presented in Sec. A.7.1, following Ntokas et al. (2023b). Furthermore, a python-toolbox was developed by Ntokas (2023), which allows to generate the Norton-Beer apodization and its Fourier transform for any given parameter set, presented thereafter in Sec. A.7.2.

Table 7.7: Parameters of the extended Norton-Beer apodization given by Naylor and Tahic (2007); the FWHM are given relative to the FWHM of the sinc function; 1.0 corresponds to the boxcar window;

FWHM	c_0	c_1	c_2	c_4	c_6	c_8
1.0	1	0	0	0	0	0
1.1	0.701551	-0.639244	0.937693	0	0	0
1.2	0.396430	-0.150902	0.754472	0	0	0
1.3	0.237413	-0.065285	0.827872	0	0	0
1.4	0.153945	-0.141765	0.987820	0	0	0
1.5	0.077112	0	0.703371	0.219517	0	0
1.6	0.039234	0	0.630268	0.234934	0.095563	0
1.7	0.020078	0	0.480667	0.386409	0.112845	0
1.8	0.010172	0	0.344429	0.451817	0.193580	0
1.9	0.004773	0	0.232473	0.464562	0.298191	0
2.0	0.002267	0	0.140412	0.487172	0.256200	0.113948

A.7.1 Derivation of the analytical Fourier transform of the Norton-Beer apodization

In this section, the mathematical derivation of the Fourier transform is presented, which corresponds to the generic form of the Norton-Beer apodization given in Eq. (3.23). Utilizing

the linearity property of the Fourier transform, it is given by

$$\mathcal{F}(A_{NB})(\sigma) = \sum_{k=0}^{K} c_k \underbrace{\mathcal{F}\left(\left[1 - \left(\frac{x}{L}\right)^2\right]^k\right)}_{=:Q_k}, \tag{A.7.1}$$

which places the parameters c_k outside of the Fourier transform. This allows to apply the following solution to any set of parameters. Q_k can be calculated by

$$Q_k = \int_{-L}^{L} \left[1 - \left(\frac{x}{L}\right)^2\right]^k e^{-i2\pi\sigma x} dx \tag{A.7.2}$$

$$= \sum_{m=0}^{k} \binom{k}{m} (-1)^m \underbrace{\int_{-L}^{L} \left(\frac{x}{L}\right)^{2m} e^{-i2\pi\sigma x} dx}_{=:\tilde{Q}_m} \tag{A.7.3}$$

where the binomial theorem is used in Eq. (A.7.3). $\tilde{Q}_0$ can be calculated by applying the fundamental theorem of calculus, given by

$$\tilde{Q}_0 = 2L \ \mathrm{sinc}(a), \tag{A.7.4}$$

where $a = 2\pi\sigma L$. $\tilde{Q}_m$ can be calculated recursively by using integration of parts twice, given by

$$\tilde{Q}_m = \int_{-L}^{L} \left(\frac{x}{L}\right)^{2m} e^{-i2\pi\sigma x} dx \tag{A.7.5}$$

$$= \left[\frac{1}{-i2\pi\sigma} e^{-i2\pi\sigma x} \left(\frac{x}{L}\right)^{2m}\right]_{-L}^{L} - \frac{2m}{-i2\pi\sigma L} \int_{-L}^{L} \left(\frac{x}{L}\right)^{2m-1} e^{-i2\pi\sigma x} dx \tag{A.7.6}$$

$$= 2L \ \mathrm{sinc}(2\pi\sigma L) - \frac{2m}{-i2\pi\sigma L} \left(\left[\frac{1}{-i2\pi\sigma} e^{-i2\pi\sigma x} \left(\frac{x}{L}\right)^{2m-1}\right]_{-L}^{L} - \right. \tag{A.7.7}$$

$$\left. \int_{-L}^{L} \frac{2m-1}{L} \left(\frac{x}{L}\right)^{2m-2} \frac{1}{-i2\pi\sigma} e^{-i2\pi\sigma x} dx \right) \tag{A.7.8}$$

$$= 2L \left(\mathrm{sinc}(2\pi\sigma L) + \frac{2m}{(2\pi\sigma L)^2} \cos(2\pi\sigma L)\right) - \frac{2m(2m-1)}{(2\pi\sigma L)^2} \tilde{Q}_{m-1} \tag{A.7.9}$$

$$= 2L \left(\mathrm{sinc}(a) + \frac{2m}{a^2} \cos(a)\right) - \frac{2m(2m-1)}{a^2} \tilde{Q}_{m-1} \,. \tag{A.7.10}$$

Using Eq. (A.7.3), Eq. (A.7.4) and Eq. (A.7.10), Q_k normalized by the length of the

interferogram for k up to 8 are given by

$$Q_0 = \mathrm{sinc}(a) \tag{A.7.11}$$

$$Q_1 = \frac{2}{a^2}(\mathrm{sinc}(a) - \cos(a)) \tag{A.7.12}$$

$$Q_2 = 8[\left(-\frac{1}{a^2} + \frac{3}{a^4}\right)\mathrm{sinc}(a) - \frac{3}{a^4}\cos(a)] \tag{A.7.13}$$

$$Q_3 = 48[\left(-\frac{6}{a^4} + \frac{15}{a^6}\right)\mathrm{sinc}(a) + \left(\frac{1}{a^4} - \frac{15}{a^6}\right)\cos(a)] \tag{A.7.14}$$

$$Q_4 = 384[\left(\frac{1}{a^4} - \frac{45}{a^6} + \frac{105}{a^8}\right)\mathrm{sinc}(a) + \left(\frac{10}{a^6} - \frac{105}{a^8}\right)\cos(a)] \tag{A.7.15}$$

$$\begin{aligned} Q_5 = 3\,840[&\left(\frac{15}{a^6} - \frac{420}{a^8} + \frac{945}{a^{10}}\right)\mathrm{sinc}(a) + \\ &\left(-\frac{1}{a^6} + \frac{105}{a^8} - \frac{945}{a^{10}}\right)\cos(a)] \end{aligned} \tag{A.7.16}$$

$$\begin{aligned} Q_6 = 46\,080[&\left(-\frac{1}{a^6} + \frac{210}{a^8} - \frac{4\,725}{a^{10}} + \frac{10\,395}{a^{12}}\right)\mathrm{sinc}(a) + \\ &\left(-\frac{21}{a^8} + \frac{1\,260}{a^{10}} - \frac{10\,395}{a^{12}}\right)\cos(a)] \end{aligned} \tag{A.7.17}$$

$$\begin{aligned} Q_7 = 645\,120[&\left(-\frac{28}{a^8} + \frac{3\,150}{a^{10}} - \frac{62\,370}{a^{12}} + \frac{135\,135}{a^{14}}\right)\mathrm{sinc}(a) + \\ &\left(\frac{1}{a^8} - \frac{378}{a^{10}} + \frac{17\,325}{a^{12}} - \frac{135\,135}{a^{14}}\right)\cos(a)] \end{aligned} \tag{A.7.18}$$

$$\begin{aligned} Q_8 = 10\,321\,920[&\left(\frac{1}{a^8} - \frac{630}{a^{10}} + \frac{51\,975}{a^{12}} - \frac{945\,945}{a^{14}} + \frac{2\,027\,025}{a^{16}}\right)\mathrm{sinc}(a) + \\ &\left(\frac{36}{a^{10}} - \frac{6\,930}{a^{12}} + \frac{270\,270}{a^{14}} - \frac{2\,027\,025}{a^{16}}\right)\cos(a)]\ . \end{aligned} \tag{A.7.19}$$

A.7.2 Python toolbox for Norton-Beer apodization and its Fourier transform

Following Ntokas et al. (2023b), a free Python toolbox called *norton_beer* is developed. It allows to generate the apodization window and its analytical Fourier transform for a given set of parameters. The generation of the apodization window is straight forward and will not be discussed in detail. The generation of its Fourier transform calculates the Q_k presented in Eq. (A.7.3) using the recursive form for $\tilde{Q}_m$ shown in Eq. (A.7.4) and Eq. (A.7.10). For $\mid a \mid < 1$, the analytical solution becomes numerically unstable due to the a^{2n} for $n = 1, 2, ...$

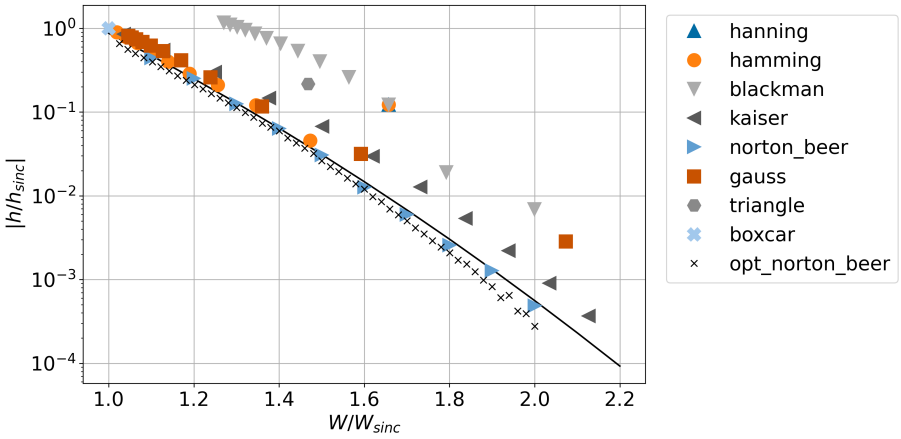

Figure 7.8: Filler's Diagram for commonly used apodization functions with different parameters; the functions and used parameters for each apodization window are presented in Tab. 7.8; the parameters in increasing order correspond to the markers from small to large FWHM, except for Hamming and Gauss window, where it corresponds to the markers from large to small FWHM; the solid line represents the boundary defined by the Eq. (3.22); 'opt_norton_beer' shows the result for newly generated apodization function using the optimization algorithm presented in Sec. A.7.2;

in the divisor. The evaluated Q_1 to Q_8 in Eq. (A.7.12)–A.7.19 show examples of the divisors a^{2n} for n up to 8. Taylor expansion is used for the cos and sinc, denoted by

$$cos(a) = \sum_{n=0}^{\infty} \frac{(-1)^n}{(2n)!} a^{2n} \tag{A.7.20}$$

$$sinc(a) = \sum_{n=0}^{\infty} \frac{(-1)^n}{(2n+1)!} a^{2n},, \tag{A.7.21}$$

which eliminates the a^{2z}. Note that at least the first K summands in the Taylor series needs to be taken to eliminate all denominator, where K is the number of parameters used in Eq (3.23). To ensure a high level of accuracy, the toolbox calculates the first $2(K+1)$ summands. This effectively reduces the maximal approximation error below 1×10^{-10}. To reduce the computational cost, the scalar numerators are calculated first, resulting in the numerators in Eq. (A.7.12)–(A.7.19). Subsequently, the sinc- and cosine functions are evaluated on the abscissa a and summed up with the denominators a^{2n}. This allows to calculate sinc(a), cos(a) and $\frac{1}{a^{2n}}$ for each n only once.

Window	Function defined for $x \in [-L, L]$	Parameter range of p (min, max, step)	Reference
Hamming	$p + (1-p)\cos\left(2\pi\frac{x}{L}\right)$	$(0.5, 0.95, 0.05)$	Harris (1978)
Blackman	$\frac{1-p}{2} + \frac{1}{2}\cos\left(2\pi\frac{x}{L}\right) + \frac{p}{2}\cos\left(4\pi\frac{x}{L}\right)$	$(-1, 0.2, 0.1)$	Harris (1978)
Hanning	$\frac{1}{2} + \frac{1}{2}\cos\left(2\pi\frac{x}{L}\right)$	None	Naylor and Tahic (2007)
Kaiser	$I_0[\pi p\sqrt{1-(x/L))^2}]/I_0[\pi p]$	$(1, 11, 1)$	Kaiser and Schafer (1980)
Gauss	$e^{-\frac{1}{2}\left(\frac{1}{p}\frac{x}{L}\right)^2}$	$(0.3, 1.3, 0.1)$	Harris (1978)
Norton-Beer	Eq. (3.23) & Tab. 7.7	$(1.0, 2.0, 0.1)$	Naylor and Tahic (2007)
Triangle	$1 - \frac{\lvert x\rvert}{L}$	None	Harris (1978)

Table 7.8: Apodization functions and parameters used in Fig. 3.4 and Fig. 7.8; I_0 in the definition of the Kaiser window is the zeroth-order modified Bessel function of the first kind;

Furthermore, new apodization functions can be generated, where the parameters are optimized for a given FWHM so that the absolute maximal value of the side lobes is minimized. Hereby, the objective function takes a set of parameters, calculates the Fourier transform of the apodization window for the given parameter set, and derives the FWHM of the main lobe and the absolute maximum of the first side lobe. These two measures are used in the minimization process to optimize the parameter set, denoted by

$$\min_{p} \; c(W_{want} - W)^2 + h \tag{A.7.22}$$

where p refers to the parameter set, W_{want} and W denotes the wanted and gained FWHM of the main lobe, h is the absolute maximum of the first side lobe, and c a weighting factor. The weighting factor is set to 500 by default to ensure a resulting apodization function which Fourier transform main lobe's FWHM is close to the aimed FWHM. However, the weighting factor can be adjusted. This can be done for a fixed number of parameters or for a range of numbers, where the minimum value of that range is returned. The latter is used to generate new apodization functions for multiple relative FWHMs. Figure 7.8 compares the FWHMs and absolute maxima of the side lobes of the Fourier transform of the newly generated apodization functions with commonly used apodization windows defined in Tab. 7.8 as it was already done in Fig. 3.4. The newly generated apodization functions using the opti-

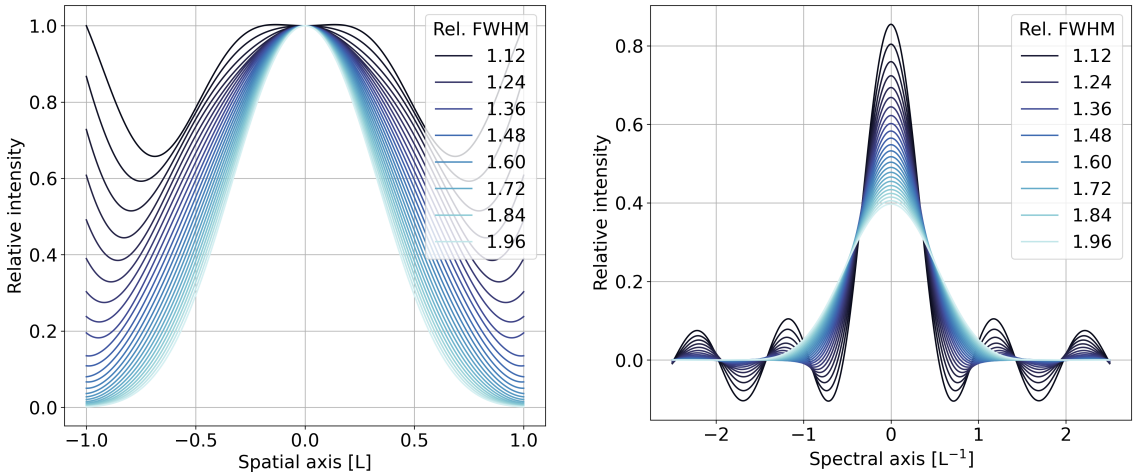

(a) (b)

Figure 7.9: Newly generated Norton-Beer apodization functions using the optimization algorithm from Sec. A.7.2 in (a) spatial domain and (b) spectral domain; every second x-marker from Fig. 7.8 is presented; the legend shows the relative FWHM set at the beginning of the optimization;

mization algorithm consistently lie below the solid boundary line for relative FWHM values ranging from 1 to 2. This demonstrates that the Python toolbox is capable of generating novel apodization functions within that specific FWHM range. The optimized apodization windows and their Fourier transform are presented in Fig. 7.9. It is remarkable that for very low FWHM below 1.2, the apodization functions increase again towards the edges indicating inadequate suppression of discontinuity. This phenomenon occurs because the procedure focuses solely on the minimization of the maximal absolute values of the first side lobe, neglecting the decay of the side lobes. However, the decay of the side lobes is closely connected to the suppression of the discontinuity (Zhu and Griffiths, 1998).

A.8 Shot noise propagation into the spectral space

A noisy interferogram can be described by

$$\hat{I}[n] = I[n] + \varepsilon[n] \tag{A.8.1}$$

where $\hat{I}$ is the interferogram with noise, I denotes the non-noisy interferogram and ε refers to the shot noise described by the normal distribution

$$\varepsilon[n] \sim \mathcal{N}(0, \overline{I}) \tag{A.8.2}$$

where $\overline{I}$ is the mean of the signal. The shot noise can be propagated through the Fourier transformation, resulting in a noisy spectrum where the imaginary and real part can be represented by two Gaussian random variables given by

$$\mathrm{Re}(\hat{S}[k]) \sim \mathcal{N}(S[k], \frac{\overline{I}}{2N}) \tag{A.8.3}$$

$$\mathrm{Im}(\hat{S}[k]) \sim \mathcal{N}(0, \frac{\overline{I}}{2N}) \tag{A.8.4}$$

where N is the number of samples in the interferogram and S is the non-noisy spectrum. This agrees with the intuition that the standard deviation of the spectral noise decreases with increasing number of samples. It should be noted that the standard deviation of the noise will be decreased if apodization is applied. The absolute value of the spectral samples $\sqrt{\mathrm{Re}(\hat{S}[k])^2 + \mathrm{Im}(\hat{S}[k])^2}$ can be described by the Rice distribution (Talukdar and Lawing, 1991), where the distribution in each spectral sample depends on the value of the non-noisy spectral sample. Let $\upsilon = S[k]$ be the mean distance of the real and imaginary part to the origin and let $\sigma = \sqrt{\frac{\overline{I}}{2N}}$ be the standard deviation of the real and imaginary part. Following Talukdar and Lawing (1991), the Rice distribution is defined by υ and σ and the mean is given by

$$\mu_{rice} = \sigma\sqrt{\frac{\pi}{2}}\,{}_1F_1\left(-\frac{1}{2}; 1; -\frac{\upsilon^2}{2\sigma^2}\right) \tag{A.8.5}$$

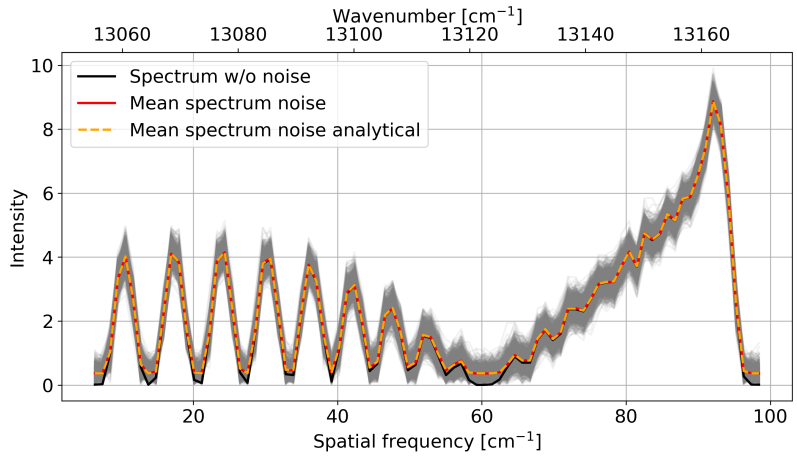

(a)

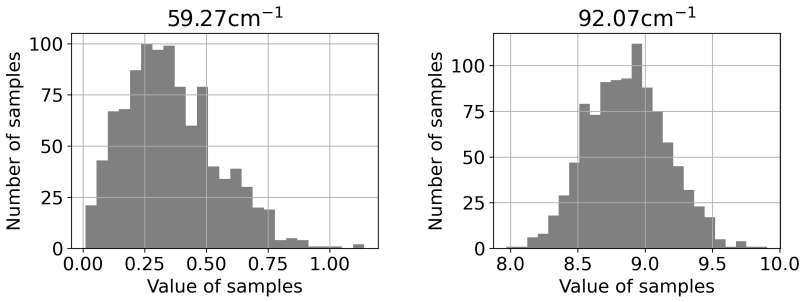

(b) (c)

Figure 7.10: (a) Absolute spectra for a low signal with a SNR of 20 and high temperature of 700K with (grey lines) and without (solid black line) shot noise; the mean of the noisy spectra (red solid line) and the analytical mean calculation following the mean of the Rice distribution defined in Eq. (A.8.5) (orange dashed line); (b) and (c) noise distribution at the minimal and maximal spectral sample at 59.27cm^{-1} and 92.07cm^{-1}, respectively;

where ${}_1F_1$ is the confluent hypergeometric function of the first kind. The standard deviation can be derived from the second moment, defined by

$$\sigma_{rice} = \sqrt{2\sigma^2} = \sqrt{\frac{\overline{I}}{N}}. \tag{A.8.6}$$

The derived theory is validated in a small simulation in Figure 7.10a, where absolute spectra for a low signal with an SNR of 20 and high temperature of 700K are shown. Note that Norton-Beer strong apodization is applied. One can see that the noisy spectra are centered around the non-noisy spectrum for high values but are off for low values. Figure 7.10c shows

that the noise distribution is close to a normal distribution for a high value but skewed for low values as shown in Figure 7.10b. Within the processing, the deviating mean is subtracted to at least center the noise distribution around the non-noisy spectrum, which reduces the bias. It should be noted that this affects only very low signals which are below the signal levels usually used within the processing.

A.9 Measurement error and a priori precision matrix

In this section, some guide lines are given for the generation of the measurement error and a priori precision matrix in Sec. A.9.1 and Sec. A.9.2, respectively, which are needed for the temperature retrieval.

A.9.1 Measurement error precision matrix

The measurement error precision matrix contains the measurement uncertainty governed by the spectral shot noise mentioned in Sec. 3.3. The noise is then propagated evenly into the spectrum as described in detail in Sec. A.8. Following Eq. (A.8.6), the spectral noise of an absolute spectrum for a given row k is given by $\sigma_k = \sqrt{\frac{\overline{I_k}}{N}}$, where $\overline{I_k}$ is the mean signal of that row and N is the number of spatial samples along the horizontal axis in the interferogram. The covariance matrix of the measurement error $\mathbf{S}_\epsilon \in \mathbb{R}^{M\times M}$ is then given by

$$\mathbf{S}_\epsilon = \begin{bmatrix} \mathbf{\Sigma}_1 & & \\ & \ddots & \\ & & \mathbf{\Sigma}_\mathrm{K} \end{bmatrix} \tag{A.9.1}$$

where K is the number of rows or tangent altitudes and $\mathbf{\Sigma}_\mathrm{k} \in \mathbb{R}^{L\times L}$ for $k = 1, .., K$ are diagonal block matrices defined by

$$\mathbf{\Sigma}_\mathrm{k} = \begin{bmatrix} \sigma_k & & \\ & \ddots & \\ & & \sigma_k \end{bmatrix} \tag{A.9.2}$$

where L is the number of samples in the spectral region of interest used in the retrieval process. Since $\mathbf{S}_\epsilon$ is a diagonal matrix, its inverse is also a diagonal matrix, where the diagonal entries are inverted.

A.9.2 A priori precision matrix

The a priori precision matrix can be seen as a linear operator weighting the influence of the a priori knowledge. Numerous approaches have been proposed for constructing the a priori precision matrix.

A popular way due its simplicity is given by Tikhonov and Arsenin (1977), where the a priori precision matrix is defined by

$$\mathbf{S}_{\mathrm{a}}^{-1} = \alpha_0^2 \mathbf{L}_0^T \mathbf{L}_0 + \alpha_1^2 \mathbf{L}_1^T \mathbf{L}_1, \tag{A.9.3}$$

where $\mathbf{L}_0 \in \mathbb{R}^{N \times N}$ and $\mathbf{L}_1 \in \mathbb{R}^{N \times N}$ denotes the zeroth- and first-order Tikhonov regularization matrices, respectively, and α_0 and α_1 the corresponding weighting factors. The $\mathbf{L}_0$ matrix is defined by the identity matrix, which scales the absolute difference between state parameters and a priori values. The $\mathbf{L}_1$ matrix is defined by

$$\mathbf{L}_1 = \begin{bmatrix} -1 & 1 & \dots & 0 & 0 \\ 0 & -1 & \dots & 0 & 0 \\ \vdots & \vdots & \ddots & \vdots & \vdots \\ 0 & 0 & \dots & -1 & 1 \\ 0 & 0 & \dots & 0 & 0 \end{bmatrix}. \tag{A.9.4}$$

It should be noted that $\mathbf{L}_1^T \mathbf{L}_1$ represents the central finite difference approximating the first derivative of the difference between the state parameters and a priori values. Tikhonov matrices representing higher derivatives can be set up analogously. The scaling factors can be seen as tuning parameters to govern the strength of the regularization. A large α_0 means that the retrieval result is drawn towards the a priori values. A large α_1 ensures a smooth result assuming that the a priori values are smooth, as it is the usual case. A second-order Tikhonov regularization is sometimes used to mitigate oscillation in retrieval results, as the second derivative of the differences will be decreased. The Tikhonov regularization, while effective, suffers from a significant drawback: the weighting factors α_0 and α_1 lack physical

meaning and scalability with respect to the number of state parameters. E.g. if a retrieval is performed with reduced vertical grid step size, the number of state parameters will be increased. This will increase the strength of the regularization since the regularization term, being essentially a sum, as presented in Eq. (3.25), is increased if the weighting factors are not adjusted accordingly.

The auto-regressive approach addresses this problem. Hereby, the covariance matrix of the differences between a priori and state parameters is described by a 1D exponential covariance denoted by

$$S_a(z, z') = \sigma \exp\left(\frac{\mid z - z' \mid}{c}\right), \tag{A.9.5}$$

where z and z' are the continuous representations of the vertical sample positions $\boldsymbol{z}$, σ denotes the expected standard deviation of the difference, while c refers to the correlation length. This approach thus incorporates the vertical grid size and gives the remaining parameters some physical meaning. The regularization term in Eq. (3.25) can be reformulated in a continuous form using a scalar product, denoted by

$$\langle f, f \rangle_{S_a^{-1}} = \int_{z_0}^{z_1} \int_{z_0}^{z_1} f(z) S_a^{-1}(z, z') f(z') dz' dz, \tag{A.9.6}$$

where z_0 and z_1 denote the boundaries of the vertical axis, and $f(z) = x_s(z) - x_a(z) \in L^2$ is a twice differentiable function defining the difference between state parameters and a priori values. Also here, x_s and x_a are the continuous representations of $\boldsymbol{x}_s$ and $\boldsymbol{x}_a$. Following Tarantola (2005) Sec. 7.21, Eq. (A.9.6) can be expressed as

$$\langle f, f \rangle_{S_a^{-1}} = \frac{1}{\sigma^2} \left(\int_{z_0}^{z_1} \frac{1}{c} f(z)^2 dz + \int_{z_0}^{z_1} c \left(\frac{\partial}{\partial z} f(z) \right)^2 dz \right). \tag{A.9.7}$$

To get an a priori precision matrix, the integrals in Eq. (A.9.7) are approximated by Riemann sums, resulting in a vector matrix multiplication, representing the regularization term in Eq. (3.25).

Let $\boldsymbol{z} \in \mathbb{R}^N$ be the vector of vertical sample positions. The first integral can then be

computed using the trapezoidal rule denoted by

$$\frac{1}{c\sigma^2}\int_{z_0}^{z_1} f(z)^2 dz \approx \frac{1}{c\sigma^2}\sum_{i=0}^{n-1}(\boldsymbol{z}_{i+1}-\boldsymbol{z}_i)\left(\frac{f(\boldsymbol{z}_{i+1})^2+f(\boldsymbol{z}_i)^2}{2}\right) \tag{A.9.8}$$

$$=: \boldsymbol{f}^T\mathbf{L}_0^T\mathbf{L}_0\boldsymbol{f}, \tag{A.9.9}$$

where $\boldsymbol{f} = (f(\boldsymbol{z}_i)) \in \mathbb{R}^N$ and $\mathbf{L}_0 \in \mathbb{R}^{N\times N}$ is defined by

$$\mathbf{L}_0 = \frac{\sqrt{h}}{\sigma\sqrt{c}}\begin{bmatrix} \sqrt{\frac{1}{2}} & 0 & \dots & & 0 \\ 0 & 1 & 0 & & \\ \vdots & & \ddots & & \vdots \\ & & 0 & 1 & 0 \\ 0 & & \dots & 0 & \sqrt{\frac{1}{2}} \end{bmatrix}, \tag{A.9.10}$$

where $h = \boldsymbol{z}_1 - \boldsymbol{z}_0$ and assuming that $\boldsymbol{z}$ is a equidistant discretization of z. The first order derivative in the second integral in Eq. (A.9.7) is approximated by the forward finite differences and left Riemann sum, respectively, given by

$$\frac{c}{\sigma^2}\int_{z_0}^{z_1} f'(x)^2 dx \approx \frac{c}{\sigma^2}\sum_{i=0}^{n-1}(\boldsymbol{z}_{i+1}-\boldsymbol{z}_i)\left(\frac{f(\boldsymbol{z}_{i+1})-f(\boldsymbol{z}_i)}{\boldsymbol{z}_{i+1}-\boldsymbol{z}_i}\right)^2 \tag{A.9.11}$$

$$= \frac{c}{\sigma^2}\sum_{i=0}^{n-1}\frac{\left(f(\boldsymbol{z}_{i+1})-f(\boldsymbol{z}_i)\right)^2}{\boldsymbol{z}_{i+1}-\boldsymbol{z}_i} \tag{A.9.12}$$

$$=: \boldsymbol{f}^T\mathbf{L}_1^T\mathbf{L}_1\boldsymbol{f}, \tag{A.9.13}$$

where $\mathbf{L}_1 \in \mathbb{R}^{N-1\times N}$ is defined by

$$\mathbf{L}_1 = \frac{\sqrt{c}}{\sigma\sqrt{h}}\begin{bmatrix} -1 & 1 & & \\ & \ddots & \ddots & \\ & & -1 & 1 \end{bmatrix}. \tag{A.9.14}$$

The regularization strength can be kept variable with altitude by supplying a σ for each altitude level, and/or by providing a c for each interval between altitude levels. Further, the whole discretization procedure can be applied to a non-regular vertical grid. Let the distance between the altitude levels be $\Delta \boldsymbol{z}_i = \frac{\boldsymbol{z}_{i+1} - \boldsymbol{z}_i}{c_i}$. The matrix $\mathbf{L}_0 \in \mathbb{R}^{N \times N}$ is then denoted by

$$\mathbf{L}_0 = \begin{bmatrix} \sigma_0^{-1} & & \\ & \ddots & \\ & & \sigma_n^{-1} \end{bmatrix} \begin{bmatrix} \sqrt{\frac{\Delta \boldsymbol{z}_0}{2}} & & & & \\ & \sqrt{\frac{\Delta \boldsymbol{z}_0 + \Delta \boldsymbol{z}_1}{2}} & & & \\ & & \ddots & & \\ & & & \sqrt{\frac{\Delta \boldsymbol{z}_{n-1} + \Delta \boldsymbol{z}_n}{2}} & \\ & & & & \sqrt{\frac{\Delta \boldsymbol{z}_n}{2}} \end{bmatrix} \tag{A.9.15}$$

and the matrix $\mathbf{L}_1 \in \mathbb{R}^{N-1 \times N}$ can be written as

$$\mathbf{L}_1 = \begin{bmatrix} \sigma_0^{-1} & & \\ & \ddots & \\ & & \sigma_n^{-1} \end{bmatrix} \begin{bmatrix} \sqrt{\Delta \boldsymbol{z}_0}^{-1} & & \\ & \ddots & \\ & & \sqrt{\Delta \boldsymbol{z}_{n-1}}^{-1} \end{bmatrix} \begin{bmatrix} -1 & 1 & & \\ & \ddots & \ddots & \\ & & -1 & 1 \end{bmatrix}. \tag{A.9.16}$$

The a priori precision matrix is then defined similar to the Tikhonov regularization by

$$\mathbf{S}_{\mathrm{a}}^{-1} = \alpha_0^2 \mathbf{L}_0^T \mathbf{L}_0 + \alpha_1^2 \mathbf{L}_1^T \mathbf{L}_1 \tag{A.9.17}$$

where α_0 and α_1 are scalars, weighting the strength of the regularization. However, these scalar parameters here serve only a fine tuning purpose and are not necessary as the standard deviation and correlation length are already incorporated into the $\mathbf{L}_0$ and $\mathbf{L}_1$ matrices.

A.10 Mathematical background on Barber's pole

Misalignment of the gratings introduces a frequency dependent rotation of the fringe pattern as shown in Sec. 4.3.3, entailing a vertical frequency component in the interferogram equation. The vertical frequency component denoted by $\alpha\sigma y$ in Eq. (4.4) can be mathematically shown, following the subsequent steps. It mainly involves the reflection of an incident ray by a rotated plane. In this context, the global coordinate system refers to a coordinate system which describes the direction of the incident ray. The local coordinate system refers to a coordinate system which is rotated by a misalignment angle of the grating such that the incident ray behaves as in the perfectly aligned case.

The unit vector of the incident ray $\boldsymbol{i}$ is transformed from the global to the local coordinate system using the inverse rotation matrix defined by the rotation angle β, denoted by

$$\boldsymbol{i}' = \mathbf{R}^{-1}(\beta)\boldsymbol{i}. \tag{A.10.1}$$

The ray is reflected across the local normal $\boldsymbol{n}'$ which results in the reflected ray in the local coordinates given by

$$\boldsymbol{r}' = \boldsymbol{i}' - 2(\boldsymbol{i}' \cdot \boldsymbol{n}')\boldsymbol{n}'. \tag{A.10.2}$$

The reflected ray is then transformed back into the global coordinate system using the rotation matrix

$$\boldsymbol{r} = \mathbf{R}(\beta)\boldsymbol{r}' \tag{A.10.3}$$

The rotation matrix for rotation around x-axis with angle χ is given by

$$\mathbf{R}_{\mathrm{x}}(\chi) = \begin{bmatrix} 1 & 0 & 0 \\ 0 & \cos\chi & -\sin\chi \\ 0 & \sin\chi & \cos\chi \end{bmatrix} \tag{A.10.4}$$

Recall that rotation matrices are orthogonal. Therefore, the inverse of rotation matrices are given by the transpose of the matrix. Thus, the inverse rotation matrix is given by

$$\mathbf{R}_{\mathrm{x}}^{-1}(\chi) = \begin{bmatrix} 1 & 0 & 0 \\ 0 & \cos\chi & \sin\chi \\ 0 & -\sin\chi & \cos\chi \end{bmatrix} \tag{A.10.5}$$

Applying the steps described in Eq. (A.10.1) to Eq. (A.10.3) for an incident ray onto grating 1 being parallel to the $\hat{z}$-axis, given by $\boldsymbol{i_1} = [0, 0, 1]^T$, the reflected ray is given by

$$\boldsymbol{r_1} = \begin{bmatrix} 0 \\ 2\cos(\chi)\sin(\chi) \\ 1 - 2\cos^2(\chi) \end{bmatrix}. \tag{A.10.6}$$

Using small angle approximation gives

$$\boldsymbol{r_1} = \begin{bmatrix} 0 \\ 2\chi \\ -1 \end{bmatrix}, \tag{A.10.7}$$

which demonstrates that the y-coordinate of the wave front is altered when comparing to the derivation of an ideal interferogram presented by Deiml (2018) in their Appendix B.2.1. The rotation matrix for rotation around $\hat{z}$-axis with angle ϕ is given by

$$\mathbf{R}_{\mathrm{z}}(\phi) = \begin{bmatrix} \cos\phi & -\sin\phi & 0 \\ \sin\phi & \cos\phi & 0 \\ 0 & 0 & 1 \end{bmatrix}. \tag{A.10.8}$$

Using again the transpose of the rotation matrix as its inverse and applying the steps described in Eq. (A.10.1) to Eq. (A.10.3) to an incident ray onto grating 2 being parallel to the x-axis, given by $\boldsymbol{i_2} = [1, 0, 0]^T$, the reflected ray is given by

$$\boldsymbol{r_2} = \begin{bmatrix} -1 \\ 2\cos(\phi)\sin(\phi) \\ 0 \end{bmatrix}. \tag{A.10.9}$$

Using small angle approximation gives

$$\boldsymbol{r_2} = \begin{bmatrix} -1 \\ 2\phi \\ 0 \end{bmatrix}, \tag{A.10.10}$$

which shows a similar alteration effect in the y-coordinate of the wave front as for grating 1. Following Deiml (2018) Appendix B.2.1, but including the tilt of the gratings into the wavefront vectors' y-coordinates, a monochromatic interferogram for a particular wavenumber is given by

$$I_\sigma(x,y) = \frac{1}{2}R(\sigma)(1+\cos(\boldsymbol{d}\cdot(\boldsymbol{k_1}-\boldsymbol{k_2}))) \tag{A.10.11}$$

where $\boldsymbol{d} = [x, y, 0]^T$ is the vector indicating the direction at the detector, and $\boldsymbol{k_1}$ and $\boldsymbol{k_2}$ describes the propagation of the two wave fronts, given by

$$\boldsymbol{k_1} = 2\pi\sigma \begin{bmatrix} 2\tan\theta_L \frac{\sigma-\sigma_L}{\sigma} \\ 2\chi \\ \cos\gamma_1 \end{bmatrix} \tag{A.10.12}$$

$$\boldsymbol{k_2} = 2\pi\sigma \begin{bmatrix} -2\tan\theta_L \frac{\sigma-\sigma_L}{\sigma} \\ 2\phi \\ \cos\gamma_2 \end{bmatrix}. \tag{A.10.13}$$

.

Inserting Eq. (A.10.12) and Eq. (A.10.13) into Eq. (A.10.11) gives

$$I_\sigma(x,y) = \frac{1}{2}R(\sigma)\left[1+\cos\left(\begin{bmatrix}x\\y\\0\end{bmatrix}\cdot 2\pi\sigma\begin{bmatrix}4\tan\theta_L\frac{\sigma-\sigma_L}{\sigma}\\2(\chi-\phi)\\\cos\gamma_1-\cos\gamma_2\end{bmatrix}\right)\right] \tag{A.10.14}$$

$$= \frac{1}{2}R(\sigma)\left[1+cos(2\pi(4\tan\theta_L(\sigma-\sigma_L)x+\alpha\sigma y))\right] \tag{A.10.15}$$

where $\alpha = 2(\chi-\phi)$.

A.11 Example of amplitude, baseline and visibility estimation from monochromatic measurements

In this section, additional examples of baseline, amplitude and visibility estimation from monochromatic interferograms are presented. These examples serve as supplementary material to the content discussed in Section 4.3.4.

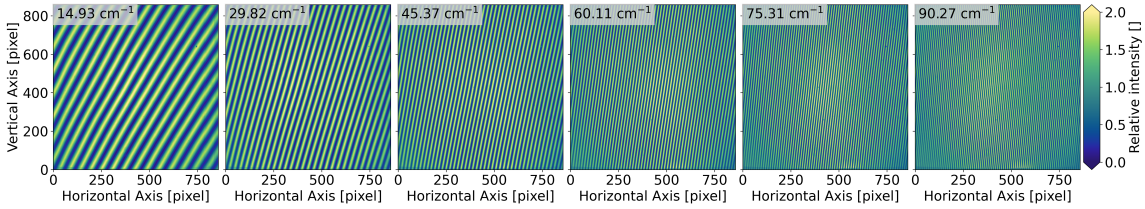

(a)

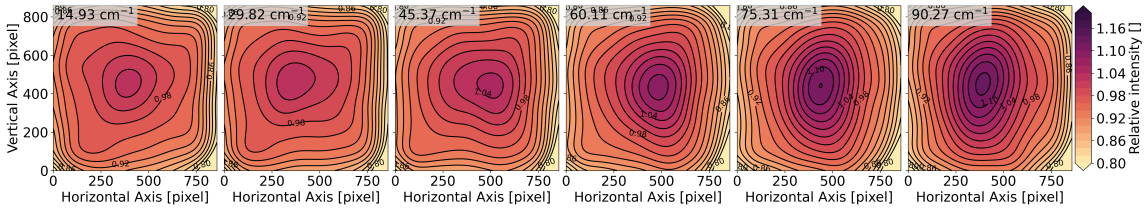

(b)

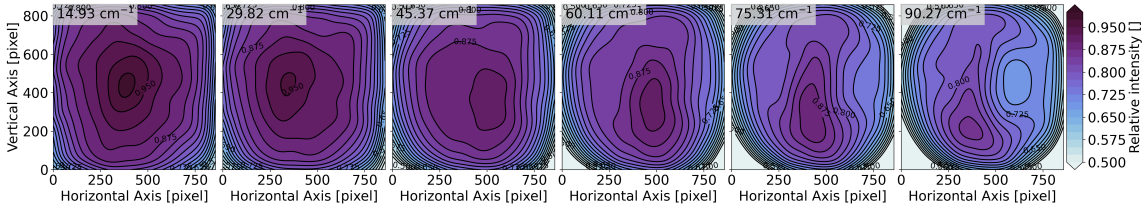

(c)

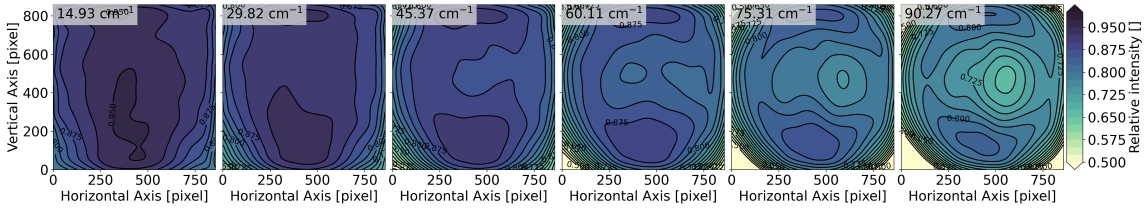

(d)

Figure 7.11: Baseline and amplitude estimation from monochromatic interferograms for instrument temperature at 0 °C for selected spatial frequencies equally distributed over the spectral range of the band pass filter; columns refer to the selected spatial frequencies and are indicated in the upper left corner of each subplot; (a) monochromatic interferogram; (b) baseline estimate; (c) amplitude estimate; (d) visibility estimate;

A.12 Effectiveness of baseline and amplitude estimation

A little example is presented to show that the 2D Savitzky-Golay filter is capable in estimating the baseline and amplitude correctly. Hereby, a monochromatic interferogram including baseline and amplitude variation is simulated. Subsequently, the 2D Savitzky-Golay filter is applied to estimate the baseline. The baseline is subtracted to eliminate the non-modulated part of the interferogram. The amplitude is estimated using the Hilbert transform along the horizontal axis, which is subsequently smoothed by a Savitzky-Golay filter as explained in Sec. 4.3.4.

The outcomes of this procedure are presented in Figure 7.12. Baseline and amplitude data employed for interferogram generation are extracted from a monochromatic calibration measurement, as depicted in Figures 7.12b and 7.12c, respectively. The resulting simulated

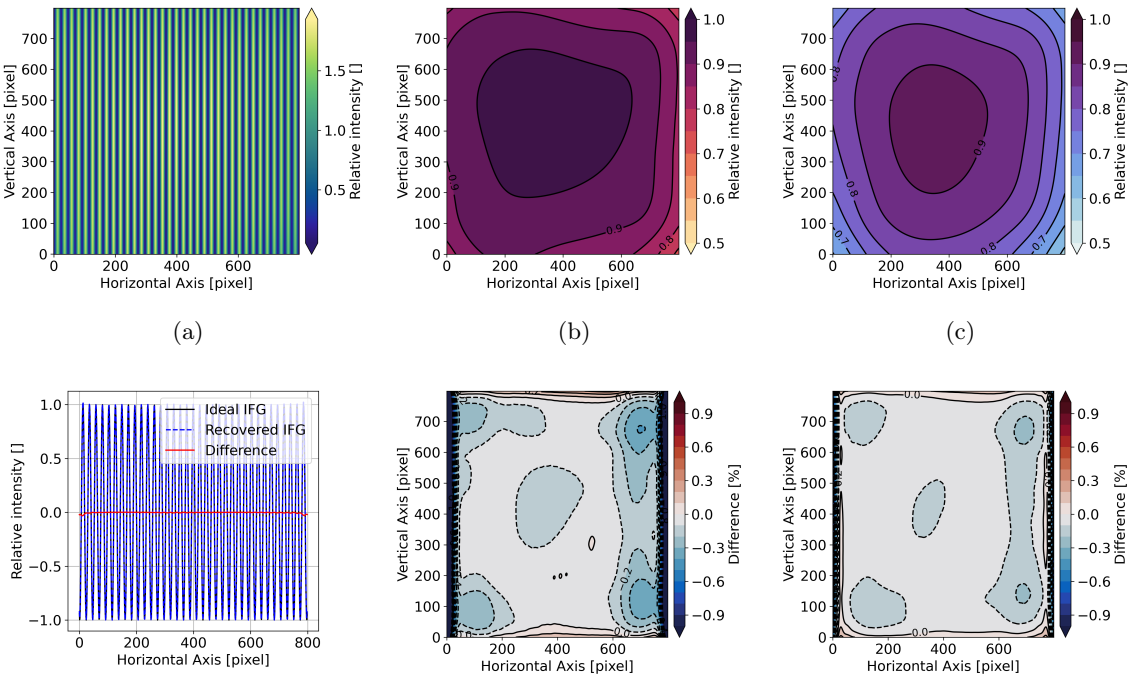

Figure 7.12: Example of baseline and amplitude estimation; (a) interferogram with (b) baseline and (c) amplitude variation for a spatial frequency of $40\,\mathrm{cm}^{-1}$; (d) comparison of ideal interferogram without baseline and amplitude variation and recovered interferogram after baseline and amplitude extraction and correction; difference of (e) baseline and (f) amplitude estimation to initial baseline and amplitude variation;

interferogram is displayed in Figure 7.12a. Employing the outlined process, baseline and amplitude estimation is achieved with an accuracy of less than 0.5 %, except at the image edges, as depicted in Figures 7.12e and 7.12f. It is important to note that a sufficiently large moving window for the Savitzky-Golay filter is necessary to eliminate the modulated part's wavy pattern. This, however, leads to larger errors at the edges due to data padding. A comparison between the ideal interferogram without variations and the recovered interferogram after correction reveals discrepancies primarily at the edges, as depicted in Figure 7.12d. To address this issue, it it recommended to apply the Savitzky-Golay filter to a larger region of interest and subsequently cut the edges to mitigate boundary effects. Additionally, it should be highlighted that employing a large window size increases the potential for smearing localized errors over a significant area. This can impact a considerable portion of the baseline and amplitude estimates.

A.13 Effectiveness of phase estimation

A little example is presented to assess the effectiveness of the phase estimation. Hereby, a monochromatic interferogram including spatial phase distortion is simulated. Subsequently, the phase is estimated following Sec. 4.3.5.

The outcomes of this procedure is presented in Fig. 7.13. The phase used in this simulation is extracted from a monochromatic calibration measurement depicted in Fig. 7.13b. The resulting simulated interferogram including spatial phase distortion is displayed in Fig. 7.13a. Using the above explained procedure, the phase estimation shows an error of less than 0.1 rad for most of the field.

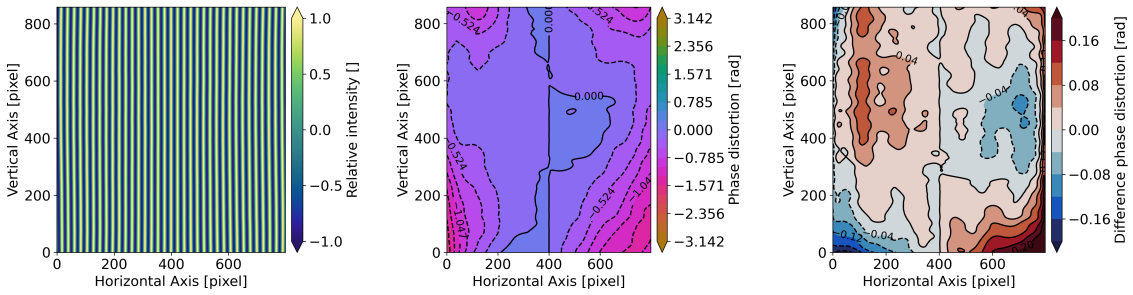

(a) (b) (c)

Figure 7.13: Example of phase estimation following Sec. 4.3.5; (a) interferogram with spatial phase distortion for spatial frequency of $40\,\mathrm{cm}^{-1}$; (b) initial phase distortion; (c) difference of phase estimation and initial phase;

Acknowledgments

I wish to begin by expressing my gratitude to Martin Riese for giving me the opportunity to collaborate at IEK-7. I appreciate the constructive discussions regarding my scientific findings and publications.

I also want to convey my profound appreciation to Jörn Ungermann and Martin Kaufmann for their invaluable mentorship and close guidance throughout the complex project. I am deeply thankful to both of them for the wealth of knowledge I have gained from their expertise.

Special thanks are due to Peter Preuße for fostering a pleasant working environment within our research group. His guidance in decision-making concerning journal and conference selections has been instrumental to my progress.

Furthermore, I would like to express my sincere gratitude to all my colleagues at IEK-7 and the Atmospheric Physics Department of Bergische Universität Wuppertal. Collaborating with them over the past three years has been an absolute delight.

Bibliography

M. J. Alexander and C. Barnet. Using Satellite Observations to Constrain Parameterizations of Gravity Wave Effects for Global Models. *Journal of the Atmospheric Sciences*, 64(5): 1652–1665, 2007. doi: 10.1175/JAS3897.1. URL https://journals.ametsoc.org/doi/10.1175/JAS3897.1.

M. J. Alexander, M. Geller, C. McLandress, S. Polavarapu, P. Preusse, F. Sassi, K. Sato, S. Eckermann, M. Ern, A. Hertzog, Y. Kawatani, M. Pulido, T. A. Shaw, M. Sigmond, R. Vincent, and S. Watanabe. Recent developments in gravity-wave effects in climate models and the global distribution of gravity-wave momentum flux from observations and models: Recent Developments in Gravity-Wave Effects. *Quarterly Journal of the Royal Meteorological Society*, 136(650):1103–1124, 2010. doi: 10.1002/qj.637. URL https://onlinelibrary.wiley.com/doi/10.1002/qj.637.

D. G. Andrews, J. R. Holton, and C. B. Leovy. *Middle atmosphere dynamics*. Number v. 40 in International geophysics series. Academic Press, Orlando, 1987. ISBN 978-0-12-058575-5.

C. Barnet, J. Blaisdell, and J. Susskind. Practical methods for rapid and accurate computation of interferometric spectra for remote sensing applications. *IEEE Transactions on Geoscience and Remote Sensing*, 38(1):169–183, 2000. doi: 10.1109/36.823910. URL http://ieeexplore.ieee.org/document/823910/.

C. A. Barth and A. F. Hildebrandt. The 5577 A airglow emission mechanism. *Journal of Geophysical Research*, 66(3):985–986, 1961. doi: 10.1029/JZ066i003p00985. URL http://doi.wiley.com/10.1029/JZ066i003p00985.

A. Ben-David and A. Ifarraguerri. Computation of a spectrum from a single-beam Fourier-transform infrared interferogram. *Applied Optics*, 41(6):1181, 2002. doi: 10.1364/AO.41.001181. URL https://opg.optica.org/abstract.cfm?URI=ao-41-6-1181.

C. D. Boone, S. D. McLeod, and P. F. Bernath. Apodization effects in the retrieval of volume mixing ratio profiles. *Applied Optics*, 41(6):1029, 2002. doi: 10.1364/AO.41.001029. URL https://opg.optica.org/abstract.cfm?URI=ao-41-6-1029.

M. Borgeaud, N. Scheidegger, M. Noca, G. Roethlisberger, F. Jordan, T. Choueiri, and N. Steiner. SwissCube: The First Entirely-Built Swiss Student Satellite with an Earth Observation Payload. In R. Sandau, H.-P. Roeser, and A. Valenzuela, editors, *Small Satellite Missions for Earth Observation*, pages 207–213. Springer Berlin Heidelberg, Berlin, Heidelberg, 2010. ISBN 978-3-642-03500-5. doi: 10.1007/978-3-642-03501-2_19. URL http://link.springer.com/10.1007/978-3-642-03501-2_19.

J. Bouwmeester and J. Guo. Survey of worldwide pico- and nanosatellite missions, distributions and subsystem technology. *Acta Astronautica*, 67(7-8):854–862, 2010. doi: 10.1016/j.actaastro.2010.06.004. URL https://linkinghub.elsevier.com/retrieve/pii/S0094576510001955.

G. Brasseur and S. Solomon. *Aeronomy of the middle atmosphere: chemistry and physics of the stratosphere and mesosphere*. Number v. 32 in Atmospheric and oceanographic sciences library. Springer, Dordrecht, Great Britain, 3rd rev. and enlarged ed edition, 2005. ISBN 978-1-4020-3284-4.

J. W. Brault. High precision fourier transform spectrometry: The critical role of phase corrections. *Mikrochimica Acta*, 93(1-6):215–227, 1987. doi: 10.1007/BF01201691. URL http://link.springer.com/10.1007/BF01201691.

A. Bucholtz, W. R. Skinner, V. J. Abreu, and P. B. Hays. The dayglow of the O_2 atmospheric band system. *Planetary and Space Science*, 34(11):1031–1035, 1986. doi: 10.1016/0032-0633(86)90013-9. URL https://www.sciencedirect.com/science/article/pii/0032063386900139.

J. Burrows, E. Hölzle, A. Goede, H. Visser, and W. Fricke. SCIAMACHY—scanning imaging absorption spectrometer for atmospheric chartography. *Acta Astronautica*, 35(7):445–451, 1995. doi: 10.1016/0094-5765(94)00278-T. URL https://linkinghub.elsevier.com/retrieve/pii/009457659400278T.

I. Campbell and C. Gray. Rate constants for O(^{3}P) recombination and association with N(^{4}S). *Chemical Physics Letters*, 18(4):607–609, 1973. doi: 10.1016/0009-2614(73)80479-8. URL https://linkinghub.elsevier.com/retrieve/pii/0009261473804798.

J. Cardon, C. Englert, J. Harlander, F. Roesler, and M. Stevens. SHIMMER on STS-112: Development and Proof-of-Concept Flight. In *AIAA Space 2003 Conference & Exposition*, Long Beach, California, 2003. American Institute of Aeronautics and Astronautics. ISBN 978-1-62410-103-8. doi: 10.2514/6.2003-6224. URL https://arc.aiaa.org/doi/10.2514/6.2003-6224.

Q. Chen. *Retrieval of atmospheric quantities from remote sensing measurements of nightglow emissions in the MLT region.* PhD thesis, Bergische Universität Wuppertal, 2020. ISBN: 9783958064850 OCLC: 1246167094.

Q. Chen, K. Ntokas, B. Linder, L. Krasauskas, M. Ern, P. Preusse, J. Ungermann, E. Becker, M. Kaufmann, and M. Riese. Satellite observations of gravity wave momentum flux in the mesosphere and lower thermosphere (MLT): feasibility and requirements. *Atmospheric Measurement Techniques*, 15(23):7071–7103, 2022. doi: 10.5194/amt-15-7071-2022. URL https://amt.copernicus.org/articles/15/7071/2022/.

P. Connes. Spectromètre interférentiel à sélection par l'amplitude de modulation. *Journal de Physique et le Radium*, 19(3):215–222, 1958. doi: 10.1051/jphysrad:01958001903021500. URL http://www.edpsciences.org/10.1051/jphysrad:01958001903021500.

M. Deiml. *Development of a Small Satellite Remote Sensing Payload for Passive Limb Sounding of the Atmospheric Oxygen Emission.* PhD thesis, University of Wuppertal, 2018.

C. R. Englert and J. M. Harlander. Flatfielding in spatial heterodyne spectroscopy. *Applied*

Optics, 45(19):4583, 2006. doi: 10.1364/AO.45.004583. URL https://www.osapublishing.org/abstract.cfm?URI=ao-45-19-4583.

C. R. Englert, J. M. Harlander, J. G. Cardon, and F. L. Roesler. Correction of phase distortion in spatial heterodyne spectroscopy. *Applied Optics*, 43(36):6680, 2004. doi: 10.1364/AO.43.006680. URL https://www.osapublishing.org/abstract.cfm?URI=ao-43-36-6680.

C. R. Englert, J. M. Harlander, C. M. Brown, K. D. Marr, I. J. Miller, J. E. Stump, J. Hancock, J. Q. Peterson, J. Kumler, W. H. Morrow, T. A. Mooney, S. Ellis, S. B. Mende, S. E. Harris, M. H. Stevens, J. J. Makela, B. J. Harding, and T. J. Immel. Michelson Interferometer for Global High-Resolution Thermospheric Imaging (MIGHTI): Instrument Design and Calibration. *Space Science Reviews*, 212(1-2):553–584, 2017. doi: 10.1007/s11214-017-0358-4. URL http://link.springer.com/10.1007/s11214-017-0358-4.

M. Ern. Absolute values of gravity wave momentum flux derived from satellite data. *Journal of Geophysical Research*, 109(D20):D20103, 2004. doi: 10.1029/2004JD004752. URL http://doi.wiley.com/10.1029/2004JD004752.

M. Ern, L. Hoffmann, and P. Preusse. Directional gravity wave momentum fluxes in the stratosphere derived from high-resolution AIRS temperature data: NET GRAVITY WAVE MOMENTUM FLUX FROM AIRS. *Geophysical Research Letters*, 44(1):475–485, 2017. doi: 10.1002/2016GL072007. URL http://doi.wiley.com/10.1002/2016GL072007.

E. J. Fetzer and J. C. Gille. Gravity Wave Variance in LIMS Temperatures. Part I: Variability and Comparison with Background Winds. *Journal of the Atmospheric Sciences*, 51(17):2461–2483, 1994. doi: 10.1175/1520-0469(1994)051<2461:GWVILT>2.0.CO;2. URL http://journals.ametsoc.org/doi/10.1175/1520-0469(1994)051<2461:GWVILT>2.0.CO;2.

A. S. Filler. Apodization and Interpolation in Fourier-Transform Spectroscopy*. *Journal of the Optical Society of America*, 54(6):762, 1964. doi: 10.1364/JOSA.54.000762. URL https://www.osapublishing.org/abstract.cfm?URI=josa-54-6-762.

A. Fitzgibbon. Simultaneous linear estimation of multiple view geometry and lens distortion. In *Proceedings of the 2001 IEEE Computer Society Conference on Computer Vision and*

Pattern Recognition. CVPR 2001, volume 1, pages I–125–I–132, Kauai, HI, USA, 2001. IEEE Comput. Soc. doi: 10.1109/CVPR.2001.990465. URL http://ieeexplore.ieee.org/document/990465/.

J. Florczak, T. Neubert, K. El Maghawry, E. Zimmermann, H. Rongen, M. Kaufmann, F. Olschewski, and S. Van Waasen. Radiation Monitor Extension for CMOS Imaging Instruments in Nanosatellites. *IEEE Transactions on Nuclear Science*, 69(7):1651–1658, 2022a. doi: 10.1109/TNS.2022.3144784. URL https://ieeexplore.ieee.org/document/9686712/.

J. Florczak, K. Ntokas, T. Neubert, E. Zimmermann, H. Rongen, U. Clemens, M. Kaufmann, M. Riese, and S. van Waasen. Bad pixel detection for on-board data quality improvement of remote sensing instruments in CubeSats. In C. D. Norton and S. R. Babu, editors, *CubeSats and SmallSats for Remote Sensing VI*, page 3, San Diego, United States, 2022b. SPIE. doi: 10.1117/12.2633124. URL https://www.spiedigitallibrary.org/conference-proceedings-of-spie/12236/2633124/Bad-pixel-detection-for-on-board-data-quality-improvement-of/10.1117/12.2633124.full.

G. B. Folland and A. Sitaram. The uncertainty principle: A mathematical survey. *The Journal of Fourier Analysis and Applications*, 3(3):207–238, 1997. doi: 10.1007/BF02649110. URL http://link.springer.com/10.1007/BF02649110.

M. L. Forman, W. H. Steel, and G. A. Vanasse. Correction of Asymmetric Interferograms Obtained in Fourier Spectroscopy*. *Journal of the Optical Society of America*, 56(1):59, 1966. doi: 10.1364/JOSA.56.000059. URL https://www.osapublishing.org/abstract.cfm?URI=josa-56-1-59.

D. C. Fritts and M. J. Alexander. Gravity wave dynamics and effects in the middle atmosphere: MIDDLE ATMOSPHERE GRAVITY WAVE DYNAMICS. *Reviews of Geophysics*, 41(1), 2003. doi: 10.1029/2001RG000106. URL http://doi.wiley.com/10.1029/2001RG000106.

A. Galli, S. Guerlet, A. Butz, I. Aben, H. Suto, A. Kuze, N. M. Deutscher, J. Notholt,

D. Wunch, P. O. Wennberg, D. W. T. Griffith, O. Hasekamp, and J. Landgraf. The impact of spectral resolution on satellite retrieval accuracy of CO_2 and CH_4. *Atmospheric Measurement Techniques*, 7(4):1105–1119, 2014. doi: 10.5194/amt-7-1105-2014. URL `https://amt.copernicus.org/articles/7/1105/2014/`.

R. R. Gamache, B. Vispoel, M. Rey, A. Nikitin, V. Tyuterev, O. Egorov, I. E. Gordon, and V. Boudon. Total internal partition sums for the HITRAN2020 database. *Journal of Quantitative Spectroscopy and Radiative Transfer*, 271:107713, 2021. doi: 10.1016/j.jqsrt.2021.107713. URL `https://linkinghub.elsevier.com/retrieve/pii/S0022407321002065`.

J. Gille, J. Barnett, P. Arter, M. Barker, P. Bernath, C. Boone, C. Cavanaugh, J. Chow, M. Coffey, J. Craft, C. Craig, M. Dials, V. Dean, T. Eden, D. P. Edwards, G. Francis, C. Halvorson, L. Harvey, C. Hepplewhite, R. Khosravi, D. Kinnison, C. Krinsky, A. Lambert, H. Lee, L. Lyjak, J. Loh, W. Mankin, S. Massie, J. McInerney, J. Moorhouse, B. Nardi, D. Packman, C. Randall, J. Reburn, W. Rudolf, M. Schwartz, J. Serafin, K. Stone, B. Torpy, K. Walker, A. Waterfall, R. Watkins, J. Whitney, D. Woodard, and G. Young. High Resolution Dynamics Limb Sounder: Experiment overview, recovery, and validation of initial temperature data. *Journal of Geophysical Research*, 113(D16):D16S43, 2008. doi: 10.1029/2007JD008824. URL `http://doi.wiley.com/10.1029/2007JD008824`.

M. Gisi, F. Hase, S. Dohe, T. Blumenstock, A. Simon, and A. Keens. XCO_2-measurements with a tabletop FTS using solar absorption spectroscopy. *Atmospheric Measurement Techniques*, 5(11):2969–2980, 2012. doi: 10.5194/amt-5-2969-2012. URL `https://amt.copernicus.org/articles/5/2969/2012/`.

I. Gordon, L. Rothman, R. Hargreaves, R. Hashemi, E. Karlovets, F. Skinner, E. Conway, C. Hill, R. Kochanov, Y. Tan, P. Wcisło, A. Finenko, K. Nelson, P. Bernath, M. Birk, V. Boudon, A. Campargue, K. Chance, A. Coustenis, B. Drouin, J. Flaud, R. Gamache, J. Hodges, D. Jacquemart, E. Mlawer, A. Nikitin, V. Perevalov, M. Rotger, J. Tennyson, G. Toon, H. Tran, V. Tyuterev, E. Adkins, A. Baker, A. Barbe, E. Canè, A. Császár, A. Dudaryonok, O. Egorov, A. Fleisher, H. Fleurbaey, A. Foltynowicz, T. Furtenbacher, J. Harrison, J. Hartmann, V. Horneman, X. Huang, T. Karman, J. Karns, S. Kassi,

I. Kleiner, V. Kofman, F. Kwabia–Tchana, N. Lavrentieva, T. Lee, D. Long, A. Lukashevskaya, O. Lyulin, V. Makhnev, W. Matt, S. Massie, M. Melosso, S. Mikhailenko, D. Mondelain, H. Müller, O. Naumenko, A. Perrin, O. Polyansky, E. Raddaoui, P. Raston, Z. Reed, M. Rey, C. Richard, R. Tóbiás, I. Sadiek, D. Schwenke, E. Starikova, K. Sung, F. Tamassia, S. Tashkun, J. Vander Auwera, I. Vasilenko, A. Vigasin, G. Villanueva, B. Vispoel, G. Wagner, A. Yachmenev, and S. Yurchenko. The HITRAN2020 molecular spectroscopic database. *Journal of Quantitative Spectroscopy and Radiative Transfer*, 277: 107949, 2022. doi: 10.1016/j.jqsrt.2021.107949. URL `https://linkinghub.elsevier.com/retrieve/pii/S0022407321004416`.

B. G. Gowri, V. Hariharan, S. Thara, V. Sowmya, S. S. Kumar, and K. P. Soman. 2D Image data approximation using Savitzky Golay filter - Smoothing and differencing. In *2013 International Mutli-Conference on Automation, Computing, Communication, Control and Compressed Sensing (iMac4s)*, pages 365–371, Kottayam, India, 2013. IEEE. doi: 10.1109/iMac4s.2013.6526438. URL `http://ieeexplore.ieee.org/document/6526438/`.

J. G. Green, J. Shi, and J. R. Barker. Photochemical Kinetics of Vibrationally Excited Ozone Produced in the 248 nm Photolysis of O_2/O_3 Mixtures. *The Journal of Physical Chemistry A*, 104(26):6218–6226, 2000. doi: 10.1021/jp000635k. URL `https://doi.org/10.1021/jp000635k`.

P. R. Griffiths and J. A. De Haseth. *Fourier transform infrared spectrometry.* Wiley-Interscience, Hoboken, N.J., 2nd ed edition, 2007. ISBN 978-0-470-10629-7.

J. Gumbel, L. Megner, O. M. Christensen, N. Ivchenko, D. P. Murtagh, S. Chang, J. Dillner, T. Ekebrand, G. Giono, A. Hammar, J. Hedin, B. Karlsson, M. Krus, A. Li, S. McCallion, G. Olentšenko, S. Pak, W. Park, J. Rouse, J. Stegman, and G. Witt. The MATS satellite mission – gravity wave studies by Mesospheric Airglow/Aerosol Tomography and Spectroscopy. *Atmospheric Chemistry and Physics*, 20(1):431–455, 2020. doi: 10.5194/acp-20-431-2020. URL `https://acp.copernicus.org/articles/20/431/2020/`.

A. Gupta, T. Birner, A. Dörnbrack, and I. Polichtchouk. Importance of Gravity Wave Forc-

ing for Springtime Southern Polar Vortex Breakdown as Revealed by ERA5. *Geophysical Research Letters*, 48(10):e2021GL092762, 2021. doi: 10.1029/2021GL092762. URL https://agupubs.onlinelibrary.wiley.com/doi/10.1029/2021GL092762.

J. Harlander, R. J. Reynolds, and F. L. Roesler. Spatial heterodyne spectroscopy for the exploration of diffuse interstellar emission lines at far-ultraviolet wavelengths. *The Astrophysical Journal*, 396:730, 1992. doi: 10.1086/171756. URL http://adsabs.harvard.edu/doi/10.1086/171756.

F. Harris. On the use of windows for harmonic analysis with the discrete Fourier transform. *Proceedings of the IEEE*, 66(1):51–83, 1978. doi: 10.1109/PROC.1978.10837. URL http://ieeexplore.ieee.org/document/1455106/.

H. Heidt, J. Puig-Suari, A. S. Moore, S. Nakasuka, and R. J. Twiggs. Cubesat: A new generation of picosatellite for education and industry low-cost space experimentation. Logan, USA, 2000. 14th Annual/USU Conference on Small Satellites.

N. P. Hindley, C. J. Wright, N. D. Smith, and N. J. Mitchell. The southern stratospheric gravity wave hot spot: individual waves and their momentum fluxes measured by COSMIC GPS-RO. *Atmospheric Chemistry and Physics*, 15(14):7797–7818, 2015. doi: 10.5194/acp-15-7797-2015. URL https://acp.copernicus.org/articles/15/7797/2015/.

L. Hoffmann and M. J. Alexander. Retrieval of stratospheric temperatures from Atmospheric Infrared Sounder radiance measurements for gravity wave studies. *Journal of Geophysical Research*, 114(D7):D07105, 2009. doi: 10.1029/2008JD011241. URL http://doi.wiley.com/10.1029/2008JD011241.

J. R. Holton, P. H. Haynes, M. E. McIntyre, A. R. Douglass, R. B. Rood, and L. Pfister. Stratosphere-troposphere exchange. *Reviews of Geophysics*, 33(4):403–439, 1995. doi: 10.1029/95RG02097. URL https://agupubs.onlinelibrary.wiley.com/doi/10.1029/95RG02097.

F. T. Huang, H. G. Mayr, C. A. Reber, J. M. Russell, M Mlynczak, and J. G. Mengel. Stratospheric and mesospheric temperature variations for the quasi-biennial and semiannual

(QBO and SAO) oscillations based on measurements from SABER (TIMED) and MLS (UARS). *Annales Geophysicae*, 24(8):2131–2149, 2006. doi: 10.5194/angeo-24-2131-2006. URL https://angeo.copernicus.org/articles/24/2131/2006/.

J. Humlíček. Optimized computation of the voigt and complex probability functions. *Journal of Quantitative Spectroscopy and Radiative Transfer*, 27(4):437–444, 1982. doi: 10.1016/0022-4073(82)90078-4. URL https://linkinghub.elsevier.com/retrieve/pii/0022407382900784.

D. G. Johnson, W. A. Traub, and K. W. Jucks. Phase determination from mostly one-sided interferograms. *Applied Optics*, 35(16):2955, 1996. doi: 10.1364/AO.35.002955. URL https://opg.optica.org/abstract.cfm?URI=ao-35-16-2955.

J. Kaiser and R. Schafer. On the Use of the I_0-Sinh Window for Spectrum Analysis. *IEEE Transactions on Acoustics, Speech, and Signal Processing*, 28(1):105–107, 1980. doi: 10.1109/TASSP.1980.1163349. URL http://ieeexplore.ieee.org/document/1163349/.

M. Kaufmann, F. Olschewski, K. Mantel, B. Solheim, G. Shepherd, M. Deiml, J. Liu, R. Song, Q. Chen, O. Wroblowski, D. Wei, Y. Zhu, F. Wagner, F. Loosen, D. Froehlich, T. Neubert, H. Rongen, P. Knieling, P. Toumpas, J. Shan, G. Tang, R. Koppmann, and M. Riese. A highly miniaturized satellite payload based on a spatial heterodyne spectrometer for atmospheric temperature measurements in the mesosphere and lower thermosphere. *Atmospheric Measurement Techniques*, 11(7):3861–3870, 2018. doi: 10.5194/amt-11-3861-2018. URL https://amt.copernicus.org/articles/11/3861/2018/.

M. Kaufmann, K. Ntokas, D. Sivil, B. Michel, Q. Chen, F. Olschewski, O. Wroblowski, T. Augspurger, M. Miebach, J. Ungermann, T. Neubert, K. Mantel, and M. Riese. Optical design and straylight analyses of a spatial heterodyne interferometer for the measurement of atmospheric temperature from space. page 7, San Diego, United States, 2023. SPIE. doi: 10.1117/12.2677600. URL https://www.spiedigitallibrary.org/conference-proceedings-of-spie/12689/2677600/

Optical-design-and-straylight-analyses-of-a-spatial-heterodyne-interferometer/10.1117/12.2677600.full.

A. Kleinert, F. Friedl-Vallon, T. Guggenmoser, M. Höpfner, T. Neubert, R. Ribalda, M. K. Sha, J. Ungermann, J. Blank, A. Ebersoldt, E. Kretschmer, T. Latzko, H. Oelhaf, F. Olschewski, and P. Preusse. Level 0 to 1 processing of the imaging Fourier transform spectrometer GLORIA: generation of radiometrically and spectrally calibrated spectra. *Atmospheric Measurement Techniques*, 7(12):4167–4184, 2014. doi: 10.5194/amt-7-4167-2014. URL https://amt.copernicus.org/articles/7/4167/2014/.

J. Langille, D. Letros, D. Zawada, A. Bourassa, D. Degenstein, and B. Solheim. Spatial Heterodyne Observations of Water (SHOW) vapour in the upper troposphere and lower stratosphere from a high altitude aircraft: Modelling and sensitivity analysis. *Journal of Quantitative Spectroscopy and Radiative Transfer*, 209:137–149, 2018. doi: 10.1016/j.jqsrt.2018.01.026. URL https://linkinghub.elsevier.com/retrieve/pii/S0022407317309196.

J. Langille, D. Letros, A. Bourassa, B. Solheim, D. Degenstein, F. Dupont, D. Zawada, and N. D. Lloyd. Spatial heterodyne observations of water (SHOW) from a high-altitude airplane: characterization, performance, and first results. *Atmospheric Measurement Techniques*, 12(1):431–455, 2019. doi: 10.5194/amt-12-431-2019. URL https://amt.copernicus.org/articles/12/431/2019/.

R. Learner. Phase correction of emission line fourier transform spectra. *Journal of the Optical Society of America A: Optics and Image Science, and Vision*, 12(10):2165, 1995.

T. Lindeberg. Scale Selection Properties of Generalized Scale-Space Interest Point Detectors. *Journal of Mathematical Imaging and Vision*, 46(2):177–210, 2013. doi: 10.1007/s10851-012-0378-3. URL https://link.springer.com/10.1007/s10851-012-0378-3.

J. Liu, D. Wei, O. Wroblowski, Q. Chen, K. Mantel, F. Olschewski, M. Kaufmann, and M. Riese. Analysis and correction of distortions in a spatial heterodyne spectrometer system. *Applied Optics*, 58(9):2190, 2019. doi: 10.1364/AO.58.002190. URL https://www.osapublishing.org/abstract.cfm?URI=ao-58-9-2190.

X. Liu, J. Yue, J. Xu, L. Wang, W. Yuan, J. M. Russell, and M. E. Hervig. Gravity wave variations in the polar stratosphere and mesosphere from SOFIE/AIM temperature observations. *Journal of Geophysical Research: Atmospheres*, 119(12):7368–7381, 2014. doi: 10.1002/2013JD021439. URL `http://doi.wiley.com/10.1002/2013JD021439`.

E. J. Llewellyn, N. D. Lloyd, D. A. Degenstein, R. L. Gattinger, S. V. Petelina, A. E. Bourassa, J. T. Wiensz, E. V. Ivanov, I. C. McDade, B. H. Solheim, J. C. McConnell, C. S. Haley, C. Von Savigny, C. E. Sioris, C. A. McLinden, E. Griffioen, J. Kaminski, W. F. Evans, E. Puckrin, K. Strong, V. Wehrle, R. H. Hum, D. J. Kendall, J. Matsushita, D. P. Murtagh, S. Brohede, J. Stegman, G. Witt, G. Barnes, W. F. Payne, L. Piché, K. Smith, G. Warshaw, D. L. Deslauniers, P. Marchand, E. H. Richardson, R. A. King, I. Wevers, W. McCreath, E. Kyrölä, L. Oikarinen, G. W. Leppelmeier, H. Auvinen, G. Mégie, A. Hauchecorne, F. Lefèvre, J. De La Nöe, P. Ricaud, U. Frisk, F. Sjoberg, F. Von Schéele, and L. Nordh. The OSIRIS instrument on the Odin spacecraft. *Canadian Journal of Physics*, 82(6):411–422, 2004. doi: 10.1139/p04-005. URL `http://www.nrcresearchpress.com/doi/10.1139/p04-005`.

H. Luo, X. Fang, and B. Ertas. Hilbert Transform and Its Engineering Applications. *AIAA Journal*, 47(4):923–932, 2009. doi: 10.2514/1.37649. URL `https://arc.aiaa.org/doi/10.2514/1.37649`.

M. López-Puertas and F. W. Taylor. *Non-LTE radiative transfer in the atmosphere*. Number 3 in Series on atmospheric, oceanic and planetary physics. World Scientific, Singapore, 2001. ISBN 978-981-02-4566-5.

I. C. McDade, D. P. Murtagh, R. G. H. Greer, P. H. G. Dickinson, G. Witt, J. Stegman, E. J. Llewellyn, L. Thomas, and D. B. Jenkins. ETON 2: Quenching parameters for the proposed precursors of $O_2(b^1\Sigma_g^+)$ and $O(^1S)$ in the terrestrial nightglow. *Planetary and Space Science*, 34(9):789–800, 1986. doi: 10.1016/0032-0633(86)90075-9. URL `https://www.sciencedirect.com/science/article/pii/0032063386900759`.

C. McLandress, M. J. Alexander, and D. L. Wu. Microwave Limb Sounder observations of

gravity waves in the stratosphere: A climatology and interpretation. *Journal of Geophysical Research: Atmospheres*, 105(D9):11947–11967, 2000. doi: 10.1029/2000JD900097. URL http://doi.wiley.com/10.1029/2000JD900097.

C. A. McLinden, A. E. Bourassa, S. Brohede, M. Cooper, D. A. Degenstein, W. J. F. Evans, R. L. Gattinger, C. S. Haley, E. J. Llewellyn, N. D. Lloyd, P. Loewen, R. V. Martin, J. C. McConnell, I. C. McDade, D. Murtagh, L. Rieger, C. Von Savigny, P. E. Sheese, C. E. Sioris, B. Solheim, and K. Strong. OSIRIS: A Decade of Scattered Light. *Bulletin of the American Meteorological Society*, 93(12):1845–1863, 2012. doi: 10.1175/BAMS-D-11-00135.1. URL https://journals.ametsoc.org/doi/10.1175/BAMS-D-11-00135.1.

D. Murtagh, G. Witt, J. Stegman, I. McDade, E. Llewellyn, F. Harris, and R. Greer. An assessment of proposed O(^{1}S) and $O_2(b^1\Sigma_g^+)$ nightglow excitation parameters. *Planetary and Space Science*, 38(1):43–53, 1990. doi: 10.1016/0032-0633(90)90004-A. URL https://linkinghub.elsevier.com/retrieve/pii/003206339090004A.

D. A. Naylor and M. K. Tahic. Apodizing functions for Fourier transform spectroscopy. *Journal of the Optical Society of America A*, 24(11):3644, 2007. doi: 10.1364/JOSAA.24.003644. URL https://www.osapublishing.org/abstract.cfm?URI=josaa-24-11-3644.

R. H. Norton and R. Beer. New apodizing functions for Fourier spectrometry. *Journal of the Optical Society of America*, 66(3):259, 1976. doi: 10.1364/JOSA.66.000259. URL https://www.osapublishing.org/abstract.cfm?URI=josa-66-3-259.

R. H. Norton and R. Beer. Errata: New Apodizing Functions For Fourier Spectrometry. *Journal of the Optical Society of America*, 67(3):419, 1977. doi: 10.1364/JOSA.67.000419. URL https://opg.optica.org/abstract.cfm?URI=josa-67-3-419.

K. Ntokas, M. Kaufmann, J. Ungermann, P. Preusse, and M. Riese. Retrieval of gravity wave parameters using half interferograms measured by CubeSats. page 9, San Diego, United States, 2022. SPIE. doi: 10.1117/12.2633460. URL https://www.spiedigitallibrary.org/conference-proceedings-of-spie/12236/2633460/

Retrieval-of-gravity-wave-parameters-using-half-interferograms-measured-by/10.1117/12.2633460.full.

K. Ntokas, J. Ungermann, M. Kaufmann, T. Neubert, and M. Riese. Observation of horizontal temperature variations by a spatial heterodyne interferometer using single-sided interferograms. *Atmospheric Measurement Techniques*, 16(22):5681–5696, Nov. 2023a. ISSN 1867-8548. doi: 10.5194/amt-16-5681-2023. URL https://amt.copernicus.org/articles/16/5681/2023/.

K. F. F. Ntokas. Norton-Beer apodization python package, 2023. URL https://github.com/konstntokas/norton_beer.

K. F. F. Ntokas, J. Ungermann, and M. Kaufmann. Norton-Beer apodization and its Fourier transform. *Journal of the Optical Society of America A*, 40(11):2026, 2023b. doi: 10.1364/JOSAA.501593. URL https://opg.optica.org/abstract.cfm?URI=josaa-40-11-2026.

H. Nyquist. Certain Topics in Telegraph Transmission Theory. *Transactions of the American Institute of Electrical Engineers*, 47(2):617–644, 1928. doi: 10.1109/T-AIEE.1928.5055024. URL http://ieeexplore.ieee.org/document/5055024/.

D. Offermann, K.-U. Grossmann, P. Barthol, P. Knieling, M. Riese, and R. Trant. Cryogenic Infrared Spectrometers and Telescopes for the Atmosphere (CRISTA) experiment and middle atmosphere variability. *Journal of Geophysical Research: Atmospheres*, 104(D13): 16311–16325, 1999. doi: 10.1029/1998JD100047. URL http://doi.wiley.com/10.1029/1998JD100047.

F. Olschewski, M. Kaufmann, K. Mantel, M. Riese, and R. Koppmann. A novel CubeSat payload for airglow measurements in the mesosphere and lower thermosphere. page 2, San Diego, United States, 2018. SPIE. doi: 10.1117/12.2320998. URL https://www.spiedigitallibrary.org/conference-proceedings-of-spie/10769/2320998/A-novel-CubeSat-payload-for-airglow-measurements-in-the-mesosphere/10.1117/12.2320998.full.

D. A. Ortland, P. B. Hays, W. R. Skinner, and J.-H. Yee. Remote sensing of mesospheric temperature and $O_2(^1\Sigma)$ band volume emission rates with the high-resolution Doppler imager. *Journal of Geophysical Research: Atmospheres*, 103(D2):1821–1835, 1998. doi: 10.1029/97JD02794. URL `http://doi.wiley.com/10.1029/97JD02794`.

A. Poghosyan and A. Golkar. CubeSat evolution: Analyzing CubeSat capabilities for conducting science missions. *Progress in Aerospace Sciences*, 88:59–83, 2017. doi: 10.1016/j.paerosci.2016.11.002. URL `https://linkinghub.elsevier.com/retrieve/pii/S0376042116300951`.

P. Preusse, A. Dörnbrack, S. D. Eckermann, M. Riese, B. Schaeler, J. T. Bacmeister, D. Broutman, and K. U. Grossmann. Space-based measurements of stratospheric mountain waves by CRISTA 1. Sensitivity, analysis method, and a case study. *Journal of Geophysical Research: Atmospheres*, 107(D23):CRI 6–1–CRI 6–23, 2002. doi: 10.1029/2001JD000699. URL `http://doi.wiley.com/10.1029/2001JD000699`.

P. Preusse, M. Ern, S. D. Eckermann, C. D. Warner, R. H. Picard, P. Knieling, M. Krebsbach, J. M. Russell, M. G. Mlynczak, C. J. Mertens, and M. Riese. Tropopause to mesopause gravity waves in August: Measurement and modeling. *Journal of Atmospheric and Solar-Terrestrial Physics*, 68(15):1730–1751, 2006. doi: 10.1016/j.jastp.2005.10.019. URL `https://linkinghub.elsevier.com/retrieve/pii/S1364682606001568`.

P. Preusse, S. D. Eckermann, and M. Ern. Transparency of the atmosphere to short horizontal wavelength gravity waves. *Journal of Geophysical Research*, 113(D24):D24104, 2008. doi: 10.1029/2007JD009682. URL `http://doi.wiley.com/10.1029/2007JD009682`.

P. Preusse, S. Schroeder, L. Hoffmann, M. Ern, F. Friedl-Vallon, J. Ungermann, H. Oelhaf, H. Fischer, and M. Riese. New perspectives on gravity wave remote sensing by spaceborne infrared limb imaging. *Atmospheric Measurement Techniques*, 2(1):299–311, 2009. doi: 10.5194/amt-2-299-2009. URL `https://amt.copernicus.org/articles/2/299/2009/`.

T. Reddmann and R. Uhl. The H Lyman-α actinic flux in the middle atmosphere. *Atmos. Chem. Phys.*, page 7, 2003.

K. Ritter and T. Wilkerson. High-resolution spectroscopy of the oxygen A band. *Journal of Molecular Spectroscopy*, 121(1):1–19, 1987. doi: 10.1016/0022-2852(87)90167-6. URL https://linkinghub.elsevier.com/retrieve/pii/0022285287901676.

C. Rocken, R. Anthes, M. Exner, D. Hunt, S. Sokolovskiy, R. Ware, M. Gorbunov, W. Schreiner, D. Feng, B. Herman, Y.-H. Kuo, and X. Zou. Analysis and validation of GPS/MET data in the neutral atmosphere. *Journal of Geophysical Research: Atmospheres*, 102(D25):29849–29866, 1997. doi: 10.1029/97JD02400. URL http://doi.wiley.com/10.1029/97JD02400.

C. D. Rodgers. *Inverse Methods for Atmospheric Sounding: Theory and Practice*, volume 2 of *Series on Atmospheric, Oceanic and Planetary Physics*. WORLD SCIENTIFIC, 2000. doi: 10.1142/3171. URL https://www.worldscientific.com/worldscibooks/10.1142/3171.

F. L. Roesler and J. M. Harlander. Spatial heterodyne spectroscopy: interferometric performance at any wavelength without scanning. page 234, Los Cruces, NM, 1990. doi: 10.1117/12.22119. URL http://proceedings.spiedigitallibrary.org/proceeding.aspx?doi=10.1117/12.22119.

L. S. Rothman, I. E. Gordon, Y. Babikov, A. Barbe, D. C. Benner, P. F. Bernath, M. Birk, L. Bizzocchi, V. Boudon, L. R. Brown, A. Campargue, K. Chance, E. A. Cohen, L. H. Coudert, V. M. Devi, B. J. Drouin, A. Fayt, J.-M. Flaud, R. R. Gamache, J. J. Harrison, J.-M. Hartmann, C. Hill, J. T. Hodges, D. Jacquemart, A. Jolly, J. Lamouroux, R. J. L. Roy, G. Li, D. A. Long, O. M. Lyulin, C. J. Mackie, S. T. Massie, S. Mikhailenko, H. S. P. Müller, O. V. Naumenko, A. V. Nikitin, J. Orphal, V. Perevalov, A. Perrin, E. R. Polovtseva, C. Richard, M. A. H. Smith, E. Starikova, K. Sung, S. Tashkun, J. Tennyson, G. C. Toon, V. G. Tyuterev, and G. Wagner. The HITRAN2012 molecular spectroscopic database. *Journal of Quantitative Spectroscopy and Radiative Transfer*, 130:4–50, 2013. doi: 10.1016/j.jqsrt.2013.07.002. URL https://www.sciencedirect.com/science/article/pii/S0022407313002859.

J. M. Russell III, M. G. Mlynczak, L. L. Gordley, J. J. Tansock, Jr., and R. W. Esplin.

Overview of the SABER experiment and preliminary calibration results. page 277, Denver, CO, USA, 1999. doi: 10.1117/12.366382. URL http://proceedings.spiedigitallibrary.org/proceeding.aspx?doi=10.1117/12.366382.

S. Sander, J. Abbatt, J. Barker, J. Burkholder, R. Friedl, D. Golden, R. Huie, M. Kurylo, G. Moortgat, V. Orkin, and P. Wine. Chemical Kinetics and Photochemical Data for Use in Atmospheric Studies, Evaluation No. 17, 2011.

H. Schmidt, G. P. Brasseur, M. Charron, E. Manzini, M. A. Giorgetta, T. Diehl, V. I. Fomichev, D. Kinnison, D. Marsh, and S. Walters. The HAMMONIA Chemistry Climate Model: Sensitivity of the Mesopause Region to the 11-Year Solar Cycle and CO_2 Doubling. *Journal of Climate*, 19(16):3903–3931, 2006. doi: 10.1175/JCLI3829.1. URL http://journals.ametsoc.org/doi/10.1175/JCLI3829.1.

F. Schreier. Optimized implementations of rational approximations for the Voigt and complex error function. *Journal of Quantitative Spectroscopy and Radiative Transfer*, 112(6):1010–1025, 2011. doi: 10.1016/j.jqsrt.2010.12.010. URL https://linkinghub.elsevier.com/retrieve/pii/S002240731000467X.

W. Schreiner, J. Weiss, R. Anthes, J. Braun, V. Chu, J. Fong, D. Hunt, Y. Kuo, T. Meehan, W. Serafino, J. Sjoberg, S. Sokolovskiy, E. Talaat, T. Wee, and Z. Zeng. COSMIC-2 Radio Occultation Constellation: First Results. *Geophysical Research Letters*, 47(4), 2020. doi: 10.1029/2019GL086841. URL https://onlinelibrary.wiley.com/doi/10.1029/2019GL086841.

SciaL1C. https://earth.esa.int/eogateway/tools/scial1c-command-line-tool. Accessed: 2023-06-16.

C. Shannon. Communication In The Presence Of Noise. *Proceedings of the IEEE*, 86(2):447–457, 1998. doi: 10.1109/JPROC.1998.659497. URL http://ieeexplore.ieee.org/document/659497/.

P. Sheese. *Mesospheric ozone densities retrieved from OSIRIS observations of the oxy-*

gen A-band dayglow. PhD thesis, Library and Archives Canada, Ottawa, 2009. ISBN 9780494649367.

P. E. Sheese, E. J. Llewellyn, R. L. Gattinger, A. E. Bourassa, D. A. Degenstein, N. D. Lloyd, and I. C. McDade. Temperatures in the upper mesosphere and lower thermosphere from OSIRIS observations of O $_2$ A-band emission spectra. *Canadian Journal of Physics*, 88(12): 919–925, 2010. doi: 10.1139/p10-093. URL `http://www.nrcresearchpress.com/doi/10.1139/p10-093`.

G. G. Shepherd, G. Thuillier, W. A. Gault, B. H. Solheim, C. Hersom, J. M. Alunni, J.-F. Brun, S. Brune, P. Charlot, L. L. Cogger, D.-L. Desaulniers, W. F. J. Evans, R. L. Gattinger, F. Girod, D. Harvie, R. H. Hum, D. J. W. Kendall, E. J. Llewellyn, R. P. Lowe, J. Ohrt, F. Pasternak, O. Peillet, I. Powell, Y. Rochon, W. E. Ward, R. H. Wiens, and J. Wimperis. WINDII, the wind imaging interferometer on the Upper Atmosphere Research Satellite. *Journal of Geophysical Research*, 98(D6):10725, 1993. doi: 10.1029/93JD00227. URL `http://doi.wiley.com/10.1029/93JD00227`.

G. G. Shepherd, G. Thuillier, Y.-M. Cho, M.-L. Duboin, W. F. J. Evans, W. A. Gault, C. Hersom, D. J. W. Kendall, C. Lathuillère, R. P. Lowe, I. C. McDade, Y. J. Rochon, M. G. Shepherd, B. H. Solheim, D.-Y. Wang, and W. E. Ward. The Wind Imaging Interferometer (WINDII) on the Upper Atmosphere Research Satellite: A 20 year perspective. *Reviews of Geophysics*, 50(2), 2012. doi: 10.1029/2012RG000390. URL `http://doi.wiley.com/10.1029/2012RG000390`.

T. G. Slanger, D. L. Huestis, D. E. Osterbrock, and J. P. Fulbright. The Isotopic Oxygen Nightglow as Viewed from Mauna Kea. *Science*, 277(5331):1485–1488, 1997. doi: 10.1126/science.277.5331.1485. URL `https://www.science.org/doi/10.1126/science.277.5331.1485`.

A. K. Smith. Physics and chemistry of the mesopause region. *Journal of Atmospheric and Solar-Terrestrial Physics*, 66(10):839–857, 2004. doi: 10.1016/j.jastp.2004.01.032. URL `https://linkinghub.elsevier.com/retrieve/pii/S1364682604000513`.

V. F. Sofieva, A. S. Gurvich, F. Dalaudier, and V. Kan. Reconstruction of internal gravity wave

and turbulence parameters in the stratosphere using GOMOS scintillation measurements. *Journal of Geophysical Research*, 112(D12):D12113, 2007. doi: 10.1029/2006JD007483. URL `http://doi.wiley.com/10.1029/2006JD007483`.

R. Song, M. Kaufmann, M. Ern, J. Ungermann, G. Liu, and M. Riese. Three-dimensional tomographic reconstruction of atmospheric gravity waves in the mesosphere and lower thermosphere (MLT). *Atmospheric Measurement Techniques*, 11(5):3161–3175, 2018. doi: 10.5194/amt-11-3161-2018. URL `https://amt.copernicus.org/articles/11/3161/2018/`.

K. K. Talukdar and W. D. Lawing. Estimation of the parameters of the Rice distribution. *The Journal of the Acoustical Society of America*, 89(3):1193–1197, 1991. doi: 10.1121/1.400532. URL `http://asa.scitation.org/doi/10.1121/1.400532`.

A. Tarantola. *Inverse Problem Theory and Methods for Model Parameter Estimation*. Society for Industrial and Applied Mathematics, 2005. doi: 10.1137/1.9780898717921. URL `http://epubs.siam.org/doi/book/10.1137/1.9780898717921`.

A. N. Tikhonov and V. I. Arsenin. *Solutions of ill-posed problems*. Scripta series in mathematics. Winston ; distributed solely by Halsted Press, Washington : New York, 1977. ISBN 978-0-470-99124-4.

C. C. Triplett, B. J. Harding, Y.-J. J. Wu, S. England, C. R. Englert, J. J. Makela, M. H. Stevens, and T. Immel. Large-Scale Gravity Waves in Daytime ICON-MIGHTI Data from 2020. *Space Science Reviews*, 219(1):3, 2023. doi: 10.1007/s11214-022-00944-w. URL `https://link.springer.com/10.1007/s11214-022-00944-w`.

T. Tsuda, M. Nishida, C. Rocken, and R. H. Ware. A Global Morphology of Gravity Wave Activity in the Stratosphere Revealed by the GPS Occultation Data (GPS/MET). *Journal of Geophysical Research: Atmospheres*, 105(D6):7257–7273, 2000. doi: 10.1029/1999JD901005. URL `http://doi.wiley.com/10.1029/1999JD901005`.

J. Ungermann, A. Kleinert, G. Maucher, I. Bartolomé, F. Friedl-Vallon, S. Johansson, L. Krasauskas, and T. Neubert. Quantification and mitigation of the instrument effects

and uncertainties of the airborne limb imaging FTIR GLORIA. *Atmospheric Measurement Techniques*, 15(8):2503–2530, 2022. doi: 10.5194/amt-15-2503-2022. URL `https://amt.copernicus.org/articles/15/2503/2022/`.

R. A. Vincent. The dynamics of the mesosphere and lower thermosphere: a brief review. *Progress in Earth and Planetary Science*, 2(1):4, 2015. doi: 10.1186/s40645-015-0035-8. URL `http://www.progearthplanetsci.com/content/2/1/4`.

S. Watchorn, F. L. Roesler, J. M. Harlander, K. P. Jaehnig, R. J. Reynolds, and W. T. Sanders III. Development of the spatial heterodyne spectrometer for VUV remote sensing of the interstellar medium. In O. H. W. Siegmund, S. Fineschi, and M. A. Gummin, editors, *UV/EUV and Visible Space Instrumentation for Astronomy and Solar Physics,*, pages 284–295, San Diego, CA, 2001. Proc. SPIE 4498. doi: 10.1117/12.450063. URL `http://proceedings.spiedigitallibrary.org/proceeding.aspx?articleid=894451`.

J. A. C. Weideman. Computation of the Complex Error Function. *SIAM Journal on Numerical Analysis*, 31(5):1497–1518, 1994. doi: 10.1137/0731077. URL `http://epubs.siam.org/doi/10.1137/0731077`.

S. Wold, K. Esbensen, and P. Geladi. Principal component analysis. *Chemometrics and Intelligent Laboratory Systems*, 2(1-3):37–52, 1987. doi: 10.1016/0169-7439(87)80084-9. URL `https://linkinghub.elsevier.com/retrieve/pii/0169743987800849`.

O. Wroblowski. Characterisation and In-Orbit Demonstration of a Heterodyne Spectrometer for Atmospheric Research from Small Satellites. 2023. doi: 10.25926/BUW/0-113. URL `https://elekpub.bib.uni-wuppertal.de/doi/10.25926/BUW/0-113`. Publisher: Bergische Universität Wuppertal.

D. L. Wu. Mesoscale gravity wave variances from AMSU-A radiances. *Geophysical Research Letters*, 31(12):L12114, 2004. doi: 10.1029/2004GL019562. URL `http://doi.wiley.com/10.1029/2004GL019562`.

D. L. Wu and S. D. Eckermann. Global Gravity Wave Variances from Aura MLS: Characteristics and Interpretation. *Journal of the Atmospheric Sciences*, 65(12):3695–3718,

2008. doi: 10.1175/2008JAS2489.1. URL https://journals.ametsoc.org/doi/10.1175/2008JAS2489.1.

D. L. Wu and J. W. Waters. Gravity-wave-scale temperature fluctuations seen by the UARS MLS. *Geophysical Research Letters*, 23(23):3289–3292, 1996. doi: 10.1029/96GL02924. URL http://doi.wiley.com/10.1029/96GL02924.

V. Yankovsky and E. Vorobeva. Model of Daytime Oxygen Emissions in the Mesopause Region and Above: A Review and New Results. *Atmosphere*, 11(1):116, 2020. doi: 10.3390/atmos11010116. URL https://www.mdpi.com/2073-4433/11/1/116.

V. A. Yankovsky and R. O. Manuilova. Model of daytime emissions of electronically-vibrationally excited products of O_3 and O_2 photolysis: application to ozone retrieval. *Annales Geophysicae*, 24(11):2823–2839, 2006. doi: 10.5194/angeo-24-2823-2006. URL https://angeo.copernicus.org/articles/24/2823/2006/.

K. Yoshino, W. H. Parkinson, K. Ito, and T. Matsui. Absolute absorption cross-section measurements of Schumann–Runge continuum of O_2 at 90 and 295K. *Journal of Molecular Spectroscopy*, 229(2):238–243, 2005. doi: 10.1016/j.jms.2004.08.020. URL https://www.sciencedirect.com/science/article/pii/S0022285204002772.

M. V. Zagidullin, N. A. Khvatov, I. A. Medvedkov, G. I. Tolstov, A. M. Mebel, M. C. Heaven, and V. N. Azyazov. O_2 ($b^1\Sigma_g^+$) Quenching by O_2, CO_2, H_2O, and N_2 at Temperatures of 300–800 K. *The Journal of Physical Chemistry A*, 121(39):7343–7348, 2017. doi: 10.1021/acs.jpca.7b07885. URL https://pubs.acs.org/doi/10.1021/acs.jpca.7b07885.

A. Zarboo, S. Bender, J. P. Burrows, J. Orphal, and M. Sinnhuber. Retrieval of and $O_2(^1\Sigma)$ and $O_2(^1\Delta)$ volume emission rates in the mesosphere and lower thermosphere using SCIAMACHY MLT limb scans. *Atmospheric Measurement Techniques*, 11(1):473–487, 2018. doi: 10.5194/amt-11-473-2018. URL https://amt.copernicus.org/articles/11/473/2018/.

C. Zhu and P. R. Griffiths. Extending the Range of Beer's Law in FT-IR Spectrometry. Part I: Theoretical Study of Norton—Beer Apodization Functions. *Applied Spectroscopy*, 52(11):

1403–1408, 1998. doi: 10.1366/0003702981943022. URL http://journals.sagepub.com/doi/10.1366/0003702981943022.

Y. Zhu and M. Kaufmann. Consistent Nighttime Atomic Oxygen Concentrations From O_2 A-band, O(^{1}S) Green-Line, and OH Airglow Measurements as Performed by SCIAMACHY. *Geophysical Research Letters*, 46(14):8536–8545, 2019. doi: 10.1029/2019GL083550. URL https://onlinelibrary.wiley.com/doi/10.1029/2019GL083550.

M. Šimečková, D. Jacquemart, L. S. Rothman, R. R. Gamache, and A. Goldman. Einstein A-coefficients and statistical weights for molecular absorption transitions in the HITRAN database. *Journal of Quantitative Spectroscopy and Radiative Transfer*, 98(1):130–155, 2006. doi: 10.1016/j.jqsrt.2005.07.003. URL https://linkinghub.elsevier.com/retrieve/pii/S0022407305002931.